AVALANCHES IN STARS AND AT FINITE TEMPERATURE

BY

MOHAMMED AZEEM SHEIKH

DISSERTATION

Submitted in partial fulfillment of the requirements
for the degree of Doctor of Philosophy in Physics
in the Graduate College of the
University of Illinois at Urbana-Champaign, 2019

Urbana, Illinois

Doctoral Committee:

Professor Emeritus Richard L. Weaver, Chair
Professor Karin A. Dahmen, Director of Research
Professor Emeritus Michael B. Weissman
Professor S. Lance Cooper

Abstract

We study two related but distinct aspects of avalanches in physical systems. The first is the study of avalanches that we have observed in stars. We apply results from the mean field avalanche model to observations made by the *Kepler* spacecraft and the VIRGO instrument, looking at several stars including our own Sun and Tabby's star.

In this examination, we use the stars' light curve, their integrated flux as a function of time, to extract avalanche information. Dimming events on the Sun are fairely well understood, and we find that there is scaling even in the Sun's data, likely caused by sunspots or combinations of such spots. We also look at Tabby's star, where the anomalous dimming has not been explained, and show that there is also avalanche scaling seen in this extraordinary star.

We then look at avalanches at finite but low temperature in plastic deformation. The slow plastic deformation of materials under stress, known as creep motion, has long been studied in material's science. We hypothesize that at low temperatures, this deformation is the result of temperature activated avalanches. In order to explore this idea, we develop an extension of the mean field model to incorporate temperature. This model poses a problem since it requires exponentially many evaluations of rate constants when simulated using a kinetic monte carlo algorithm. We solve this problem by using a recursive strategy to pair down the number of evaluations and effectively choose the appropriate rate constants.

Finally, we evaluate theoretically the interevent time distribution between these thermally activated avalanches. We identify high and low temperature regimes, at which the character of the distributions changes dramatically. We use simulations to verify our results, and connect them to experimental efforts currently underway to determine these distributions.

Dedicated to my grandfather, for his unwavering support of my scientific pursuits.

Acknowledgments

It is difficult to write an acknowledgement without mentioning first my adviser, Karin Dahmen, without whom I would have not have completed my Ph.D. I want to thank Lance Cooper, who guided me through some very tough academic times with his sensible advice. Richard Weaver was also incredibly helpful, first as a kind ear to listen to my bad ideas and my good ideas, and second, as essentially another adviser for me. Mike Weissman also helped me in many unexpected ways, particularly for sharing his passion of physics and his enthusiasm of his work with me.

I want to thank my parents, Zia and Neelam, my brother Osaid, and my sister Aisha. Although they may not know it, they have all supported me throughout my graduate career. I want to thank Megan White, who also stood by listening to my complaints and always giving good advice. She helped shape most of my graduate life. Also thanks to the rest of my Champaign-Urbana family, too numerous to name individually, who I made memories with that will last a lifetime. I would also like to thank the GEO, they (as a collective and as individuals) expanded my horizons and taught me things you can't learn in a classroom. Also to my extended family, again too numerous to name, who supported me throughout my career.

Finally, I would thank my grandfather, who never once asked me how much money I was going to make, or what kind of job I was going to have after graduating. His only refrain was proud words in my willingness to dive into scientific pursuit. His only questions were about my research, asked in earnest curiosity and not out of obligation.

Table of Contents

Chapter 1

Introduction

1.1 Avalanches and Crackling Noise

Noise is a constant and ubiquitous feature of nature. The types and forms of noise are too varied to count. The most significant type of noise in this thesis is known specifically as crackling noise [1]. Crackling noise is particularly interesting because it is associated with a specific mechanism of relaxation known as avalanches. When the word avalanche is used, it is usually used in the context of a runaway chain reaction that only slows down as the result of either external forces or limits of the system size. In the context of this thesis, avalanches adapt a broader meaning, specifically as the causes of crackling noise.

The examples of systems that exhibit crackling noise in nature are both plentiful and varied. A well-studied example of crackling noise is the Barkhausen noise exhibited by certain types of magnets [2, 3, 4]. Other examples include solar flares [5], earthquakes [6, 7], the dynamics of superconductors [8, 9], the pinning of driven charge density waves by disorder [10], interfaces advancing in a random medium [11, 12], and plastic deformation of nanocrystals and bulk metallic glasses under stress [13, 14, 15]. Our list is by no means exhaustive, but shows that such phenomena are common.

In fact, what is so special about crackling noises and avalanches is that although these phenomena occur in so many different places, they share a distinct set of common properties. Because noise is in general a stochastic process, these properties are all exhibited as statistical similarities in the avalanches observed. When determining whether a system exhibits avalanches, it is common to rely not upon a single event, but a broad range of events that show a common pattern in their statistics. The exact property shared by all avalanche phenomena is self-similarity over a regime known as the scaling regime [16, 1], both in how these phenomena physically manifest themselves (their physical size, their evolution in time, etc.) [6, 17, 18, 4], but also in how their statistics are self-similar over a certain range [17, 7]. The precise meaning of self-similarity, as well as its causes, are the domain of the renormalization group [19, 20, 10, 1].

1.2 Avalanches in Magnetic Materials

Crackling noise [1] in the context of magnets is often known as Barkhausen noise [3], but it has been shown to occur in many magnetic materials exhibiting hysteresis [21, 16, 1]. Although we do not focus only on magnetic avalanches, they offer an instructive and simplified version of avalanches we study. A magnetic material, initially in some magnetic field, has large magnetic domains pointing along this magnetic field. As the magnetic field is slowly driven towards zero and flipped in the opposite direction, there are at first slight domain flips between the original domain orientation and its reverse. These flips can happen in a continuous fashion, so that the domains slowly realign themselves with the magnetic field. However, when disorder is added to the system, it is often observed that these domains flip in random bursts [21, 2] rather than continuously. These random bursts are identified as avalanches.

Two conditions are generally observed to be needed for avalanches. The first is the presence of a driving force. Avalanches only occur when the driving force changes, in this case the magnetic field. The second is the presence of disorder in the system. This disorder is fundamental for some form of avalanches [21, 22] to occur in the system. If there is too much disorder is in the system, the domain walls remain pinned to a given orientation despite the opposition of the magnetic field. Once the magnetic field becomes large enough, the whole system flips at once. Alternatively, if there is too little disorder is in the system, the domain walls flip in small bursts, the result being a smoother flow between polarities. There is a middle ground of disorder at which the avalanches occur over a broad range of sizes [22]. The width of this broad range of sizes (here the number of flipped cells in a given avalanche) is tuned based on the tuning parameter, the disorder.

1.3 Plastic Deformation Through Avalanches

Plastic deformation through avalanches is another extensively studied area of crackling noise [13]. It will be one of the main focuses of this thesis. Plastic deformation is the permanent distortion of a material when it is subject to tensile, compressive, shearing, or torsional stress. Both crystalline materials [23, 24, 14] and amorphous materials [25, 15, 26] are theorized and experimentally shown [14, 15] to plastically deform through avalanches. Like magnetic avalanches, there is both a driving force and disorder in these systems [27]. In this case the driving force is the stress on the system. The disorder is built into the system in the form of irregular defects [27] such as dislocations in crystalline materials [28] or shear transformation zones [29, 30] in bulk metallic glasses.

We restrict ourselves to plastic deformation of crystalline materials and bulk-metallic glasses. Crystalline materials are usually single crystals such as Al or Cu. The crystalline materials that have been shown to have avalanches are primarily face-centered cubic, body-centered cubic, and hexagonally close packed crystals [14, 31]. Similarly, the bulk-metallic glasses have also been shown to undergo plastic deformation through avalanches [15, 26]. Bulk-metallic glasses (BMGs) are amorphous materials, in that they do not form crystalline structures because they are usually alloys that are cooled too quickly to form crystals. An example of a BMG is $\mathrm{Zm}_{45}\mathrm{Hf}_{12}\mathrm{Nb}_5\mathrm{Cu}_{15.4}\mathrm{Ni}_{12.6}\mathrm{Al}_{10}$ which has been experimentally shown to exhibit avalanche phenomena [15].

In order to study plastic deformation in a general setting, we use a simplified model of two interfaces sliding against each other, similar to a fault zone that slides during an earthquake [13]. Initially let us think about the interface at zero temperature. Then the only relevant variation the interface experiences is a stress Σ, and the interface responds by sliding at a velocity v. In order to think about plasticity, it is necessary that the interface remains pinned for small stresses, with the source of this pinning being the disorder in the material. As stress increases, it reaches what is known as a critical stress. This critical stress Σ_c is the point at which the interface begins sliding. In other words, $v = f(\Sigma - \Sigma_c)$, where $f(x) = 0$ for $x < 0$, and *a priori* $f(x)$ can be any arbitrary function (if there is hysteresis, it does not even have to be single valued [21]). This equation, analogous to equations of state in classical equilibrium statistical mechanics, is an expression of the material properties at a given force. The equation $v = f(\Sigma - \Sigma_c)$ is a similar to an equation of state, in that it gives us the value of one parameter v, at a fixed value of another parameter Σ, similar to how equation of state for liquids relates pressure, volume, and temperature. Note that in general, there is a another parameter in all of our equations, the system size, which we denote by the number of particles N. For the present discussion, assume that we study the system in the thermodynamic limit $N \to \infty$, but in chapter 6 we will consider finite but large N.

In the simplest case, when Σ is near Σ_c the function $f(\Sigma - \Sigma_c)$ turns out to be a power law, and is related to the scale invariance of the crackling noise as mentioned above. Therefore $v \sim (\Sigma - \Sigma_c)^\beta$, which defines the exponent β. One method to derive β is through the renormalization group [10, 11, 6, 1, 13], and this exponent β is expected to be universal [32, 19]. Here, universality means that the exponent depends only on the dimensions of the system (the number of free parameters needed to describe the system), the symmetries of the system, and how the interactions between elements in the system scale at long distances. In contrast to the exponent β, the critical force Σ_c is not universal. It depends on the specific details of the system we are studying, and even on the specific sample being studied. However, the critical force is important, as it defines the critical point at which many quantities exhibit scale invariance. We will discuss the details of such critical points when reviewing the general theory of avalanches in chapter 4.

1.3.1 Plastic deformation in crystalline materials

In crystalline materials, the primary source of plastic deformation comes from the movement of dislocations [33]. Similarly, the disorder can either be provided through defects besides dislocations, such as point defects [34] that are common in alloyed materials, or through emergent phenomena such as jamming [35, 36]. It is surprising that different mechanisms of dislocation pinning can lead to similar behavior, for example with β being the same in both cases, but this has been observed in simulations [35], although it has not been theoretically justified.

Unlike the case of a simple picture with a single dislocation, in real plastic deformation, there are many dislocations that interact to result in deformation. We do not discuss detail the theory of dislocations, but we do need information about how the dislocations interact with one another. As is probably clear, the lattice distortions will cause stresses in the crystal. These stresses cause the formation of a glide plane along which the crystal deforms [37, 38]. These glide planes are the faults we discussed earlier, and we assume that they have formed when considering crystal deformation. When talking about a glide plane of dislocations, it turns out that the interaction between pieces of dislocations scales as $1/r^3$ along the plane [6, 39]. This force is long range, and as we will show later this is crucial for developing a mean field theory that has been shown to agree with simulations of 3 dimensional dislocation dynamics [40, 41]. In general, we denote long range interactions to be interactions that scale as $1/r^{d+1}$ or more slowly for arbitrary dimensions d. Here $d = 2$ since we are talking about the glide plane along which the dislocations have formed.

1.3.2 Plastic deformation in amorphous materials

Unlike crystalline materials, where the source of plastic deformation is clear and well established, amorphous materials are much more complex. We focus particularly on bulk-metallic glass in this thesis, otherwise known as amorphous metals. It has long been argued that the source of plastic deformation of amorphous materials is due to free volume [42]. Here, free volume can be best visualized as vacancies in the packing of atoms in amorphous materials. This free volume allows atoms to slide past one another, usually through what is known as a shear transformation zone (STZ) [29, 30]. Although the precise mechanism is still controversial (whether by sliding [30] or through vacancies [29]), the basic idea is of an STZ is of a local cluster of atoms that undergoes an activation from one low energy state to another via a higher energy (and more densely packed) state [43, 42]. Experimental characterization of STZs agree very well with theoretical developments [44, 45, 46, 47, 48].

Because of the slightly more vague structure of shear transformation zones, exact stress and strain fields are more complicated in these cares. What is known about STZs is that they likely involve 100s of atoms that rearrange themselves when a material experiences a load [47]. Rather, many authors rely either on two state models (active vs. not active) [43], molecular dynamics simulations [43, 49], or because they involve a significant number of atoms, simplified continuum dynamics models [50, 51]. We focus especially on the latter, where it has been found that the most effective description of stress transfer due to slipping STZs are the stress fields of ellipsoidal inclusions (Eshelby inclusions) [52], which has been shown experimentally using colloidal glasses as a prototype of an amorphous solid [50]. Here, an ellipsoidal inclusion is a region within an elastic solid with an ellipsoidal boundary inside a homogeneous medium that has been deformed [52].

Similar to the discussion on crystalline materials, the ellipsoidal inclusion has a long range interaction with other ellipsoidal inclusions, with the interaction strength going as $1/r^3$ [52]. Once again, we see long range interactions at play, which will be important in justifying use of mean field theory as a collective model of local slips with similar stress distributions resembling to leading approximation to ellipsoidal inclusions.

1.4 12 Decades of Scaling

In the previous discussion, we saw that avalanches occur in a wide range of systems. Although the details of each system are different, there are a few underlying principles which are common between these systems. The first is that each system is not in equilibrium, and that there is a force driving the system out of equilibrium. The second is the presence of disorder in each of these systems, and usually this disorder is quenched [53]. Here quenched means that the disorder is not part of the dynamics of the theory, and is present as a type of background heterogeneity. However, note that the quenched randomness we talk about may also have some history dependence [6, 17]. Although disorder is sometimes part of the dynamics, especially in the case of jamming [36], we will take the independence of the disorder from the dynamics as a simplifying assumption. Finally, the interactions between elements in the system are long ranged. Given that these are fairly generic requirements, it comes as no surprise that avalanche behavior, and specifically, mean-field avalanche behavior is seen in over 12 decades of length scales [54], from nanocrystals [14] to earthquakes [55, 6, 7, 56, 57] to stars [5, 58, 59].

1.4.1 Avalanches in Stars and the *Kepler* Spacecraft

One of the main aspects of this thesis will discuss avalanches in stars. A basic understanding of stellar properties is vital to understanding the classification of stars and why Tabby's star [60] is such a strange star. Of the stellar properties that are directly visible to astronomers, the two easiest to measure are the temperature and the luminosity. The temperature is measured using the peak of the spectrum of the star (assuming black body radiation), while the luminosity is measured using the apparent luminosity (i.e. luminosity as observed on Earth) and some independent measure of distance, typically either parallax, through the use of standard candle stars [61] for which the luminosity is a known value, or even through the Hertzsprung-Russell diagram plotted below [62].

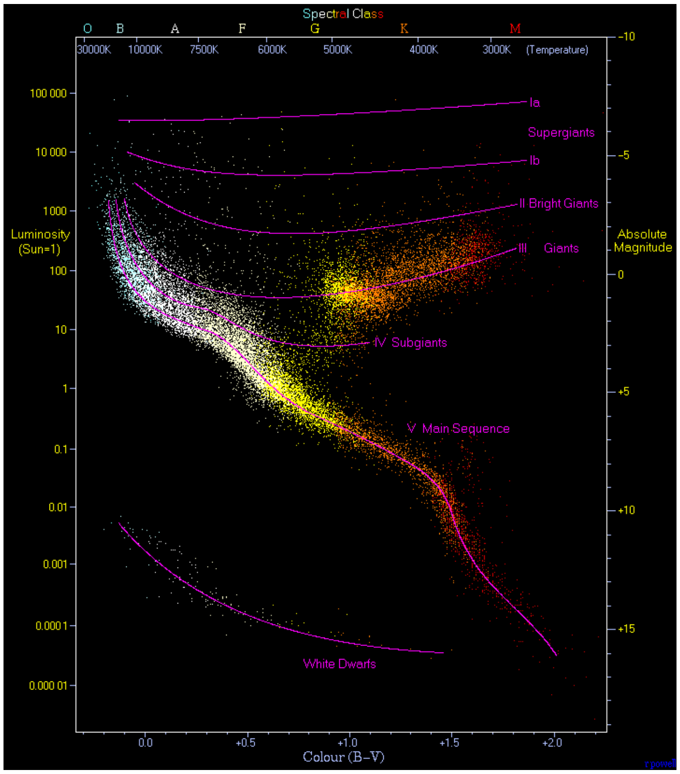

Figure 1.1: The Hertzsprung-Russell diagram [63], detailing how stellar properties are related to one another. The temperature is plotted on an inverse loglog plot against the luminosity (with the Sun having luminosity 1). The main sequence is highlighted as the primary line that sweeps through the diagram. Above the temperature axis are labels for the various stellar spectral classes. On the x axis, we see that the color changes from red (cool) to blue (hot), as blue wavelengths are shorter and more energetic than red wavelengths.

A simple physical observation based on the Stefan-Boltzmann law is that the luminosity $L \propto T^4R^2$. It is natural to plot the luminosity of observed stars as a function of temperature, and this results in the Hertzsprung-Russell diagram. One expects the luminosity to scale as a power of the temperature, and for the most part this is the case on what is known as the main sequence. The exponent is somewhat higher than 4 as hotter stars also tend to be larger, but the relationship holds fairly well. Stellar classifications are based on temperature, and are defined with the letters O, B, A, F, G, K, and M, with O being the hottest and M being the coolest stars. In addition, for each letter there is a numeric digit with 0 being the hottest and 9 being the coolest. For example, the Sun is a type $G2$ star, and specifically known as a $G2V$ star, where the V means the Sun is on the main sequence.

Historically the primary avalanches which have been observed in stars are stellar flares [58], and their analogue on the Sun known as solar flares [5]. These avalanches are thought to be connected to the star's magnetic field [5, 64, 65]. As was shown in a recent paper, data besides solar flares can also be seen to have properties akin to avalanches [59]. This data was extracted from the *Kepler* spacecraft. Initially, *Kepler* was launched to study distant planets around other stars, known as exoplanets [66]. The goal was to observe about 150,000 stars simultaneously and look for signatures of very minute and periodic dimming events that indicated an exoplanet was orbiting a far away star.

It turned out that *Kepler* could be used for all sorts of fascinating explorations of stars. As mentioned before, when stars have exceptionally strong flares, it was possible to spot these with *Kepler* [58, 67, 68], and this led to another type of power law that is seen in the *Kepler* data. Additionally, one could look at how the luminosity of red giants oscillates [69], which ushered in a new age of looking at the internals of these mysterious stars, a field known as astroseismology. We will show below that the *Kepler* data can also be used to find evidence of avalanches. The most striking example of this is Tabby's star [60], for which there are dimming events on the order of 20% of the total luminosity of the star. Unlike the case of other extraordinary stars studied using *Kepler*, Tabby's star is thoroughly average in most ways except for these dimming events. The exact mapping of the dimming events to avalanches is slightly complex, but has been used previously [5].

1.5 Introduction to the Theory of Avalanches

Given all of these examples, we have mentioned earlier the common thread that connects them. This is the mean field theory of avalanches [6, 17, 7, 13]. We will go over some simple concepts and results from this theory, and develop more formal arguments later. As a theory of avalanches, the primary quantities of interest are the size of the avalanche and the duration of the avalanche. Traditionally, the size of a *slip* avalanche is the total, time-integrated displacement during an avalanche, otherwise known as the potency [13]. For example, if we denote $u(\mathbf{x}, t)$ to be the discontinuity along a fault that is slipping during an avalanche, the size would be

$$S = \int_{\mathcal{D}} d^2x dt u(\mathbf{x}, t) \tag{1.1}$$

where $\mathbf{x}$ denotes coordinates along the fault, t denotes the time, and $\mathcal{D}$ denotes the domain over which the avalanche occurred. Similarly, the duration is defined as the time over which the avalanche occurs.

This interpretation of avalanche size makes sense when talking about earthquakes [6], plastic deformation [13], granular deformation [25], or other slip events. We denote such events as slip avalanches rather than just avalanches, although we will sometimes use the words interchangeably. Luckily, the definition also generalizes to the astrophysics case (in astrophysics magnetic avalanches may be more common [16, 21, 22]). Here, $u(\mathbf{x}, t)$ is not a discontinuity along a fault, but a change in luminosity from a predefined ambient luminosity. The surface in this case is the surface of the star (usually), and this definition is similar to one used for solar flares [5]. The size of an avalanche is the total time integrated luminosity, which is known as the radiant fluence (or change thereof), otherwise known as the energy per unit surface area. What is important is that although the interpretation of $u(\mathbf{x}, t)$ has changed, the definition of the size and duration remains unaltered. The need for an ambient field, in this case played by the star's ambient luminosity, is also not entirely without precedent. This is common in many interface slipping problems [70], where one is looking for avalanches above the critical stress. Recall from earlier that above the critical force, the interface acquires a velocity $v \sim (\Sigma - \Sigma_c)^{\beta}$. In this case, near Σ_c, avalanches can still be defined by looking at variations around this slipping velocity.

The problem is then reduced to finding evidence of avalanches in the data that show evidence of scaling. For all purposes, these events can be considered random because of the requirement of quenched randomness as mentioned above. Therefore, we usually talk about avalanche size and duration distributions. Renormalization predicts in the simplest case that the avalanche size $p(S) \sim S^{-\tau} f(S/S_{max})$ [10, 11, 21, 22, 17, 13] near a critical point. Mean field theory predicts this exponent $\tau = 3/2$ [21, 22, 17], although this exponent has been known for a much longer time in the theory of branching processes [71]. Here $f(S/S_{max})$ is an arbitrary function that approaches unity when $S \ll S_{max}$ and decays quickly for $S > S_{max}$. Similarly, the theory predicts $p(T) \sim T^{-\alpha} g(T/T_{max})$ [10, 11, 21, 22, 17], with $g(x)$ playing the same role as $f(x)$ above. It is notable that in MFT, the predicted form of $f(x), g(x) \to e^{-x}$ for large x [17]. Other predictions include the detailed forms of averaged shapes of avalanches, spatial correlation functions, and so forth [22, 18, 72, 73, 74, 75, 76].

1.5.1 Non-equilibrium Critical Phenomena

All of these predictions rely upon the renormalization group applied to non-equilibrium situations [1]. The renormalization group (RG) is the application of scale transformations to systems, as in the familiar case of the Ising model [19]. The exact prescription [20, 77] does not rely on the assumption of equilibrium. Instead, it is relies on coarse graining and then rescaling [78]. The term coarse graining is somewhat vague, and many methods exist to coarse grain, including majority rule and averaging for Ising spins [77] to momentum coarse graining [6, 22] in field theory. After coarse graining, the units of measurement must be rescaled so that the original units can be mapped to the rescaled values.

The upshot of all of this is that under this repeated application of RG transformations (i.e. under repeated coarse graining and rescaling), the system's various interactions all flow along with the rescaling value, so that each of the infinitely many interactions flow with application of the RG transformations [77]. Most of these interactions turn out to be unimportant for large systems, and flow towards zero. There are specific points in this flow which are fixed points that are invariant under the RG transformation. These points are clearly scale invariant, as rescaling does not change their nature. In the equilibrium case these fixed points either define a phase of the matter, or they define a phase transition between two phases [20, 78, 77]. This analogy is carried through to the non-equilibrium case, even though in the nonequilibrium case the focus is no longer on the states but on the paths that a system can follow [10, 11, 22]. For an interface under stress Σ, the interface can be either stuck at low stresses ($\Sigma < \Sigma_c$) or moving at high stresses ($\Sigma > \Sigma_c$). Between these two regimes is a critical stress $\Sigma = \Sigma_c$ corresponding to a renormalization fixed point where the power law scaling behavior and scale invariance is observed [17, 1]. Near a critical fixed point one finds universal behavior, because it is associated with a diverging correlation length that dominates the dynamics so that microscopic details do not matter near Σ_c [32, 19]. For a large class of theories, the renormalization flow results in the same fixed points.

Scale invariance is directly related to the power laws we often see in avalanche phenomena. To be precise, scale invariance of $f(x)$ is the property that $f(\lambda x) = \lambda^{\Delta} f(x)$. The exact solution to this functional equation is known as a homogeneous function [77], which for a single variable is a power law. For mean field theory, the exponents are denoted by different greek letters. For the size distribution the exponent is $\tau = 3/2$, while for the duration the exponent is $\alpha = 1$. In addition to this, the size versus duration also scales with an exponent $\sigma\nu z = 1/2$, so that $T \sim S^{\sigma\nu z}$, where σ, ν, and z all define other exponents [22, 6, 13, 25].

The full description of these scaling laws, as well as how renormalization works for these types of problems is covered in the appendices. Here we will give a plausible argument that the upper critical dimension d_c, the point at which mean field theory applies, is 2, in order to later justify the use of mean field theory. First, to fix notation (sometimes d_c is taken to be 3, even though the problem has not changed [11]), the dimension we refer to is the dimension of the interface. If we consider our earlier discussion, this is the number of degrees of freedom of $\mathbf{x}$ in $u(\mathbf{x}, t)$, for which we have already fixed at 2 in the problems we discuss.

The argument is actually very old [79], similar to Imry-Ma type of arguments for random field Ising spins [80, 6, 13]. We take as our model system a set of spins with long range positive interactions in a d dimensional space. We could instead talk about a d dimensional interface, but the spin picture is somewhat less difficult to imagine. The interactions prevent the spins from adopting any non-uniformity, instead snapping it back to the average value. The disorder causes the spins to point in random directions. These two forces oppose each other, as our spins wants to be very ordered because of the long range interactions, and very disordered because of the defects. Then over long length scales, the interaction strength between spins scales as $1/L^{d+1}$ because the spins have long range interactions, as mentioned above (i.e. for $d = 2$, the interaction strength between spins scales as $1/L^3$) [39, 41, 13]. Since the spins span a d dimensional space, the total interaction strength (i.e. integrate the interaction strengths of the spins over a space L^d) scales as $L^d/L^{d+1} = L^{-1}$. Similarly, the sum of many random forces will slowly go to zero, and will go to zero as $L^{-d/2}$, the familiar expression for averaging random interactions. These two quantities scale at the same rate at $d = 2$, suggesting that there is a balance between interaction and disorder here. Above this dimension, the random forces go to zero faster than the interactions, resulting in a rigid set of spins that will point in the same direction. Below this dimension, the random forces will dominate the interactions over long length scales resulting in a very heterogeneous set of spins. Therefore, $d = 2$ is the upper critical dimension. Note that for short range interactions, this is no longer true as the interactions scale as L^{-d-2}, and the upper critical dimension is instead $d_c = 4$. Renormalization calculations agree with this heuristic argument [6, 13, 40].

1.6 Overview of This Thesis

In this thesis, we will examine two related but different problems involving avalanches. The first is the application of the avalanche model developed for plasticity and magnets [13] to stellar avalanches. We will begin by describing the observations of Tabby's star [60], which is an extraordinary F class star on the main sequence. We will describe in detail the analysis we did on the *Kepler* data set of this star, the surprising discovery of the power laws in many of the avalanche statistics, and how Tabby's star compares to other F class stars on the main sequence. We will conclude by describing others' possible explanations for the behavior of Tabby's star as well as our own understanding of the star up to this point.

Second, we will apply the same analysis that led us to the conclusions for Tabby's star to our own Sun. Unlike Tabby's star, the Sun is a very ordinary G class star (i.e. it is slightly cooler). However, data on the Sun is much more readily available, and we have used data from the VIRGO instrument aboard the SoHO spacecraft [81] to extract light curves equivalent to what was done with Tabby's star. This data is very clean and provides us opportunities to explore physical mechanisms that might lead to non-secular, non-periodic dimming in stars like Tabby's star.

We will then change directions to focus on thermal effects on avalanches. Much work has been done in this direction, both theoretically [82, 83, 84, 85] and experimentally [86, 87, 88, 89, 90]. We will first describe where the current state of this work is at, and then we will discuss the practical challenges in obtaining accurate avalanche distributions theoretically, computationally, and experimentally. With this in hand, we will describe how we have developed a new algorithm that circumvents some of these challenges and offers more insight into how thermal effects change the avalanche distributions. Finally, we will describe interevent times between avalanches. We will take a deep look at the mean field model, and how avalanches can arise in such a model at finite temperature. Then with the aid of the algorithms developed above, we will describe how to theoretically derive interevent time distributions for the mean field model, and show that these distributions agree with the simulations. We will close by describing experiments that can test these predictions in real materials.

Chapter 2

Avalanches and Criticality in the Highly Variable Tabby's Star (KIC 8462852)

2.1 Tabby's Star

The Kepler spacecraft was conceived with the goal of finding extrasolar planets by measuring the time-varying light flux, defined as power received in the 423-897 nm wavelength range, from about 150,000 stars [91, 92, 93]. As mentioned above, these light curves have proved useful for other purposes, such as astroseismology [94]. Unexpectedly, these light curves are also responsible for the discovery of anomalies associated with the star KIC 8462852 [60]. KIC 8462852, also known as Tabby's star, is classified as an F class star, not too disimilar from the Sun. However, the Kepler data has shown drops in flux by more than 20%, as well as irregular smaller variations in flux in excess of similar fluctuations in many other stars [60]. The unique characteristics of this light curve have motivated much interest in Tabby's star. We show that the statistics of the fluctuations, are similar to those often seen in ferromagnets and plastic flow and to predictions from a mean field theory [16, 7, 13]. As mentioned before, we draw a formal analogy between the fluctuations in Tabby's star and avalanches in these materials. In astrophysical systems, avalanche statistics have been found to describe the distribution of energies of x-ray emission from stellar flares [5], x-rays seen from soft gamma repeaters [95], and a variety of other phenomena [96].

We list a few of the stellar properties of Tabby's star. It is labeled an F3V star, which means that it is slightly hotter than the Sun and lives on the main sequence in the Hertzsprung-Russell diagram. It also implies that the star is middle aged, similar to our Sun. It is located 1,420 light years away, and has a mass of 1.43 $M_\odot$, a radius of 1.58 $R_\odot$, a luminosity of 4.68 $L_\odot$, and a temperature of 6750 K [60] (compared to 5800 K of the Sun), where $M_\odot$, $R_\odot$, and $L_\odot$ denote the mass, radius, and luminosity of the Sun. It has a rotation period of 0.88 days [60], which we discuss below. Comparatively our Sun has a rotation period of 24 days. The temperature, luminosity, and mass of Tabby's star are relatively common for F class stars, but the rotation rate is faster than most main sequence stars in the *Kepler* catalog [97, 98] of comparable mass and temperature. The median rotation rate of F class like Tabby's star (an F3 main sequence star) is about 3 days [97], as compared to Tabby's star, which has a rotation rate of 0.88 days.

In order to analyze the avalanche properties, we extract the exponents from the light curve (flux vs. time) of Tabby's star. These exponents are extracted using the complementary cumulative distribution function (CCDF). The use of the CCDF is justified because a power law probability density function (PDF) $p(S) = (S/S_{min})^{-\tau} f(S/S_{max})$ will have a CCDF

$$C(S, S_{max}) = \int_S^\infty (S'/S_{min})^{-\tau} f(S'/S_{max}) dS' \sim S^{1-\tau} F(S/S_{max}). \tag{2.1}$$

where $C(S, S_{max})$ is the CCDF, and $F(S/S_{max}) = \int_1^\infty u^{-\tau} f(uS/S_{max}) du$. The advantage of using CCDFs instead of PDFs is that such a statistic is not sensitive to choice of binning, which is necessary to analyze PDFs. In the above analysis, the integral extends to infinity with a cutoff function $f(x)$. If S denotes the avalanche size, the regime $S_{min} < S < S_{max}$ is known as the scaling regime, over which the power law is most clearly manifest in the CCDF. In principle S_{min} is set by some physical lower limit, such as the lattice size. In practice however, it is mostly set by the noise floor, past which avalanche phenomena cannot be distinguished from other forms of noise (most notably white noise). S_{max} is set by tuning parameters, such as in plastic deformation, where the stress Σ sets the maximum avalanche size. In real systems, S_{max} is also sensitive to the system size. There may be other tuning parameters such as rotation rate, mass, or even stellar age, that can cause S_{max} to vary. A wide scaling regime indicates that the system has avalanches that span a broad range of sizes and durations, and that it is near a non-equilibrium phase transition. In some systems, very large avalanches sensitive to the system size can also occur. These avalanches are characterized as large earthquake-like, system spanning events [6, 13] that have different statistics and modified dynamics from small avalanches. Motivated by the large dimming events in Tabby's star, we have analyzed also the small dimming events (those on the order $10^{-5} - 10^{-3}$ of the median value) and compared their statistics to those of avalanches in magnets and plastic flow. As mentioned above, the avalanche sizes here represent the amount by which the radiated energy per unit surface area drops below its average value, during an avalanche, i.e. the reduction in radiant fluence (energy per unit surface area) from the quiescent stellar output. This is very much in analogy to solar and stellar flares [5, 58] and soft-gamma repeaters [95], where avalanches are defined by the total amount of energy released in excess of an average rate, rather than the amount by which it drops below the average value. We have analyzed the the statistics of these brightening events, which do not show large variations like the dimming events, and found that the statistics of these brightening events have statistics similar to the dimming events for small avalanches.

2.2 Data Analysis

In order to extract and interpret the dimming events, we define an dimming event avalanche (we refer to it as an avalanche) as a dimming event in the light curve which drops below a specified threshold. We choose the threshold to be the median value of the light curve. This was done because Tabby's star has large dimming events that will bias the mean value. The median value is used as an estimate of the quiescent stellar output. As mentioned before, it is analogous to the velocity of two interfaces sliding in plastic deformation. The use of a threshold is very common in extracting avalanches [4] from data, although it results in some unwanted free parameters. Also, in addition to the dimming events, in the appendices we show statistics for the brightening events, which are events above the threshold value.

In Tabby's star, there is a periodic 0.88 day signal, most often reported as a rotation signal [60]. We use a notch filter to remove this signal and its two higher harmonics. The presence of the 0.88 day signal may signal that Tabby's star has starspots, as stellar rotation does not usually cause periodic modulation of this magnitude otherwise [97]. If the 0.88 day signal is from rotation, it is likely that Tabby's star has a large magnetic field [64]. Because of the high rotation rate, techniques for measuring this magnetic field, such as Zeeman-Doppler imaging [99] might prove unreliable, but as far as we are aware this magnetic field has not been measured in any detail.

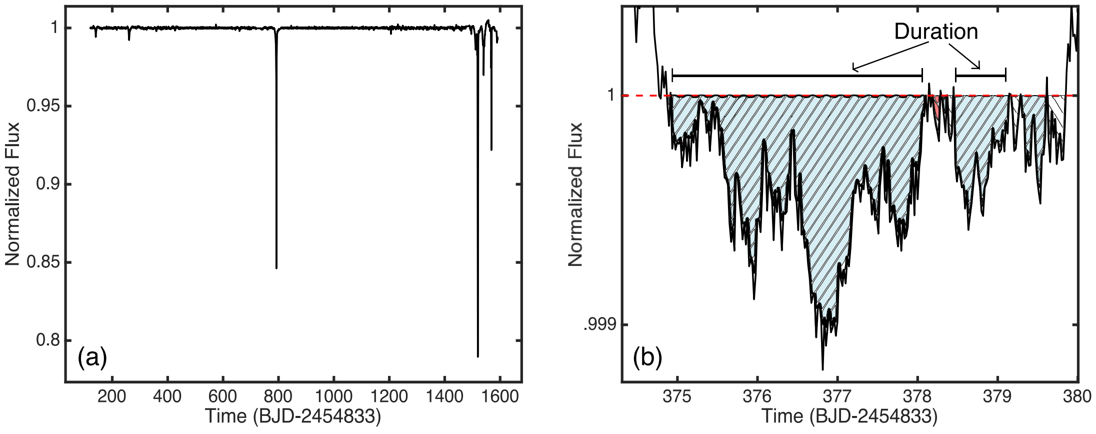

Figure 2.1: (a) The light curve of Tabby's star over the entire observation period we analyzed. We normalized the flux to the median flux in this data. (b) An example of avalanches in Tabby's star. Here the red line denotes the threshold value, which we have set to the median flux value. Taken from [59].

The entire observation period of the *Kepler* data spans a four-and-a-half year period, yielding about 1,000 avalanches. In that four-and-a-half year period, there have been 9 large avalanches, with troughs greater than 1% of the total solar output. We show above in fig. 2.1 the light curve and an example of avalanches. The large events immediately stand out, and large orbiting bodies resulting in these events have been ruled out since the discovery of the light curve [60]. We discuss possible explanations below.

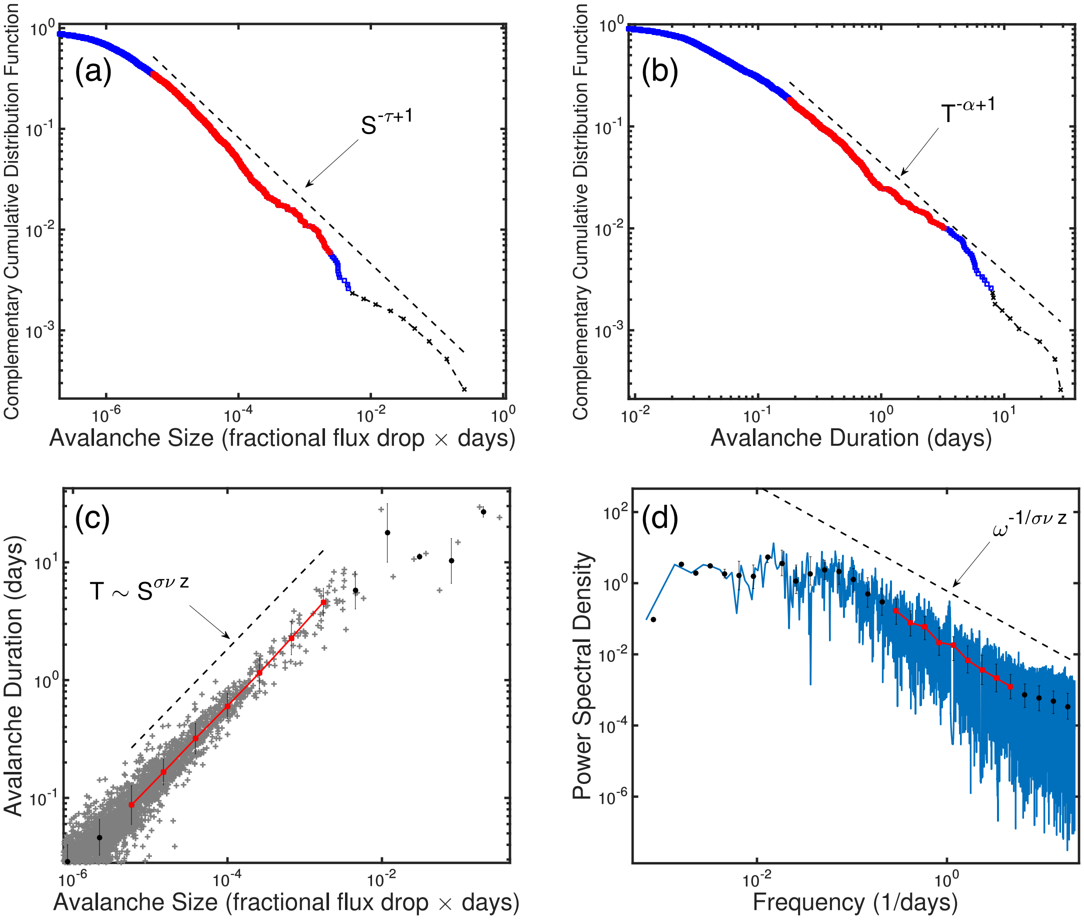

Figure 2.2: All plots are on a loglog scale. The highlighted (red) region denotes the scaling regime (a-d). In (a) and (b) the black crosses represent the 9 largest avalanches. In (a), (b), and (c) the dashed line denotes the power law with the measured exponent (Table 2.1). (a) The CCDF of avalanche sizes. (b) The CCDF of avalanche durations. (c) The avalanche magnitude vs. duration. The dots denote logarithmic bins in size. (d) The power spectral density. Here the dashed line is the power law with exponent -1.5, which matches well with the predicted value of the slope $1/\sigma\nu z$, where $\sigma\nu z$ was defined from the slope of (c). Incidentally, the slope appears to cross over at frequencies below the scaling regime (put in exact value) to $1/\sigma\nu z$, which is the mean field value. Taken from [59].

Exponent	Tabby's star	Mean Field
τ	$1.60\pm^{0.10}_{0.13}$	3/2
α	$2.09\pm^{0.07}_{0.40}$	2
$\sigma\nu z$	$0.67\pm^{0.04}_{0.02}$	1/2
$\frac{\tau-1}{\alpha-1}$	$0.55\pm^{0.46}_{0.14}$	1/2

Table 2.1: Avalanche exponents for Tabby's star and the mean field avalanche model [17]. In order to extract the exponents τ and α we used a maximum likelihood approach [100]. The uncertainties obtained from the variation of threshold and variation of the scaling regime were much larger than that from bootstrapping, so we used these uncertainty values in the table (see the appendices). The actual error bars may be larger; the maximum likelihood method we have implemented does not take into account the decaying cutoff function [2]. Taken from [59].

Figure 2.2 shows the power law behavior of avalanche size distributions in KIC 8462852, which spans nearly 4 decades of size (highlighted in red). The exponents we extract are present in table 2.1. The exponents τ and α are close to their mean field values, while the exponent $\sigma\nu z$ slightly deviates from the mean field prediction. The exponents τ and α were extracted using the maximum likelihood method, as the exponents of power laws are not accurately captured using least squares fitting of CCDFs [100]. Details of the maximum likelihood procedure are presented in the appendicies. We do not use the standard error $(\hat{\Delta}-1)/\sqrt{N}$ of the estimated exponents $\hat{\Delta}=\tau$ or $\hat{\Delta}=\alpha$, where N is the number of samples [100]. This error is too small to be reasonable when we evaluated it, so we instead choose to vary our free parameters. These free parameters are the scaling regime and threshold that we have chosen (see the appendices). The exponent $\sigma\nu z$ is found using standard least squares fitting of $\log(T)$ versus $\log(S)$ where T and S are the duration and size. The error here is the maximum of the standard error obtained from least squares fitting and the error obtained from varying our free parameters.

The power spectral density, the magnitude squared of the Fourier transform of the light curve, is expected to follow a power law as well. The slope of this power law is $1/\sigma\nu z$ [18] and we plot this slope in fig. 2.2(d). The power spectral density plotted here is not the raw power spectral density, as the large avalanches completely mask the features of the CCDF. They have been removed before plotting the CCDF, along with the rotation signal, which is visible as notches in fig. 2.2(d). The scaling regimes are highlighted in red in fig. 2.2. The scaling regimes are found using scaling collapses, as defined below (also see the appendices). One test of consistency with theoretical predictions [14] is the exponent relation $(\tau-1)/(\alpha-1)=\sigma\nu z$. This is satisfied by size and duration distributions of Tabby's star to within error bars.

In addition to the sizes and durations of the avalanches, we can look at the average temporal profiles (shapes) of the dimming events for further confirmation of our model. The *Kepler* spacecraft took data every 30 minutes. Since the events in the regime we are interested in are on the order of hours to days, we have enough temporal resolution to analyze the specific avalanche shapes. These shapes give us a powerful method to confirm that Tabby's star indeed has avalanche processes near criticality. Near criticality, the theory of non-equilibrium critical phenomena posits that the average avalanche shapes will exhibit well-defined universal profiles [17, 4]. This universal profile is not visible for single avalanches because the avalanches are stochastic, and must be averaged over a fixed variable such as size or duration.

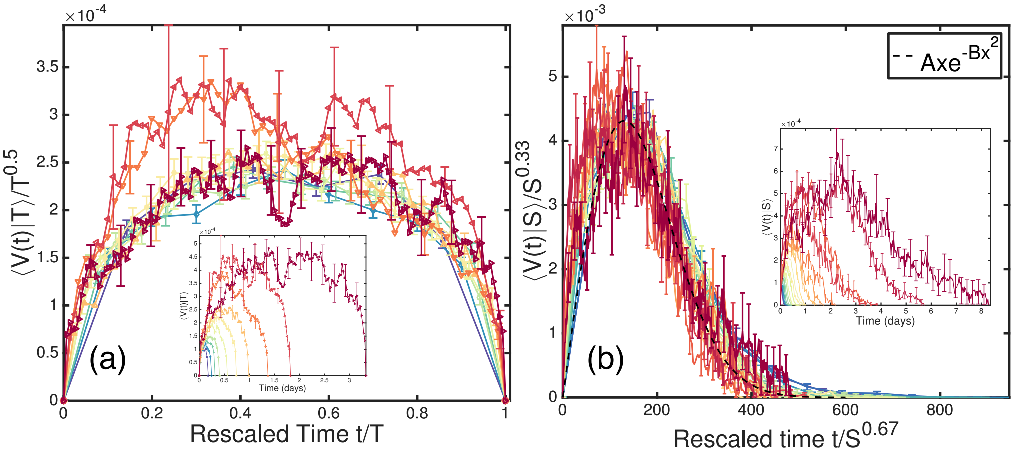

Figure 2.3: The collapses of avalanches after averaging over duration (a) and size (b). We plot every 10th error bar to prevent cluttering. The insets show the original averages before rescaling. The data is inverted from the original *Kepler* data, so that the dimming events are presented as positive excursions instead of negative excursions. Redder colors correspond to longer avalanches, while bluer colors correspond to shorter avalanches. The value of the factor $\sigma\nu z$ was taken to be 0.67, the measured value. In (a) the rescaled time is t/T, where T is the total duration. The scaling factor $T^{0.5} = T^{1/\sigma\nu z - 1}$. In (b) the dashed black line shows the best fit mean field theory prediction for the collapsed function. The rescaled time is $t/S^{\sigma\nu z} = t/S^{0.67}$ and the scaling factor $S^{1-\sigma\nu z} = S^{0.33}$. Taken from [59].

There are two types of averaging to find universal profiles, both dependent on the exponent relation $S^{\sigma\nu z} \sim T$. First, in fig. 2.3(a) we plot the average over duration T. We denote $V(t)$ to be the median light flux minus the actual light flux as a function of time t during a dimming event [4]. Given that the average avalanche profiles are expected to be universal [4, 1], we expect that $\langle V(t) \mid T \rangle = \mathcal{G}(t/T)$, where $\mathcal{G}(t/T)$ is our scaling function. Then in analogy with other scale invariant quantities, we expect that as T varies, we can rescale $\mathcal{G}(t/T)$. If $T \to T'$, then $\mathcal{G}(t/T) \to (T'/T)^{\Delta}\mathcal{G}(t/T)$. Here $\Delta = 1/\sigma\nu z - 1$, as $T^{1/\sigma\nu z} \sim S$ and

S/T is approximately the avalanche amplitude.

In practice, there are no avalanches that have the exact same duration. Therefore, we average over bins between $0.85T < T < 1.15T$ for varying T. We space the value of T so that the bins do not overlap, thereby ensuring independence between bins. The avalanches are first interpolated to a fixed number of time points so that they can be averaged. The scaling collapse, which is the main fig. 2.3(a) is produced by dividing the avalanches by a factor of $T^{1/\sigma\nu z-1}$ and rescaling time to t/T, where $\sigma\nu z = 0.67$. Scaling collapses with $0.60 < \sigma\nu z < 0.71$ are also reasonable. In fig. 2.3(a) the inset shows the original averages before rescaling.

A second natural type of averaging involves averages over avalanches of the same size S [17, 18, 4], which we show in fig. 2.3(b). We average over bins between $0.85S < S < 1.15S$. To average over size, we first zero padded the avalanches to the longest avalanche in the bin before averaging. After averaging, we rescaled the temporal coordinate by $S^{\sigma\nu z}$, which is again derived from the relation $T \sim S^{\sigma\nu z}$. As above, the avalanche amplitude is also rescaled by a factor of $S/T \sim S/S^{\sigma\nu z} = S^{1-\sigma\nu z}$. Here we used the value of $\sigma\nu z = 0.67$. Scaling collapses with $0.60 < \sigma\nu z < 0.71$ are also reasonable. The inset of fig. 2.3(b) shows the original averages before rescaling.

We have used these scaling collapses to find the scaling regime in fig. 2.2. In order to do this, we checked for consistency, by first choosing a scaling regime that we found reasonable, seeing if the shape collapses worked for this scaling regime, and varying until the avalanche shapes collapsed within the selected scaling regime. We found this method to be effective here, and it provided a method of finding the scaling regime with fewer free parameters to adjust.

2.3 Potential Explanations

2.3.1 Overview of Potential Explanations

Beyond the dimming seen in Tabby's star on the scale of the *Kepler* observations, there are reports that have confirmed that a longer term dimming of Tabby's star can be seen over several 10s of years [101]. This discovery, and subsequent confirmation [102] (although not without debate [103]) added to the enigma of Tabby's star. If we ignore the longer term dimming for the moment, there are a few possible explanations of the dimming events in the Tabby's star light curve. Exoplanets are often ruled out because the size of these planets would be too large and because of the lack of periodic dimming events.

Two of the most popular explanations for the anomalous dimming of Tabby's star are dust and exocomets (i.e. comets orbiting Tabby's star). Dust is often ruled out because of the lack of infrared (IR) excess [104], which is a simple result of black body radiation between the dust between the star and our line of sight to the star. A large cloud of dust orbiting (loosely) Tabby's star would absorb much of the light emitted by the star. It would then reradiate at a lower peak wavelength owing to its lower temperature. As Tabby's star has dimming events on the order of 20% of the total light flux, one would imaging a significant amount of IR excess in the black body curve of Tabby's star, which is not observed. However it was argued recently that dust is a possible explanation within the parameters of plausible dust models [105].

The other possibility of occulting material causing the dimming of Tabby's star is exocomets, originally proposed in the first analysis of Tabby's star [60]. However, to cause the larger dimming events in Tabby's star, there would have to be a swarm of such comets that orbited the star in a highly elliptical orbit. This elliptical orbit would explain why no dimming events are observed for long periods of time, and why such dimming events happen over an incredibly short duration. Recent models show that this is a possibility [106], but more data is needed, especially of larger dimming events. Post *Kepler* data, taken from the period of 2016 to 2018, shows that dimming events are presently occurring in Tabby's star, although with peak amplitudes of about 2-3% of the star's total flux [107]. However, it is interesting to note that these observations were taken over multiple bands, and they showed a preferential reddening (i.e. blue light from Tabby's star exhibited larger dimming), which runs counter to the exocomet hypothesis.

We presented in our paper [59] the possibility that these events are intrinsic to the stellar photosphere. It was independently proposed that such dimming events could be caused by the intrinsic reduction of heat transport efficiency in the star [108]. We do not speculate as to the exact physical mechanism here.

2.3.2 Similarities to Other Stars

Besides Tabby's star, we have analyzed the light curves of several stars monitored by *Kepler*. We have not systematically explored every star in the *Kepler* catalogue, but we have focused particularly on stars with fast rotation rates [64] and magnetic activity [65]. We looked through a total of 123 stars. Three stars, KIC 4638884, KIC 7771282 [64], and KIC 5955122 [65], were found to have avalanche shape collapses and statistics that matched the avalanche model predictions. Most of the stars that we analyzed do not exhibit evidence of avalanches, either lacking the statistics or having avalanche shapes that did not collapse. For these three stars, we plot the relevant statistics and shapes in the appendices.

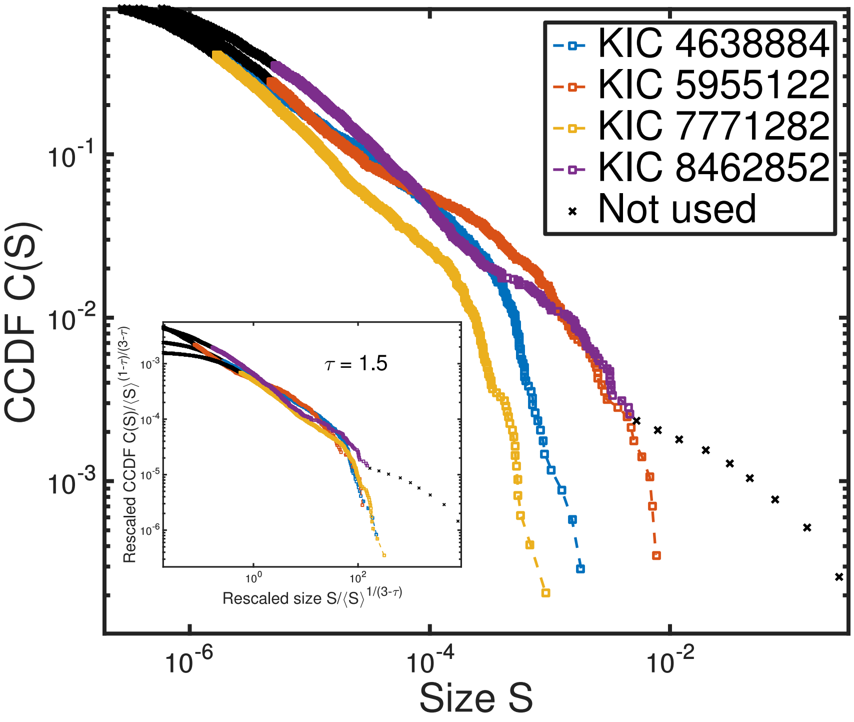

Figure 2.4: The size CCDFs of the four stars labeled in the figure. Data points marked with a squares were used in the calculation of the moments. Data points marked in black crosses were not included in the calculation of the moments. The scaling regime of KIC 8462852 is between $5 \times 10^{-6} - 2.4 \times 10^{-3}$ in size. The other stars have similar scaling regimes, approximately between $5 \times 10^{-6} - 1 \times 10^{-4}$. In the inset the rescaled CCDFs were plotted to show that there is a possible relationship between these four stars. We chose the mean field exponent $\tau = 1.5$ in the collapse, but values between $1.3 < \tau < 1.6$ produce reasonable results. In KIC 8462852, the 9 largest avalanches were not used in the calculation of the moment. Taken from [59].

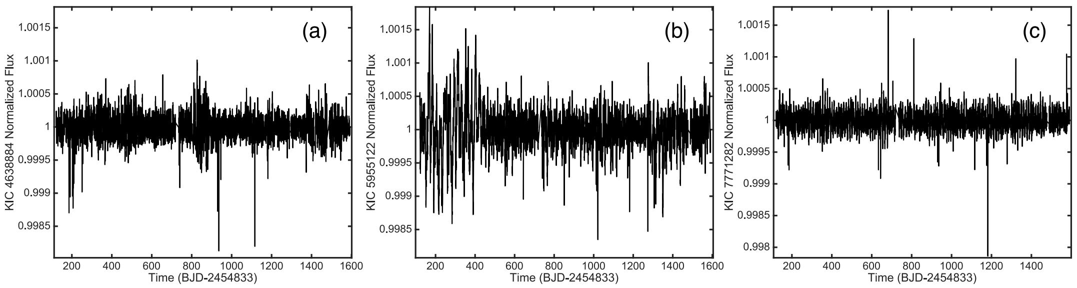

Figure 2.5: The light curves of the three stars we analyzed in the text. (a) The light curve of KIC 4638884. (b) The light curve of KIC 5955122. (c) The light curve of KIC 7771282. The light curves all show larger than usual variations in luminosity due to magnetic activity.

Exponent	KIC 4638884	KIC 5955122	KIC 7771282	Tabby's Star
τ	$1.50\pm^{0.14}_{0.09}$	$1.72\pm^{0.12}_{0.18}$	$1.63\pm^{0.08}_{0.24}$	$1.60\pm^{0.10}_{0.13}$
α	$1.68\pm^{0.28}_{0.18}$	$2.08\pm^{0.5}_{0.3}$	$2.02\pm^{1.17}_{0.29}$	$2.09\pm^{0.07}_{0.40}$
$\sigma\nu z$	$0.71\pm^{0.04}_{0.07}$	$0.75\pm^{0.04}_{0.06}$	$0.74\pm^{0.04}_{0.08}$	$0.67\pm^{0.04}_{0.02}$
$\frac{\tau-1}{\alpha-1}$	$0.74\pm^{0.58}_{0.32}$	$0.67\pm^{0.40}_{0.32}$	$0.62\pm^{0.35}_{0.29}$	$0.55\pm^{0.46}_{0.14}$

Table 2.2: We list the exponents and uncertainties of the exponent values for each of the stars analyzed that matched closely with Tabby's star. The exponents and uncertainties are obtained using methods detailed in the appendices. The lower and upper errors are the largest deviations observed using these methods. The value of $(\tau-1)/(\alpha-1)$ is listed because for avalanche dynamics it is expected that $(\tau-1)/(\alpha-1) = \sigma\nu z$ [14], and this is satisfied to within error bars for each of the 4 stars. The CCDFs of duration, size versus duration, and power spectral densities are plotted in the appendix to chapter 2. Taken from [59].

In fig. 2.4, fig. 2.5, and table 2.2 above, we show information about the stars we analyzed. We plot the size CCDFs for the 4 stars (Tabby's star is KIC 8462852) in fig. 2.4 and the light curves of each of these stars in fig. 2.5. Each of these stars had been marked as magnetically active stars with slightly larger than usual variations in the light flux. Note however that the variations are still small (on the order of $10^{-5} - 10^{-4}$ of the total flux) relative to Tabby's star, with the largest small events being the rarest due to the power law decay. We plot the remaining statistics in the appendices. If the stars are near an underlying critical point, then universality predicts that the avalanche distributions are of the form $C(S, S_{max}) = S^{1-\tau}F(S/S_{max})$ for $S > S_{min}$ [14, 54]. Similar to how the avalanche shape collapses worked, this scaling form allows us to perform a scaling collapse, which we show in the inset of fig. 2.4. In order to perform this scaling collapse, we used the second moment $\langle S^2 \rangle$ as a proxy of S_{max}. The nth avalanche moment scales as

$$\langle S^n \rangle = \int S^n p(S) dS = \int S^{n-\tau} f(S/S_{max}) dS \sim S_{max}^{n+1-\tau} \tag{2.2}$$

implying that S_{max} scales as $\langle S^2 \rangle^{\frac{1}{3-\tau}}$. Therefore we rescale the sizes of avalanches of each star by the second moment found within the scaling regime [54]. In fig. 2.4 we show the sizes we excluded as the black crosses. Values of τ that produced acceptable scaling collapses were approximately $1.3 < \tau < 1.6$, but we used the mean field value of 1.5 in the inset of fig. 2.4. In order to do the scaling collapse, we excluded the Gaussian noise regime for each of the stars (avalanches on the order of 10^{-10} to 10^{-6}) and we also excluded the 9 largest avalanches in Tabby's star. We did this because the data suggests that the largest avalanches seen in Tabby's star have modified dynamics, which could be similar to weakening and hardening in plastic flow [13], and large avalanches would also be sensitive to the system size.

The scaling collapse in fig. 2.4 implies several important conclusions. First, the stellar variability in the stars KIC 4638884, KIC 7771282, and KIC 5955122 are the result of magnetic activity in the star. Magnetic activity has been known for a long time to cause variability in total solar output [109]. If the scaling collapse is to be believed, then the stellar variability in Tabbys star may also be the result of magnetic activity, or the underlying thermodynamic processes that cause the magnetic activity. Second, the variability of stars in the *Kepler* catalogue that display power laws suggest that if Tabbys star is the result of avalanches on the stars photosphere, it is likely due to tuned criticality rather than self-organized criticality. We do not speculate what these tuning parameters are, but near a critical phase transition, avalanche sizes would diverge quickly. This would also explain the relative rarity of a light curve such as Tabby's star.

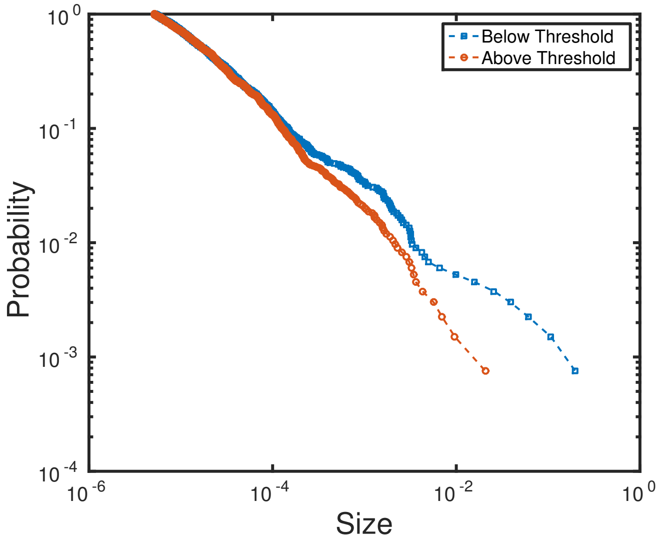

Figure 2.6: The CCDFs of the dimming events to the brightening events in Tabby's star, where dimming events are labeled as below threshold, and brightening events are labeled above threshold. We see the that small events (those with size less than 10^{-4}) are almost identical for the dimming and brightening events, but past this size the relative frequency of the larger dimming events is bigger than those of the brightening events.

In fig. 2.6 we plot the brightening events, that is those events above the threshold value.To be precise, they are defined as the excursions of the light curve above the median value. We see that there is a remarkable similarity between the CCDFs of the brightening events for small events (those with size less than 10^{-4}) but there is a divergence at this point.

Importantly, we analyzed the small dimming (and above, the brightening) events in Tabby's star, but it was the large dimming events that drew our attention in the first place. Based on the data, the small events follow a model of avalanche dynamics described above, although the exponents are not exactly mean field exponents. The large events, even with the new observations [107] do not constitute enough events to perform a statistical analysis. We can speculate that the large events are similar to large avalanches observed in bulk metallic glasses [15], and could be caused by weakening. Here, the weakening would be a free parameter in the theory that can cause runaway events that span the system size and deviate from power law scaling.

In many other stars, stellar variability is often attributed to regions of intense stellar magnetic activity [110, 111] or exotic stars with large magnetic fields [95]. There is a rough agreement between all of the exponents that we have observed, and those reported for stellar superflares [58, 112, 67, 68]. Here superflares are large stellar flares that are visible even against the bright light of the originating star. *Kepler* superflare studies have reported exponents of $\tau \sim 1.6 - 2.3$, $\alpha \sim 2$, and $\sigma\nu z \sim 0.5 - 1$ [58, 112, 67, 68]. The value of $\tau = 1.60$ is close to the value of 1.67 given for the energy released by bursts of x-rays from soft gamma repeaters [95].

This is not to suggest that each of these stars has the exact same physical mechanism underlying its activity. It is unlikely that soft gamma repeaters, which are neutron stars, and stars with superflares, which are usually main sequence stars, behave similarly. Rather, it is an appeal to universality, that the avalanche type behavior seen in all of these examples is the result of interactions, which may be long range, and similar in dimensionality, symmetry, and quenched disorder. The argument for the stellar magnetic field as the source of avalanches in Tabby's star is supported by fig. 2.4, where the magnetically driven stars' CCDFs collapse well with Tabby's star. It is also supported by table 2.2, which shows that we have extracted avalanche exponents from each of the stars' light curves that, although not in perfect agreement, do agree to within error bars of each other.

In order to further examine the possibility that the stellar variability is intrinsic, and look at possible mechanisms of this variability, we have also explored a different dataset. This dataset, taken from the Variability of Solar Irradiance and Gravity Oscillations (VIRGO) photometer on the Solar and Heliospheric Observatory (SoHO) spacecraft has similar properties to the *Kepler* data. It is a look at the total output of the Sun, known as the total solar irradiance, and it will be the subject of the next chapter. We have found that even in the Sun, there may be avalanches, and unlike Tabby's star, the variability of the Sun is better understood.

Chapter 3

Avalanches in VIRGO Data from the Sun

3.1 VIRGO Data and Purpose

As in the previous chapter, we apply the methods of avalanche behavior to the light from Sun. We use data collected by the VIRGO (Variability of Solar Irradiance and Gravity Monitoring) instrument [81] over the years of 1996 - 2008. The VIRGO instrument collects light curve data (flux vs. time) similar to *Kepler* aboard the SoHO (Solar and Heliospheric Observatory) spacecraft. In the case of VIRGO, the data is collected from two three-channel sun photometers, which measure the total spectral irradiance (TSI) around 402, 500, and 862 nm.

Similar to *Kepler*, VIRGO measures the data continuously with a frequency of once per minute, and it has done so for the past 18 years. Of the 18 years available from VIRGO, we obtained access to 12 years of unfiltered data from the 500 nm sun photometer. The original purpose of VIRGO was for gathering helioseismology data [81] on the Sun to probe the stellar interior [81, 94, 69]. Unlike the application of our avalanche methods to Tabby's star, the Sun is relatively well understood, and we have found evidence that similar – though not exactly the same – type of avalanche behavior occurs on the Sun's photosphere (the Sun's surface).

The Sun is a relatively normal G class star, and has a temperature of 5800 K, slightly below Tabby's star. By comparison with Tabby's star, light from the Sun does not experience huge dimming. However, small dimming events in the Sun still show statistics that follow the predictions of an avalanche model [13]. Importantly, the VIRGO instrument has the fidelity to measure these dimming events. The small oscillations in the Sun's brightness due to standing waves on the Sun [81] are on the order of $10^{-5} - 10^{-4}$ of the total solar irradiance (TSI) and of similar amplitude to the dimming events we observe.

Also unlike Tabby's star, where the cause of the dimming events are unknown, we believe that the small dimming events on the Sun's photosphere are the result of a continuum of events of varying size, with the largest events being the groups sunspots that are so readily visible on the Sun [113].

As we have mentioned before, there are already dramatic examples of avalanche phenomena in solar and stellar physics. Here we describe in detail how the generation of solar flares can be interpreted as an avalanche phenomenon [5]. Solar flares are sudden releases of energy in the Sun's corona, which is a layer of plasma that surrounds the Sun [114].

Solar flares are likely caused by magnetic reconnection of the magnetic field that threads around the Sun. This magnetic field may have discontinuities, which are possible when sheets of charged particles thread between them. When the discontinuity angle between two fields exceeds an angle $\theta > \theta_c$, there is a catastrophic reconnection event that ejects charged particles out into space [5]. As mentioned before, the energy released by these events (as measured in the X-ray band) [115] shows scaling with an exponent measured between 1.5 and 2 [114] over 12 decades of energy scales. We propose similar scaling is present for sunspots and other dimming events on the Sun's photosphere.

3.2 Data Analysis

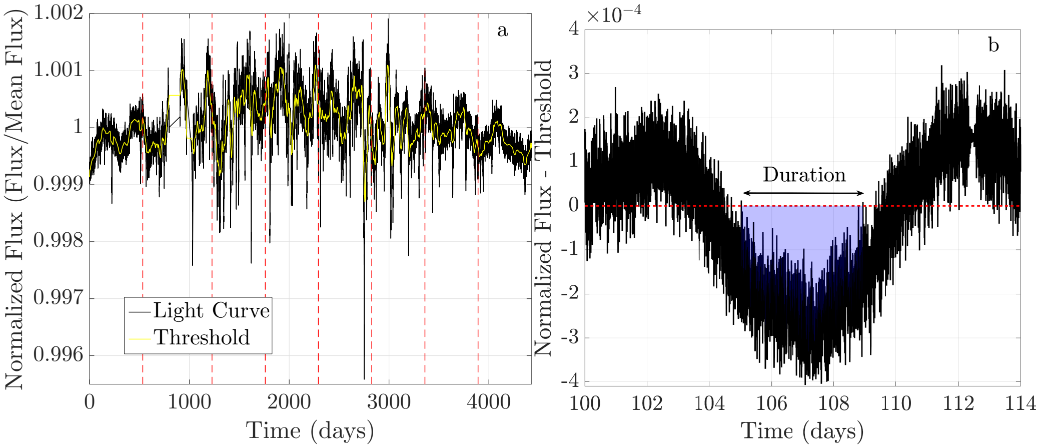

Figure 3.1: (a) The light curve of extracted from the VIRGO data over the entire observation period of 12 years. We normalized the flux to the mean flux in this data, so what is plotted is $F(t)/F_{mean}$. The yellow curve is $\bar{F}(t)/F_{mean}$ and is the smoothed data used as the threshold value. The smoothing window size was 40000 minutes, or about 28 days. The 8 red demarcations represent the 8 regions we have split the data into. In region 2 there were several days of missing data, so we extended this region to include more data. (b) An example of avalanches in the VIRGO data. Here the red line denotes the threshold value, which we have set to the median flux value.

Similar to how the analysis was done in Tabby's star, we define a dimming event as the total loss of radiant flux relative to the quiescent flux of the Sun. The quiescent flux can be found using either the mean or the median value. The median value was used in the *Kepler* data analysis, but we choose the mean value here to make the interpretation simpler. Note that because of the lack of large outliers, using the mean value or the median value does not change the results of the analysis. The duration is again defined as the time the light curve spends below the threshold, which we have taken to be the mean value of the flux. Fig. 3.1 shows the full light curve as well as an example of an avalanche in the VIRGO data.

The data was taken during solar cycle 23, beginning in 1996 and ending in 2008 (the cycle lasted 12 years). The solar cycle is a variation of solar properties that repeats once every 11-12 years, during which the Sun's magnetic field flips polarity [113]. The full period is in fact double (22-24 years) because of this polarity switching, but most properties do not depend on the polarity of the Sun's magnetic field. The primary variations in the Sun are thought to be the presence of sunspots and flares (solar activity) and variations in the total solar irradiance [109]. The TSI varies in phase with the solar cycle, with an amplitude of about 0.1 % of the mean output of 1361.5 W/m^2 [116, 117, 118].

As visible in the data above, the solar cycle causes large variations in the data that cannot be ignored when trying to extract avalanches. In order to analyze the VIRGO data, we sliced it into 8 equal regions of about 550 days. We chose 8 regions as a compromise between gathering enough avalanches within a region and our temporal resolution between regions. Note that in region 2, we were missing about 150 days of data, so this region has a range of about 700 days instead of 550 days.

The solar cycle has clear minima and maxima. The minima correspond to times during which the Sun's overall magnetic field is like a dipole similar to a bar magnet. The maxima correspond to times during which the solar magnetic field is unstable, as it is in the process of switching between polarities. This magnetic field is generated by complex fluid motions of the stellar interior and the rotation of the Sun, known as the solar dynamo [119]. In this data, regions 1 and 8 correspond to the solar minima, while regions 2-7 correspond to either transitory periods or the solar maxima. As is expected, the TSI varies far more during the solar maximum than the solar minimum.

To handle the overall variation of the TSI during the solar cycle, in addition to splitting the data into several pieces we also needed a more flexible approach to choosing our threshold. As is easily visible in fig. 3.1, the data varies on the largest time scales available, and any constant threshold (i.e. the mean solar output) would only pick up these very large variations. Since we are looking for small variations (on the order of $0.01 - 0.1\%$ of the TSI), we needed to subtract the largest variations, often called secular variations in the VIRGO data. In order to do this we used a simple window filter with a window of about 27 days, as we were mostly interested on variations smaller than this scale. If we call the raw VIRGO data $F(t)$, this window filter produced data which we call $\bar{F}(t)$. Finally, we also extracted the mean value of the data over the entire period of observation, which we call F_{mean}. This mean is used to normalize the data so that we can look at solar variations as a function of the total fraction of solar output. First we divide both $F(t)$ and $\bar{F}(t)$ by the mean value F_{mean} to normalize the data. Then we subtract $F(t)/F_{mean} - \bar{F}(t)/F_{mean} = (F(t) - \bar{F}(t))/F_{mean} = \bar{V}(t)$. This is the same normalization used in the previous chapter [59]. We also filter the short frequency data here, with a window filter of size 30 minutes. This window filter smooths short term oscillations of the type used for helioseismology [81]. We call the final signal we obtain $V(t)$.

We grant that there are several free parameters in this data analysis that were set by hand. First, the choice of window size to extract the threshold, and second, the choice of window size to filter small oscillations. These small oscillations are the result of linear gravitational and pressure waves that constantly occur on the photosphere [81] that do not correspond to avalanche phenomena, which are nonlinear. In order to provide more certainty that the exact choice of such parameters does not reflect, in the appendices we show that varying these parameters of choice does not significantly alter the distributions of size or duration. Specifically, we have varied the filtering window for the threshold $\bar{F}(t)/F_{mean}$ from 13 days to 40 days, and found very little variation in the distributions. We have also varied the offset of the threshold by a factor of 10^{-5}. Finally, we have varied the filtering window at high frequencies from 10 minutes to 60 minutes with little variation of the size and duration distributions. We believe the conclusions we reach are robust to these variations, and have included the variations of the distributions in our estimation of the error bars of the exponents that we extract.

In each of the 8 regions, we have between 600 and 3000 avalanches, with regions 1 and 8 having the largest number of avalanches. The intermediate regions have fewer avalanches because many of the events in these regions are larger, and therefore less likely to return to the mean threshold.

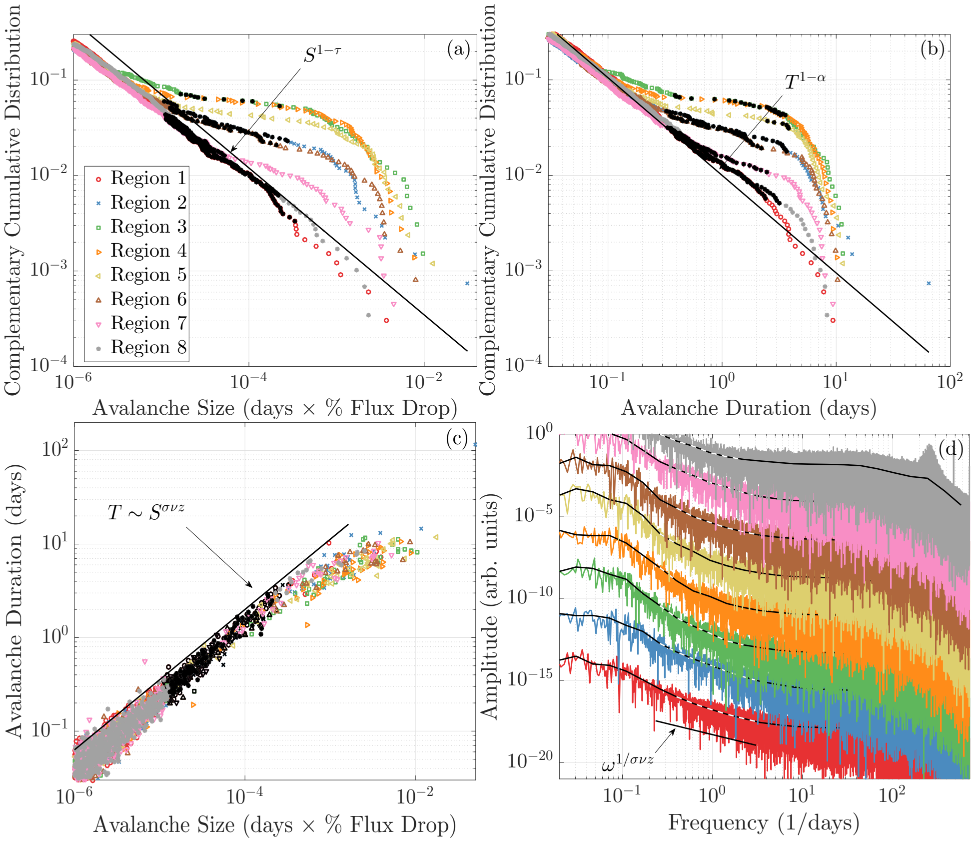

Figure 3.2: We show the dimming event avalanches for all 8 regions. Brightening events are shown in the appendices. The solid black lines are guides for the eye, with slope as the average exponent of regions 1 and 8. The highlighted black symbols denote the scaling regime for regions 1 and 8, and denote the range over which we took avalanches for all the regions for studying the avalanche shapes. (a) The avalanche size CCDFs.. The avalanche sizes grow larger as the solar maximum approaches, but this also destroys the power law behavior. (b) The avalanche duration CCDFs, which show behavior that is similar to the size CCDFs. (c) The size versus duration. (d) The power spectral density (PSD) for each of the 8 regions. There was a multiplicative offset (which is a constant offset on a loglog) applied to each region as the PSDs would overlap otherwise. We show the PSDs before we apply high pass filtering to their light curves, showing the solar oscillations at the highest frequencies visible in the PSDs (with about 5 minute periods). The solid black lines show the binned PSDs which are averaged over several intervals of frequency to remove noise, while the black line on the bottom left denotes the expected slope $1/\sigma\nu z$ of the PSDs in the scaling regime. The alternating white and black regions of the binned curve show the scaling regime as $1/T_{max}$ to $1/T_{min}$ extracted from (b).

Exponent	Region 1	Region 8	Tabby's Star	Mean Field
τ	$1.74\pm^{0.30}_{0.2}$	$1.80\pm^{0.2}_{0.3}$	$1.60\pm^{0.10}_{0.13}$	3/2
α	$2.00\pm^{0.3}_{0.5}$	$2.04\pm^{0.5}_{0.4}$	$2.09\pm^{0.07}_{0.40}$	2
$\sigma\nu z$	$0.79\pm^{0.04}_{0.04}$	$0.80\pm^{0.04}_{0.03}$	$0.67\pm^{0.04}_{0.02}$	1/2
$\frac{\tau-1}{\alpha-1}$	$0.74\pm^{1.3}_{0.3}$	$0.77\pm^{0.8}_{0.5}$	$0.55\pm^{0.46}_{0.14}$	1/2

Table 3.1: Avalanche exponents for regions 1 and 8 and the mean field avalanche model [16, 17, 1, 13] . In order to extract the exponents τ and α we used a maximum likelihood approach [100]. The uncertainties were obtained from the variation of threshold, the scaling regime, and the two filter windows, which were the highpass filter and filter to determine the threshold (see the chapter 3 appendices). The actual error bars may be larger; the maximum likelihood method we have implemented does not take into account the decaying cutoff function [2]. For convenience, we have also included the exponents extracted from Tabby's star using a similar analysis, which we reported in the previous chapter [59].

Below we plot the avalanche statistics for fig. 3.2. Here we again focus on the three exponents we can most easily extract from the data, τ, α, and $\sigma\nu z$, which come from the size, duration, and size versus duration plots. As mentioned above, the power law is expected to only hold in the scaling regime, and we only consider two regions, regions 1 and 8, to show true scaling behavior. These regions correspond to the solar minima. In table 3.1 we report the avalanche statistics for regions 1 and 8, as well as the mean field model.

Like Tabby's star, we determine this scaling regime from the avalanche collapses and the statistics, by alternately choosing a scaling regime and then checking if the avalanches collapse within this regime until a consistent scaling regime is chosen. This has the added benefit of reducing the degrees of freedom in our statistical analysis. These scaling regimes are shown in fig. 3.2 as the black markers. Regions 1 and 8 clearly have scaling behavior over at least two decades of size (fig. 3.2a-b) while the other regions show larger avalanches that seem to deviate from pure power law scaling. Avalanches larger than the avalanches in the scaling regime are fairly narrowly distributed, since the corresponding CCDFs drop off quickly and the PDFs are the negative derivatives of these quantities. Typically, large avalanches are those that are longer than 3 days in fig. 3.2a-b. These large avalanches may be the result of either merging of small events, which is a constraint of looking at the total integrated solar flux, or because they are the result of a runaway nucleation process similar to those in plasticity and magnetism [13]. The primary limitation on our scaling regimes in this case was the power spectral density (fig. 3.2d), which shows an anomalous curving for avalanches of duration shorter than 8 hours. The black lines represent the binned PSD, which is averaged over several frequency intervals in order to remove the noise. The broken black and white line in fig. 3.2d is the expected scaling regime $1/T_{max}$ to $1/T_{min}$ from fig. 3.2b. The PSD is expect to scale as $f^{-1/\sigma\nu z}$ [18], which approximately happens over the small scaling regime, as plotted by the black line on the lower left corner of fig. 3.2d. The exponents are also consistent, with the standard exponent relation $(\tau - 1)/(\alpha - 1) = \sigma\nu z$ [14, 120] holding well within error bars.

One observation is that the avalanche processes causing dimming events on the Sun are the result of tuned criticality [16] rather than self-organized criticality. This is most clearly visible in the size and duration CCDFs (fig. 3.2a-b), where the variation with the solar cycle is clearest. Similar to Tabby's star, an underlying tuning parameter must be varying during the solar cycle that causes variations in S_{max} and T_{max}.

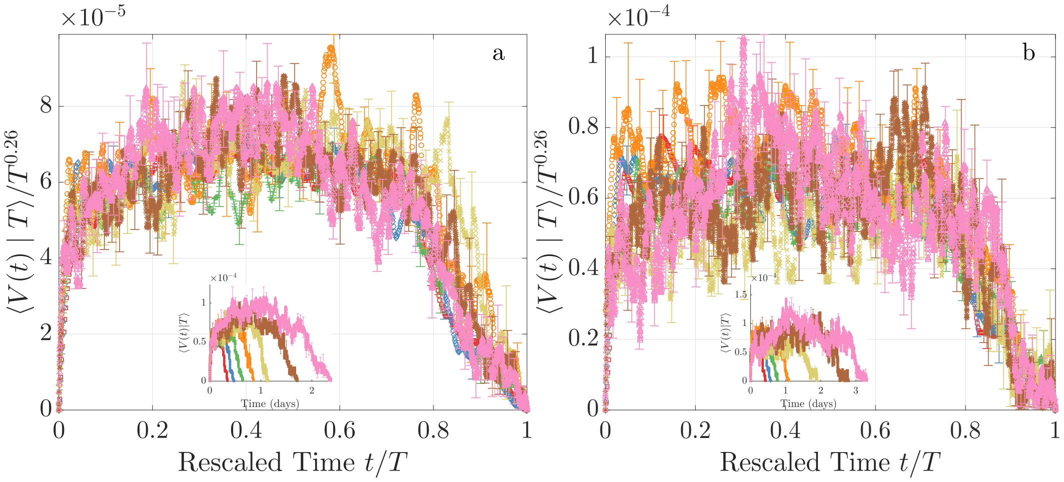

Figure 3.3: The scaling collapse of avalanche shapes for fixed duration $\langle V(t)|T\rangle$. (a) The region 1 scaling collapse. (b) The region 8 scaling collapse. The other scaling collapses are plotted in the appendices. We used the value of $\sigma\nu z = 0.79$ for these scaling collapses, which resulted in the avalanche height being rescaled by $T^{1/\sigma\nu z - 1} = T^{0.26}$, while the durations were all normalized to the between 0 and 1 (so $t \to t/T$). The insets show the avalanches before the rescaling. Each avalanche is color coded consistently between the main figure and the inset. We found that only regions 1 and 8 had satisfactory scaling collapses. The other regions did not have shapes that collapsed well, even though the value of $\sigma\nu z$ does not vary between regions by much (see fig. 3.2). This result can be explained by the fact that regions 1 and 8 have the largest scaling regimes, and therefore are expected to be closest to a critical point. Shape collapses are expected to work best close to a critical point [4].

We show in fig. 3.3 the avalanche shapes in regions 1 and 8 for averaged duration $\langle V(t)|T\rangle$. The analysis for each of the regions was described in the previous chapter. Regions 1 and 8 also produced the largest number of avalanches, and we extracted avalanches from all regions in the highlighted (black) part of the CCDFs in fig. 3.2. We performed a scaling collapse for each of these regions, which we show in the appendices. In order to perform a scaling collapse, we used the averaged measured value of $\sigma\nu z = 0.79$, but scaling collapses using $0.70 < \sigma\nu z < 0.85$ worked reasonably well, and may give us a different bound on the uncertainty in $\sigma\nu z$.

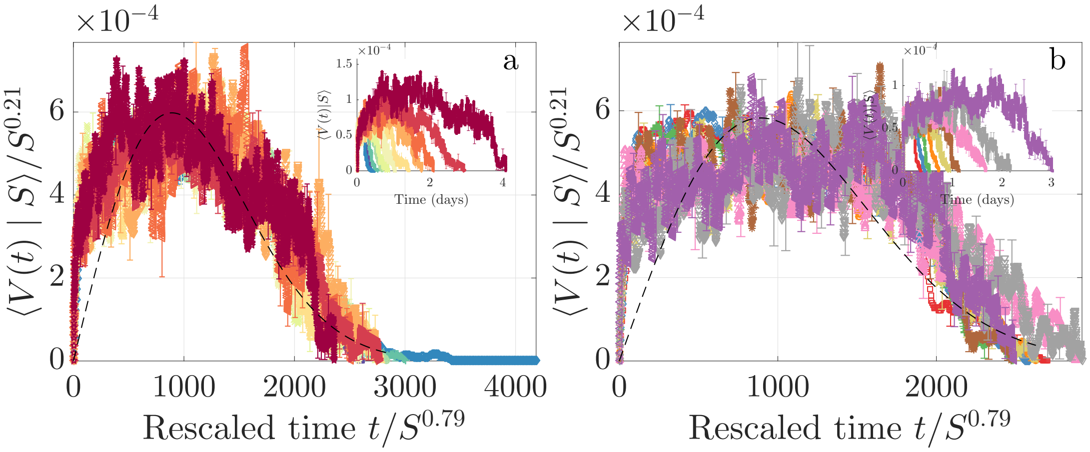

Figure 3.4: The scaling collapse of avalanche shapes for fixed size $\langle V(t)|S\rangle$. (a) The region 1 scaling collapse. (b) The region 8 scaling collapse. The other scaling collapses are plotted in the appendices. We used the value of $\sigma\nu z = 0.79$ for these scaling collapses, which resulted in the avalanche height being rescaled by $S^{1-\sigma\nu z} = S^{0.21}$, while the durations were all normalized to the between 0 and $S^{\sigma\nu z}$ (so $t \to t/S^{\sigma\nu z}$). The insets show the avalanches before the rescaling. Each avalanche is color coded consistently between the main figure and the inset. We found that only regions 1 and 8 had satisfactory scaling collapses. The other regions did not have shapes that collapsed well, even though the value of $\sigma\nu z$ does not vary between regions by much (see fig. 3.2).This result can be explained by the fact that regions 1 and 8 have the largest scaling regimes, and therefore are expected to be closest to a critical point. Shape collapses are expected to work best close to a critical point [4].

In fig. 3.4 we did a similar analysis for the avalanche shapes in regions 1 and 8 averaged over size $\langle V(t)|S\rangle$. The analysis was exactly the same as what was done in the previous chapter. We show the other regions in the appendices. Again values of $0.70 < \sigma\nu z < 0.85$ worked reasonably well, but we used the value of $\sigma\nu z = 0.79$. We have also plotted in the dotted black line the mean field scaling form $g(x) = x\exp(-Ax^2)$, where $x = t/S^{\sigma\nu z}$ and A is non-universal [17]. This form did not fit well with the scaling collapses in this case.

3.3 Sunspot Physics

It has been established [109] that dimming variations in the total solar irradiation are likely due to sunspots or their precursors. Therefore we propose that the dimming avalanches that we see here are the result of sunspots and their precursors, known as solar pores [121].

Sunspot structure is broadly defined by a dark umbra and a lighter but still dark penumbra. The penumbra is the region that surrounds the dark umbra of a sunspot. Solar pores are sunspots without these penumbra. The formation of sunspots is thought to be complex, and many attempts have been made at simulating the underlying magnetohydrodynamic equations to find evidence of formation [122]. However, the primary cause of sunspot formation has been known for many years [113] as the emergence of magnetic flux from the Sun's photosphere. This magnetic flux inhibits heat conduction to the surface of the Sun [123] thereby causing a cooling at the surface of the sun. Although exact values from spot to spot vary, the reduction in light flux from a sunspot is on the order of $F_{ss}/F_{\odot} = 1/5$ of the photosphere's average luminosity, where F_{ss} is the light flux from the sunspot and $F_{\odot}$ is the average light flux from the Sun. Given the Stefan-Boltzmann law of $L \sim T^4$, this implies a reduction in temperature of the spot by about 30%, or a cooling from 5800 K to 4000 K. The diameter of sunspots varies wildly between $1500 - 2000$ km to over 6×10^4 km, with fields on the order of $1500 - 3000$ gauss on the surface [123]. It is worth deriving from these quantities that even the smallest dimming events in the scaling regime, those on the order of 5×10^{-5} of the TSI (see the insets of fig. 3.3) would have to result from a single spot radii of about 6000 km, or multiple spots of smaller radius that have equivalent area. This follow simply from the fact that $L_{dim}/L_{\odot} = (L_{\odot} - L_{ss})/L_{\odot}$ where L_{dim} is the dimming luminosity, $L_{\odot}$ is the average Sun's luminosity. The luminosity of the sunspot is related to the flux as $L_{ss} \sim F_{ss}R_{ss}^2$, while the total average luminosity of the sun is $L_{\odot} = F_{\odot}R_{\odot}^2$, where R_{ss} is the radius of the sunspot and $R_{\odot}$ is the radius of the Sun. Then $L_{dim}/L_{\odot} = 1 - F_{ss}R_{ss}^2/(F_{\odot}R_{\odot}^2)$. Above we have assumed that the area of the sunspot scales with with radius as $A \sim R^2$, and that the flux F_{ss} is the average sunspot flux. This is true because sunspots have been observed to have only barely fractal properties with $d_f \approx 2$ [124, 125, 126].

It is believed that sunspots grow and shrink depending on the accumulation of magnetic flux tubes [123, 127]. Different flux tubes emerge, combine, disperse, and disappear in order to maintain the fundamental constraint of Gauss's Law for magnetic fields. These magnetic fields change dynamically in response to the convective motions beneath the Sun's surface. The energy lost from the reduction in luminosity must go somewhere, and it has been thought for a long time that this energy is radiated into the chronosphere (the layer of plasma around the Sun) or back deep into the interiors of the Sun through the generation of Alfvén waves [123, 128], which are uniquely hydromagnetic waves in plasmas.

We hypothesize that such sunspots and their precursors are the result of avalanche processes similar to the mean field model [17, 1, 13]. There are two points that we wish to clarify when attributing the sunspot dynamics to avalanche processes. The first is that the dimming detected by the VIRGO data is integrated over the entire hemisphere visible to the instrument. Hence sunspots (and pores, their precursors) cannot be isolated from the data set alone. The dimming might be the result of several sunspots, and this is likely for larger dimming events given that the total flux piercing the Sun's surface must sum to zero. This is the cause of the sunspot twinning often observed [113], where one sunspot follows another sunspot, with opposite magnetic flux polarities seen in each of the spots to conserve magnetic flux. Note that for long range models, the avalanches need not be connected in space [6].

The second problem is the rotation of the Sun relative to VIRGO, which introduces a time dependence to any dimming event we measure. We believe this effect is negligible given that the events in the scaling regime that we are interested in have durations which are at most 3 days (fig. 3.2), much less than the 12 day half period of the Sun's rotation. Since we are most interested in seeing scaling behavior, as well as extracting the exponents τ, α, and $\sigma\nu z$, our analysis is likely not sensitive to effects related to a dimming event that might be obfuscated by the rotation of the Sun.

3.4 Several Predictions on the Spatial Properties of Sunspots

We briefly mentioned above the fractal properties of sunspots and their precursors [124, 125, 126]. We described this as a barely fractal property, as the fractal dimension of the sunspots was found to be almost 2 (i.e. the area $A \sim R^2$). This and other spatial properties of sunspots may also follow from the avalanche model in general. If we take the solar surface as a two-dimensional surface with coordinates $\mathbf{x}$, then sunspots and pores could be described as the dimming of the surface relative to average light flux $u(\mathbf{x}, t)$. To be precise, at each point $\mathbf{x}$ on the photosphere, and for time t from some starting time, the function $u(\mathbf{x}, t)$ denotes the reduction of light flux on the Sun's photosphere from the average value. As we will describe in more detail in the appendices, the cutoff S_c is closely related to the correlation length $\xi^{1/\sigma\nu} \sim S_c$. Here the correlation length is defined as the the length $\langle u(\mathbf{x}', t)u(\mathbf{x}, t)\rangle \sim C(|\mathbf{x}' - \mathbf{x}|/\xi)$, where the angular brakets represent averaging over space, and $|\cdot|$ represents the vector magnitude. The function $C(|\mathbf{x}' - \mathbf{x}|/\xi)$ decays rapidly when $|\mathbf{x}' - \mathbf{x}| > \xi$. Note that ξ diverges at the critical point, which results in the power law behavior of the correlation length at the critical point. From the form of this, we can see that the correlation length would represent a radial dimension, and the cutoff size would represent an area, so we would find that $1/\sigma\nu$ is the fractal dimension of the events.

As it turns out, the exponent $\sigma\nu z$ is the dimension we measured in our size versus duration, so this implies that the duration $T \sim \xi^z$, where z is the exponent of time. For models with long range interactions, $z = 1$, while for short range interactions $z = 2$ [6]. If we take at face value the fractal dimension of sunspots, then $\sigma\nu = 1/2$, implying that $z \sim 1.6$, in between long and short range interactions. However, if the fractal dimension of the model varies from 2 because the fractal dimensions of individual sunspots may not be the same as the fractal dimensions of collection of dimming avalanches, this is no longer true. We expect that two new telescopes, the Daniel K. Inouye Solar Telescope [129] and European Space Telescope [130] will help resolve some ambiguities, as they will collect high resolution and long-time images of the Sun.

Besides the correlation length, another quantity, known as the roughness, is also predicted to scale with distance. The term roughness comes from the theory of elastic manifolds [11], but the predictions are generic. The roughness involves the integrated intensity loss

$$U(\mathbf{x}, t) = \int_0^t u(\mathbf{x}, t')dt' \tag{3.1}$$

where 0 denotes the start of an avalanche. Then it is expected that $\langle (U(\mathbf{x}', t) - U(\mathbf{x}, t))^2 \rangle \sim |\mathbf{x}' - \mathbf{x}|^{2\zeta}$. The exponent ζ is universal [6]. For interface depinning models [11], the avalanche size exponent is conjectured to obey $\tau = 2 - \gamma/(d + \zeta)$, where we assume that for 2 dimensional events $d = 2$ [75]. The value of γ is an analogue of the range of interactions that produce the avalanches, with the exact relation being that the interaction range scales in $\mathbf{k}$-space as $|\mathbf{k}|^\gamma$. Therefore, for $\gamma = 2$, we have short range elastic interactions from laplacians, while for longer range interactions $\gamma < 2$ [6]. Therefore the roughness exponent is important to determine the long distance effective range of the interaction.

The variation of the size and duration distributions between the solar minimum and maximum is indicative of tuned criticality. All avalanche phenomena have some form of driving force, and it is thought that large convection cells beneath the photosphere drive the formation of sunspots [131]. The presence of more toroidal fields (fields pointing along the azimuthal axis) during the solar maximum as well as more turbulent motion in the convective cells could couple together to form larger sunspots that cause larger dimming events. Such a picture might offer a framework to interpret the tail of the distributions in regions 2-7, which are the solar transition and maximum. The merging of events of smaller size could cause the events to increase beyond the maximum size S_{max}, which is set by the tuning parameters of the system. A related argument shows that for systems with duration exponents $\alpha < 2$, it is possible for a driven system to have system spanning avalanches, which would also result in an exponential distribution with a large bump near the end [132] for similar reasons (i.e $S > S_{max}$). The avalanches in the bump are likely runaway events that reach larger scales than most avalanches in the system.

We have proposed that non-equilibrium critical phenomena are a natural setting to analyze how sunspots behave the Sun's photosphere. The events we have described are almost certainly generated by the Sun's magnetic field, which itself is generated by the turbulent motion of the components of the Sun [131]. In the appendices to chapter 3, we also analyze the brightening events. These show behavior similar to the dimming events, although they are almost certainly not the result of solar flares, as most flares are obfuscated by the general light from the Sun [133]. Often flares are measured by looking at entirely different wavelength regimes (such as X-ray [5]), which were unfortunately not available from VIRGO. The exponents we extracted are very close to the dimming event exponents. When compared with the exponents from solar flares, both dimming and brightening event exponents are somewhat larger than the value of the energy exponent 1.4 [5] for solar flares, with error bars not reported. Based on similar studies of solar flares in *Kepler* stars [58], we estimate the error bars of the energy exponent are are likely $\pm 0.2 - \pm 0.3$. We hope that some of the physical mechanisms that we have elucidated here can also be applied to other stars, in particular Tabby's star.

Chapter 4

Creep and Avalanches at Finite Temperature

4.1 Creep

In this chapter we give a basic introduction to the theory of creep in solids. We introduce an equation that describes creep behavior in disordered materials and study the renormalization of this equation at zero and finite temperature. In addition, we use the renormalization picture to draw conclusions about the characteristics of the disorder potential and study the mean field theory of plastic deformation and creep.

Creep in solids is the slow plastic deformation of solids under a load. The study of creep is an actively evolving field, and there are a wide variety of mechanisms that result in creep deformation of materials. Creep mechanisms are best understood for crystalline materials, where they can broadly be classified as either dislocation creep or diffusion creep [134]. Dislocation creep arises at relatively low temperature and high stresses. It is a result of the pinning of dislocations by defects in the crystalline structure [135] or through the jamming with other dislocations [136]. In fact, the point of alloying metals and work hardening is partially to help prevent dislocation gliding [137] by either introducing defects or producing dislocation jamming. Here dislocation gliding means the motion of the dislocation parallel to its slip plane (i.e. for an ideal edge dislocation, parallel to the Burger's vector). Diffusion creep in crystalline materials arises in the opposite conditions, when the temperature is relatively high and the stress is low. Here the primary mechanisms are either the diffusion of atoms into vacancies [138], diffusion along grain boundaries (for polycrystalline materials) [139], or dislocation climb (i.e. for an ideal edge dislocation, motion perpendicular to the Burger's vector) [140].

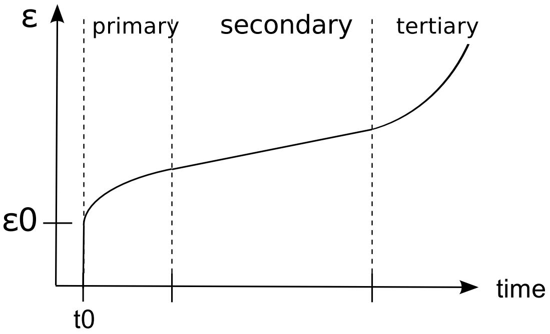

Figure 4.1: The various creep regimes that most crystalline materials exhibit, plotted as time after loading versus strain of the material. The initial jump occurs essentially instantaneously on the creep time scales because of the initial application of the stress to the system. After this, there is a period known as the primary stage of creep. During the primary stage, the strain ϵ grows as $\epsilon \propto t^{1/3}$ known as the Andrade power law. Then the secondary stage sets in, during which $\epsilon \propto t$. Finally, there is a rapid acceleration that occurs before the rupture event that destroys the material.

Despite the various mechanisms that cause crystalline creep and the variety of crystalline materials that exhibit creep, there are some very standard sets of behavior that occur in all materials shown in fig. 4.1. These are the three stages of creep that are known as the primary, secondary, and final stages [141]. Initially the material is deformed because an instantaneous load is applied to it. Then in the primary stage of creep, the material undergoes deformation along what is known as the Andrade power law regime [142]. Here the strain ϵ grows as $\epsilon \propto t^{1/3}$. Then the material enters into the secondary stage, where $\epsilon \propto t$, before finally accelerating until rupture in the final stage.

The mechanisms of creep for bulk metallic glasses (BMG) are not as well understood [42]. Here BMGs, otherwise known as amorphous metals [143], are (usually) alloys that have been cooled quickly enough to prevent formation of a crystalline structure on the atomic scale. This is in contrast to polycrystalline materials where grains of crystalline structure exist. BMGs often have to be cooled at rates of $10^5 - 10^6$ K/s [143] in order to prevent crystallization. The combination of glassiness with the properties of metallic elements allows these materials to display a remarkable array of properties, such as high tensile strength (up to 3GPa), resistance to corrosion, and the ability to be easily processed [143]. However, their amorphous nature also makes them difficult to analyze analytically, as dislocations no longer mediate plastic deformation. Instead it is thought that the deformation occurs through the activation of shear transformation zones (STZs) previously mentioned [30, 144]. At fixed stress, STZs cannot be activated unless there is either continuous flow of the glassy system, or by thermal activation [145]. We study the latter case, in which the STZ is assumed to be static until the activation event occurs.

For the remainder of this thesis, we will focus on the steady state regime of creep motion, in which the strain increases at a constant rate [42, 146]. We hypothesize that the creep of materials in the steady state regime, when the temperature is low and the stress is high, is due to many small avalanche-like jumps, rather than continuous deformation. We do not take into account diffusion, so that in our cases no diffusion creep occurs. Our primary systems of interest are crystalline materials undergoing dislocation mediated creep, and BMGs undergoing activation of shear transformation zones [147, 13, 14, 15]. Our primary contribution is to look at avalanches at finite temperature, and in particular to derive certain properties about times between such events.

4.2 The Zero Temperature Model of Plastic Deformation and Slip Avalanches

One generic but very important trait of plastic deformation of crystalline materials and BMGs is the formation of shear/glide plane. In the steady state creep regime of materials in which we are interested, the deformation localizes in slip planes, known as shear/glide planes or shear bands [30, 37, 148, 42, 149]. These are planes along which the material deforms, and we assume *a priori* that these planes have formed. This changes the character of the interaction terms that we describe. We will be more specific after introducing the continuum model.

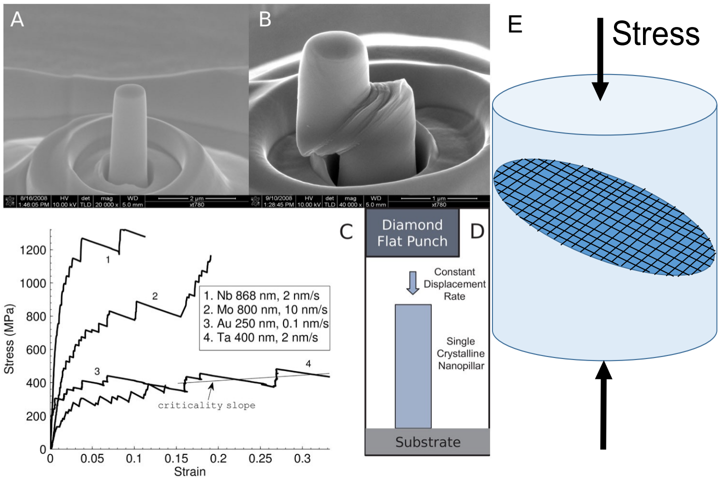

Figure 4.2: Figures (a-d) taken from [14]. (a) A standard experimental setup with a Nb nanopillar before compression. (b) The pillar after compression, which clearly shows the plastic deformation along glide planes that resulted from the stress. (c) A stress versus strain curve, which shows characteristic serrated behavior. The sudden jumps in strain are the slip avalanches. (d) A schematic of the experiment. (e) A schematic of the slip plane.

At zero temperature, the model has been known for some time [17, 13]. In the model, it is assumed that the displacement along the slip plane can be described by a function $u(\mathbf{x}, t)$ which represents the displacement of the material. For this displacement, the standard equation of motion assumes the overdamped condition, which basically means that the mass term (second order time derivative) and higher orders time derivatives are neglected. The kernel of interaction $\tilde{J}(\mathbf{x}-\mathbf{x}', t-t')$ is in general dependent on both position and history of the sample. The unique feature of the model is the addition of quenched (non-dynamical) pinning forces $f(\mathbf{x}, u(\mathbf{x}, t)$. Finally the term $\zeta(x,t)$ will describe the thermal noise, which is an idealized noise with delta function correlations (we describe it more precisely below). The equation of motion is [6, 17, 13]

$$\eta \partial_t u(\mathbf{x}, t) = \int d^2x' dt' \tilde{J}(\mathbf{x}-\mathbf{x}', t-t')(u(\mathbf{x}', t') - u(\mathbf{x}, t)) + \Sigma(\mathbf{x}, t) + f(\mathbf{x}, u(\mathbf{x}, t)) + \zeta(x, t) \tag{4.1}$$

where $\Sigma(\mathbf{x}, t)$ is the stress applied to the system, which we will often take to be uniform and time independent or varying linearly with time ($\Sigma = vt$). The term η is the friction, viscosity, or damping coefficient.

In order to specify exactly what we mean by the pinning force and the thermal noise, we need to specify the form of these functions. Since we expect these terms to be random, we specify their distributions. We make an even more narrow assumption, that these terms are both Gaussian distributed with mean zero and time independent. The noise term is correlated as typical uncorrelated noise

$$\langle \zeta(\mathbf{x},t)\zeta(\mathbf{x}',t')\rangle = 2\eta T\delta(\mathbf{x}-\mathbf{x}')\delta(t-t') \tag{4.2}$$

so that the equation of motion is a Langevin type of equation [150]. Here $\langle\cdot\rangle$ is the thermal average. This essentially states that we treat the problem at time scales much longer than atomic time scales. Finally, the pinning force is similar to the thermal noise, except

$$\overline{f(\mathbf{x},u(\mathbf{x},t))f(\mathbf{x}',u(\mathbf{x}',t'))} = \delta(\mathbf{x}-\mathbf{x}')\Delta(u-u') \tag{4.3}$$

where $u' = u(\mathbf{x}',t')$ and $\Delta(u)$ is a symmetric function, and the overbar denotes the average over different realizations of the quenched pinning forces. Note that this means there exists a non-trivial correlation of pinning force as the interface advances (i.e. the correlation along the u direction is not a delta function).

From the equation of motion, there is a simple but important consequence which can be derived immediately. We assume that $T = 0$ for this argument, and it does not apply for $T > 0$. If we have two interfaces, both experiencing the same random disorder $f(\mathbf{x},u(\mathbf{x},t))$, with $u_a(\mathbf{x},t) > u_b(\mathbf{x},t)$ at some time t for all $\mathbf{x}$ (i.e. one interface is ahead of the other), and $\tilde{J}(\mathbf{x}-\mathbf{x}',t-t')$ is a convex function, then this remains true for all times $t' > t$. This is known as Middleton's theorem [151]. It implies that if an interface is stationary at some fixed stress and disorder, then all interfaces are stationary at that fixed stress and disorder. Alternatively, if an interface is moving at some fixed stress and disorder, then all interfaces are moving at that fixed stress and disorder. What this implies is that for a fixed disorder in an infinite system, there is a unique uniform stress Σ_c at which interfaces begin moving. And what is more, because the pinning force $f(\mathbf{x},u(\mathbf{x},t))$ is random, it is expected that this critical stress is unique in an infinite system, and common among all disorder realizations, since random motion of the interface will randomly sample the pinning forces, resulting in an averaged behavior.

As it stands, the basic points are that the theory (1) has a driving force $\Sigma(\mathbf{x},t)$, (2) has quenched disorder $f(\mathbf{x},u(\mathbf{x},t))$, and (3) has a dynamical noise term $\zeta(\mathbf{x},t)$. It is practically impossible to directly solve this equation, so we often rely on various approximation methods. One of the most successful of these approximation methods is to turn this equation into a path integral, and treat it using the path integral formalism [152, 153], known as the Martin-Siggia-Rose (MSR) formalism.

4.3 Scaling Theory at Finite Temperature

Very briefly, we go over the scaling behavior of mean field theory, derived before for zero temperature [6, 17, 13] and finite temperature [154, 155] based on analogy with equilibrium critical phenomena.

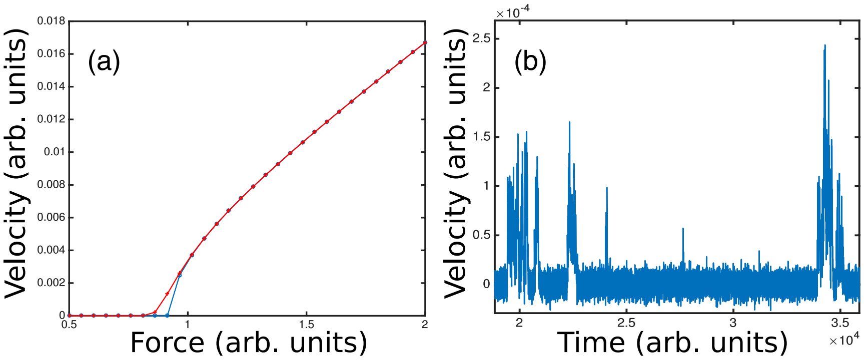

Figure 4.3: A simulation of mean field creep motion using equation 4.1 that we performed with a pinning force similar to previously used pinning forces [154]. (a) The plot of velocity versus force for two conditions, one with $T = 0$ (blue) and one with $T > 0$ (red). The $T = 0$ curve shows the sudden onset of finite velocity after the critical stress. The $T > 0$ curve shows the thermal rounding. (b) An example of the velocity as a function of time. The presence of sudden bursts can be clearly seen, along with the thermal noise that is common in finite temperature simulations.

The simulations in fig. 4.3 were done using the continuous mean field creep model (defined below), where the interaction term was replaced by a constant J, and hence models long range interactions that result in creep motion. To review, the blue curve in fig. 4.3(a) shows the onset of finite velocity of the interface after the stress exceeds the critical stress Σ_c, which here is near 0.9. Near the critical force, the velocity will scale as

$$v \sim (\Sigma - \Sigma_c)^{\beta}, \tag{4.4}$$

where in mean field theory $\beta = 1$ [6, 13]. The basic interpretation of this result is that the velocity is similar to an order parameter, while the stress is the control parameter. However, this result should not be taken too literally, as there are many differences between non-equilibrium critical phenomena and equilibrium critical phenomena. In addition, the correlation length ξ, defined above, scales as $\xi \sim |\Sigma - \Sigma_c|^{-\nu}$. The divergence at Σ_c shows the onset of an infinite avalanche where the interface acquires a finite velocity. This is encapsulated in the relation

$$S_{max} \sim (\Sigma - \Sigma_c)^{-1/\sigma} \sim \xi^{-1/\sigma\nu}. \tag{4.5}$$

Another scaling relation, long assumed but never fully derived, is that the energy barriers

$$\Delta E \sim (\Sigma_c - \Sigma)^{\gamma} \tag{4.6}$$

where γ is known as the energy exponent, which can also be interpreted as $\Delta E^{1/\gamma} \sim \Sigma_c - \Sigma$. The origin of this assumption is in Anderson's theory of flux creep [156, 157]. Several others have each found different exponents for various problems, such as for charge density waeves $\gamma = 3/2$ [155], the short range interface depinning $\gamma = 1$ [158], or the long range plasticity model $\gamma = 2$ [154]. Although not visible for small stresses in fig. 4.3(a), the $T > 0$ curve has $v > 0$ for all stresses $\Sigma > 0$. This is due to thermal activation, as seen in fig. 4.3(b). Given the assumption eq. 4.6, temperature fluctuations needed to activate a site would be on the order of ΔE, so that in order to activate sites with barriers ΔE, $k_B T \geq \Delta E$. The temperature T causes deviations from the critical point at $T = 0$. However, near the critical point T causes deviations which can be predicted using the theory of critical phenomena [155, 154]. On average, the activated energy barriers are those of order $k_B T$, as (on average) the temperature cannot overcome energy barriers with $\Delta E > k_B T$, so we will have that the temperature can overcome barriers of average size size $\Delta E \sim k_B T$. This average energy barrier means that the average velocity $v \sim (\Sigma_c - \Sigma)^{\beta} \sim \Delta E^{\beta/\gamma}$ so that

$$v \sim (k_B T)^{\beta/\gamma}, \tag{4.7}$$

where k_B is the Boltzmann constant and T is the temperature. This finite velocity is known as the thermal rounding, and is a common feature of creep motion. We hypothesize that the thermal rounding, at least when $\Sigma < \Sigma_c$, is due to thermal activation such as that seen in fig. 4.3(b). As another example, since we know that $\xi \sim (\Sigma_c - \Sigma)^{-\nu}$ then $\xi \sim \Delta E^{-\nu/\gamma}$ or $\xi \sim (k_B T)^{-\nu/\gamma}$. This results in a maximum avalanche size of (at $\Sigma_c = \Sigma$)

$$S_{max} \sim (k_B T)^{-\frac{1}{\gamma\sigma}} \tag{4.8}$$

where we used eq. 4.5. The result indicates that near criticality, the avalanche sizes actually shrink with temperature. The physical explanation of this is that the thermal noise smooths the avalanches, so that instead of huge excursions around the average velocity v, the avalanches are small excursions around this velocity. Our primary interests are in looking at quantities not accessible based on scaling theory, in particular the distribution of times between such thermal activation events. The interevent time distribution is difficult to derive from scaling theory, but easily accessed experimentally.

4.4 Overview of Renormalization at Finite Temperature

4.4.1 Outline of the Renormalization Procedure

In order to further develop the theory, we need to solve eq. 4.1 and find the probability density $\mathcal{P}(u, f, \zeta)$, which is a probability density over the space of functions $u(\mathbf{x}, t)$ as well as f and ζ. An equivalent and often easy method of deriving the probability density is to find the generating functional Z [159]. For simplicity, let us write the equation of motion as $\partial_t u - F(u, \tilde{J}, f, \Sigma, \zeta) = 0$, where F is the somewhat complicated right side of eq. 4.1, and we have absorbed η into the other constants. One can write the generating functional as

$$\langle\overline{Z[w]}\rangle = \langle\overline{e^{i\int wu}}\rangle \tag{4.9}$$

where w is an auxiliary variable, and again $\langle\cdot\rangle$ and $\bar{\cdot}$ represent the thermal and disorder averages respectively. Note that we are being schematic so we have not written down the various function arguments for u and w, as these can be inferred easily. Then we can find all correlation functions by simply differentiating $\langle\overline{Z}\rangle$ with respect to w. We impose a delta functional constraint, which basically says that the function u must obey the equations of motion

$$Z = \int \mathcal{D}u\delta\left(\partial_t u(\mathbf{x}, t) - F(u, \tilde{J}, f, \Sigma, \zeta)\right)\mathcal{J}(u, \partial_t u, \tilde{J}, f, \Sigma)e^{i\int wu}. \tag{4.10}$$

Here $\mathcal{D}u$ is the measure over function space and $\mathcal{J}$ is the Jacobian determinant, which is necessary because $\langle\overline{Z[w=0]}\rangle = 1$ [159] is required if the probability density is to be normalized to 1. Now we want to take advantage of the Fourier identity

$$\delta(x) = \int \frac{dk}{2\pi}e^{ikx} \tag{4.11}$$

but in a functional space with $u(\mathbf{x}, t)$ being the x and another field $\hat{u}(\mathbf{x}, t)$ being k [159]. This will allow us to write the partition function

$$\begin{aligned} Z = \int \mathcal{D}u\mathcal{D}\hat{u}\exp\left(i\int d^2xdt\hat{u}(\mathbf{x}, t)\left(\partial_t u(\mathbf{x}, t) - F(u, \tilde{J}, f, \Sigma, \zeta)\right)\right)\mathcal{J}(u, \partial_t u, \tilde{J}, f, \Sigma)e^{i\int wu} = \\ \int \mathcal{D}u\mathcal{D}\hat{u}\exp\left(iS_{eq}(\hat{u}(\mathbf{x}, t), u(\mathbf{x}, t)) + i\int u(\mathbf{x}, t)w(\mathbf{x}, t)\right)\mathcal{J}(u, \partial_t u, \tilde{J}, f, \Sigma) \end{aligned} \tag{4.12}$$

where $S_{eq} = \int d^2xdt\hat{u}(\mathbf{x}, t)\left(\partial_t u(\mathbf{x}, t) - F(u, \tilde{J}, f, \Sigma, \zeta)\right)$. Note that this generating function is in analogy to but distinct from the equilibrium statistical mechanics partition function, as it contains forces and time derivatives instead of simply energy. It also contains an auxiliary field $\hat{u}(\mathbf{x}, t)$. This auxiliary field is a necessity in order to analyze the classical stoachastic system with the path integral [152]. We will ultimately be averaging over disorder and variations in temperature to find the mean behavior. Recall that $\langle\cdot\rangle$ is averaging over temperature and $\bar{\cdot}$ is averaging over disorder in this chapter, so the mean behavior of $u(\mathbf{x},t) = \frac{\delta\langle\overline{Z[w]}\rangle}{\delta iw}\big|_{w=0}$ is

$$\langle\overline{u(\mathbf{x},t)}\rangle = \left\langle\overline{\int \mathcal{D}u\mathcal{D}\hat{u}u(\mathbf{x},t)\exp\left(iS_{eq}\right)\mathcal{J}(u,\partial_t u,\tilde{J},f,\Sigma)}\right\rangle. \tag{4.13}$$

Next we want to find the response function $R(\mathbf{x},\mathbf{x}',t,t')$, which is the response of $u(\mathbf{x},t)$ to a small perturbation at time $\mathbf{x}',t'$ which we write as $\delta\Sigma\delta(\mathbf{x}'-x)\delta(t'-t) = \delta\Sigma(\mathbf{x}',t')$. Adding this response function to S_{eq}, we get $S_{eq} - \delta\Sigma(\mathbf{x}',t') = \partial_t u(\mathbf{x},t) - F(u,\tilde{J},f,\Sigma,\zeta) - \delta\Sigma(\mathbf{x}',t')$. Since $\delta\Sigma$ is considered small, we expand the exponential term

$$\exp\left(-i\int d^2x dt\hat{u}(\mathbf{x},t)\delta\Sigma(\mathbf{x}',t')\right) \approx 1 - i\int d^x dt\hat{u}(\mathbf{x},t)\delta\Sigma(\mathbf{x}',t') = 1 - i\hat{u}(\mathbf{x}',t')\delta\Sigma \tag{4.14}$$

neglecting higher order terms. Here we integrated out the δ functions in the definition of $\delta\Sigma(x',t')$. Calling the perturbed field $u'(\mathbf{x},t)$, this results in

$$\langle\overline{u'(\mathbf{x},t)}\rangle = \left\langle\overline{\int \mathcal{D}u\mathcal{D}\hat{u}u(\mathbf{x},t)\exp\left(iS_{eq} + \int i\hat{u}(\mathbf{x},t)\delta\Sigma(\mathbf{x}',t')\right)\mathcal{J}}\right\rangle \tag{4.15}$$

$$\langle\overline{u'(\mathbf{x},t)}\rangle = \langle\overline{u(\mathbf{x},t)}\rangle - \left\langle\overline{\int \mathcal{D}u\mathcal{D}\hat{u}u(\mathbf{x},t)i\hat{u}(\mathbf{x}',t')\delta\Sigma\exp\left(iS_{eq}\right)\mathcal{J}}\right\rangle \tag{4.16}$$

$$\langle\delta\overline{u(\mathbf{x},t)}\rangle = -\left\langle\overline{\int \mathcal{D}u\mathcal{D}\hat{u}u(\mathbf{x},t)i\hat{u}(\mathbf{x}',t')\delta\Sigma\exp\left(iS_{eq}\right)\mathcal{J}}\right\rangle \tag{4.17}$$

where the $\delta\Sigma$ can be pulled out since it is not integrated. Then the response function

$$R(\mathbf{x},\mathbf{x}',t,t') = \frac{\langle\overline{\delta u(\mathbf{x},t)}\rangle}{\delta\Sigma} = -\langle\overline{u(\mathbf{x},t)i\hat{u}(\mathbf{x}',t')}\rangle \tag{4.18}$$

which means that $\hat{u}(\mathbf{x}',t')$ can be interpreted as field that, when coupled with $u(\mathbf{x},t)$ gives the response function. And this response function plays a role analogous to the propagator in field theory [152, 10, 11, 22].

Now we want to consider averaged quantities $\langle\overline{Z[w]}\rangle$ averaged over both temperature and disorder. Just like in spin glass theory [53], averaging over disorder f is a complicated business often involving replicas [53] or supersymmetry [160]. The approach we take has been known for some time [159, 153, 161]. As we show in the appendix to this chapter, we will need the equal time response function $R(\mathbf{x},\mathbf{x}',t,t)$ in order to perform renormalization calculations. In the Itô convention from stochastic calculus, this response function $R(\mathbf{x},\mathbf{x}',t,t) = 0$ [153, 10]. It turns out this also vastly simplifies the Jacobian determinant

$\mathcal{J}(u, \partial_t u, \tilde{J}, f, \Sigma) = 1$ [10, 11, 22, 161]. Since the determinant $\mathcal{J} = 1$, we can directly average the arguments of the generating functional without invoking replicas or supersymmetry. The two terms which we have to average are the terms in an exponential eq. 4.12, of the form $\exp\left(-i \int \hat{u}(\mathbf{x}, t) f(\mathbf{x}, t, u(\mathbf{x}, t)\right)$ and $\exp\left(-i \int \hat{u}(\mathbf{x}, t)\zeta(\mathbf{x}, t)\right)$. To average over disorder, we must expand the exponential, remembering that when averaging over odd powers of f, we get zero because the mean of f is zero. We neglect the arguments of the functions since they are inessential, and do not write the parts that are not averaged over to simplify notation so that

$$\overline{e^{-i\int \hat{u}f}} = \sum_{k=0}^{\infty} \overline{\frac{(-i\int \hat{u}f)^k}{k!}} = \sum_{k=0}^{\infty} \overline{\frac{(-i\int \hat{u}f)^{2k}}{(2k)!}} \tag{4.19}$$

$$\overline{e^{-i\int \hat{u}f}} = \sum_{k=0}^{\infty} \frac{\overline{(-i\int \hat{u}f)^k(-i\int \hat{u}f)^k}}{(2k)!} = \sum_{k=0}^{\infty} \frac{(-\int \hat{u}\hat{u}')^k \overline{ff'^k}}{(2k)!} \tag{4.20}$$

$$\overline{e^{-i\int \hat{u}f}} = \sum_{k=0}^{\infty} \frac{(2k-1)!!(-\int \hat{u}\Delta(u-u')\hat{u}')^k}{(2k)!} = \sum_{k=0}^{\infty} \frac{(-\int \hat{u}\Delta(u-u')\hat{u}')^k}{2^k(k)!} \tag{4.21}$$

$$\overline{e^{-i\int \hat{u}f}} = e^{\frac{1}{2}\int i\hat{u}i\hat{u}'\Delta(u-u')}. \tag{4.22}$$

Here $\hat{u} = \hat{u}(\mathbf{x}, t)$, $\hat{u}' = \hat{u}'(\mathbf{x}, t')$, $u = u(\mathbf{x}, t)$, $u' = u(\mathbf{x}, t')$, $f = f(u(\mathbf{x}, t), \mathbf{x})$, $f' = f(u(\mathbf{x}, t'), \mathbf{x})$, $(2k-1)!! = (2k-1)(2k-3)\cdots 1$ is the double factorial that arises because of Wick contractions of powers of f, and we have used the result of the variance eq. 4.3. Eq. 4.22 is standard and can be seen in almost all approaches to the field theory of equation 4.1 [6, 10, 11, 85]. The temperature average follows exactly the same steps, except there is a factor of 2 because of the definition eq. 4.2. The result for temperature is therefore

$$\langle e^{-i\int d^2x dt \hat{u}\zeta} \rangle = e^{\eta T \int d^2x dt i\hat{u}i\hat{u}} \tag{4.23}$$

where we plugged in the variance $\langle \zeta\zeta' \rangle = 2\eta T \delta(\mathbf{x}-\mathbf{x}')\delta(t-t')$ and integrated out the delta functions. Given this, let us reintroduce the variables from eq. 4.1 to rewrite $S_e q$ so that

$$\begin{aligned}\langle \overline{Z[w]} \rangle = \int \mathcal{D}u\mathcal{D}\hat{u} \exp \int d^2x dt i\hat{u}(\mathbf{x}, t) \left(\eta \partial_t u(\mathbf{x}, t) - \int d^2x' dt' \tilde{J}(\mathbf{x}-\mathbf{x}', t-t')(u(\mathbf{x}', t') - u(\mathbf{x}, t)) - \Sigma(\mathbf{x}, t) \right) \times \\ \overline{\exp\left(-i \int d^2x dt \hat{u}(\mathbf{x}, t) f(u(\mathbf{x}, t), \mathbf{x})\right)} \left\langle \exp\left(-i \int d^2x dt \hat{u}(\mathbf{x}, t)\zeta(\mathbf{x}, t)\right) \right\rangle \exp\left(i \int d^2x dt w(\mathbf{x}, t) u(\mathbf{x}, t)\right).\end{aligned} \tag{4.24}$$

Plugging in eq. 4.22 and eq. 4.23 we get

$$\begin{aligned}
&\langle\overline{Z[w]}\rangle = \\
&\quad\int \mathcal{D}u\mathcal{D}\hat{u}\exp\int d^2xdti\hat{u}(\mathbf{x},t)\left(\eta\partial_t u(\mathbf{x},t) - \int d^2x'\tilde{J}(\mathbf{x}-\mathbf{x}',t-t')(u(\mathbf{x}',t')-u(\mathbf{x},t)) - \Sigma(\mathbf{x},t)\right)\times \\
&\qquad\qquad \exp\left(-\frac{1}{2}\int d^2xdtd^2x'\hat{u}(\mathbf{x},t)\Delta(u(\mathbf{x},t)-u(\mathbf{x}',t))\hat{u}(\mathbf{x}',t)\right)\times \\
&\qquad\qquad\qquad \exp\left(-\eta T\int d^2xdt\hat{u}(\mathbf{x},t)\hat{u}(\mathbf{x},t)\right)\exp\left(i\int d^2xdtw(\mathbf{x},t)u(\mathbf{x},t)\right)
\end{aligned} \tag{4.25}$$

From this we can read off the action

$$\begin{aligned}
S = &\int d^2xdti\hat{u}(\mathbf{x},t)\left(\eta\partial_t u(\mathbf{x},t) - \int d^2x'\tilde{J}(\mathbf{x}-\mathbf{x}',t-t')(u(\mathbf{x}',t')-u(\mathbf{x},t)) - \Sigma(\mathbf{x},t)\right) \\
&- \frac{1}{2}\int d^2xdtdt'i\hat{u}(\mathbf{x},t)i\hat{u}(\mathbf{x},t')\Delta(u-u') - \eta T\int d^2xdti\hat{u}(\mathbf{x},t)i\hat{u}(\mathbf{x},t)
\end{aligned} \tag{4.26}$$

where the action is defined as $\langle\overline{Z[w]}\rangle = \int \mathcal{D}u\mathcal{D}\hat{u}e^{S}e^{i\int wu}$. Note that sometimes one sees the form with a factor of i factored out. We keep the i in the action because the combination $i\hat{u}$ is what appears in each of the integrals. Also it is sometimes useful to consider the generating functional $\langle\overline{Z[w,v]}\rangle = \int \mathcal{D}u\mathcal{D}\hat{u}e^{S}e^{i\int wu+i\int v\hat{u}}$ [10]. The resulting action does not change compared to eq. 4.26.

At this point we make some simplifications. As mentioned in the introduction, the interactions between slips of dislocations and STZs scales as $\tilde{J}(\mathbf{x}-\mathbf{x}') \sim J/|\mathbf{x}-\mathbf{x}'|^3$, with no time dependence, where the J denotes the strength scale of the interactions. The simplification of all positive interactions and the decay of the interactions [6, 13] is justified because we are concerned with creep during the steady state regime, after glide planes have formed (see fig. 4.2 for the zero temperature case). Once these planes are formed the leading term in the interaction kernels is a long range positive factor which scales as $1/|\mathbf{x}|^3$. We also assume Σ is uniform and has no time dependence either, as this is the case we are most interested in (i.e. creep due to static stress).

The strategy to approach critical phenomena in field theory is to use renormalization [19, 20]. In order to renormalize, we set a microscopic scale r_0, and coarse grain and rescale our coordinates as we increase our scale as

$$r_\ell = e^{\ell}r_0. \tag{4.27}$$

Here ℓ controls the scale at which we consider the action eq. 4.26 after renormalization, so for larger ℓ, the action will be renormalized to a coarser scale. For an infinitesimal increase $\delta\ell$ we then have $r_{\ell+\delta\ell} = (1+\delta\ell)r_\ell$. It is often convenient to consider the equations in momentum space, for which $\Lambda = 1/r_0$, and $\Lambda_\ell = \Lambda e^{-\ell}$.

Then the ultimate goal of the renormalization group (RG) procedure is to find out how the action eq. 4.26 changes as a function of the dimensionless scale ℓ. It turns out that each variable in the action rescales with ℓ. Easiest to understand are the position variables $d^2x \to e^{2\ell}d^2x$. All other exponents change based on this rescaling [10, 11, 22, 1] .

To successfully renormalize the theory, we also need to define the upper critical dimension, which for our case is $d_c = 2$ as described before, and consider the case where our dimension is arbitrary $d \leq d_c$. Here, the coupling includes the highly non-linear function $\Delta(u-u')$ in eq. 4.26, as this is the only integral that involves more than 2 powers of $u(\mathbf{x}, t)$ and $\hat{u}(\mathbf{x}, t)$. In fact, it will be an unfortunate but necessary for renormalization we will have to consider $\Delta(u - u')$ as a coupling function, and renormalize this entire function [10]. To do this, we Taylor expand the function $\Delta(u - u')$ to arbitrary powers $(u - u')^k$, renormalize each power as a vertex, and then resum the results to obtain the full renormalization of $\Delta(u - u')$.

At this point we will not go into the details of the renormalization procedure [10, 162, 11, 163] which have been known at finite temperature for short range potentials [85]. A derivation for long range interactions is available in the appendices to chapter 4. Let us define all the relevant variables. As above, let J denote the strength of the interactions so that $\tilde{J}(\mathbf{x} - \mathbf{x}') = J/|\mathbf{x} - \mathbf{x}'|^3$ in eq. 4.26. It turns out that the the coupling J is not renormalized due to a symmetry of the equations of motion (known as statistical tilt symmetry [10]). In order to renormalize at finite temperature, we need to introduce a finite velocity v for the interface. It is convenient to renormalize the product ηv, since this combination appears in the action eq. 4.26 after we switch the a moving frame. Explicitly, if we go to the moving frame $u(\mathbf{x}, t) \to u(\mathbf{x}, t) + vt$, then $\eta \partial_t u(\mathbf{x}, t) \to \eta \partial_t u(\mathbf{x}, t) + \eta v$. We have to rescale some of the variables in the action eq. 4.26 to simplify the equations later, so we define

$$\tilde{T} = \frac{T\Lambda^d S_d}{J\Lambda} \tag{4.28}$$

$$\kappa = \frac{\eta v}{J\Lambda} \tag{4.29}$$

$$\tilde{\Sigma} = \Sigma - \eta v \tag{4.30}$$

$$\tilde{\Delta}(u) = \frac{\Lambda^d S_d \Delta(u)}{(J\Lambda)^2} \tag{4.31}$$

to simplify the renormalization equations below, where $\Lambda = 1/r_0$ is the momentum scale defined above, S_d is the surface area of the unit $d-1$-dimensional sphere (i.e. $S_2 = 2\pi$). In our case, we have defined $d = 2$, but we write for generic d since this is required by renormalization.

4.4.2 Results Derivable from Renormalization

As we infinitesimally change the scale factor ℓ the equations for renormalization are (see appendix for chapter 4) [10, 11, 85, 1, 13]

$$\begin{aligned}
\partial_\ell \ln \tilde{T} &= -\theta + 2\kappa \int_0^\infty dt t e^{-t} \tilde{\Delta}'''(\kappa t) && (4.32)\\
\partial_\ell \ln \kappa &= (1-\zeta) - \int_0^\infty dt t e^{-t} \tilde{\Delta}''(\kappa t) && (4.33)\\
\partial_\ell \tilde{\Sigma} &= (1-\zeta)\tilde{\Sigma} + J\Lambda \int_0^\infty dt e^{-t} \tilde{\Delta}'(\kappa t) && (4.34)\\
\partial_\ell \tilde{\Delta}(u) &= (\epsilon - 2\zeta)\tilde{\Delta}(u) + \zeta u \tilde{\Delta}(u) + \tilde{T}\tilde{\Delta}''(u) + \int_0^\infty \int_0^\infty dt dt' e^{-t-t'} \tilde{\Delta}''(u)[\tilde{\Delta}((t'-t)\kappa) - \tilde{\Delta}(u + (t'-t)\kappa)]\\
&\quad - \tilde{\Delta}'(u - t'\kappa)\tilde{\Delta}'(u + t\kappa) + \tilde{\Delta}'((t+t')\kappa)[\tilde{\Delta}'(u - t'\kappa) - \tilde{\Delta}'(u + t\kappa)]. && (4.35)
\end{aligned}$$

Here ζ is the roughness, $\zeta = \epsilon/3$ where $\epsilon = 2 - d$, $\theta = 2\zeta + 1 - \epsilon$, and $\partial_\ell = \frac{\partial}{\partial \ell}$. To remind the reader of the various quantities, $\tilde{T}$, κ, $\tilde{\Sigma}$, and $\tilde{\Delta}$ are defined above in eqs. 4.28-4.31. J and Λ are the strength of the interactions and the inverse of the short distance cutoff $1/r_0$, defined above. In the equations, we need to integrate over the function $\tilde{\Delta}(u)$, and the variables of integration are labeled t and t' in eqs. 4.32-4.35. We have assumed that each of the variables is implicitly a function of the scale ℓ, which we have no written explicitly to reduce the number of arguments and simplify writing the equations. The equations are the result of the unfortunate fact that one of the coupling terms in the action eq. 4.26 is $\Delta(u - u')$, which is a function. And as it turns out, the Taylor expansion of this function is marginal in $d = 2$ for all terms in the expansion [163], thus leaving us to renormalize a function (hence why the renormalization procedure is sometimes called functional renormalization [10, 11], although this term is used in other contexts as well [164]).

The variables $\tilde{T}$ and $\tilde{\Sigma}$ are rescaled temperature and stress appearing in the action, defined by eq. 4.28 and eq. 4.30. $\tilde{\Delta}$ is a rescaled version of the disorder correlator defined by eq. 4.31, and its flow is the primary quantity that controls how the system behaves. The variable κ defined in eq. 4.29 can be thought of as generated by the finite velocity v for $T > 0$, and is translated into a position variable because there is a time scale $t = c/r_\ell \eta = c\Lambda/\eta$. The first 3 terms on the right hand size of eq. 4.35 are first order corrections to the disorder correlator. The large integral term on the right hand size of eq. 4.35 is responsible for the difficulty of analytically analyzing eq. 4.35 at finite velocity (i.e. finite κ). One thing to note is that in $d = 2$, $\zeta = 0$ and $\epsilon = 0$, so that $\theta = 1$. This means that the temperature is formally irrelevant, unlike the other three terms. Of course, this temperature is actually dangerously irrelevant, as it can easily be seen that as long as $\Delta''' > 0$ and $\kappa > 0$ in eq. 4.32 the temperature will eventually grow, because the term κ will grow (it is formally relevant).

We will only approach these equations approximately in a sense made precise below. Unfortunately equation 4.35 is prone to pathological behavior at the origin (i.e. when $u = u'$ as we will see) and therefore very difficult to analyze numerically [85]. A small simplification is that we will look at only $d = 2$, so that many of the constants can be set to zero. A much larger simplification is that we look at only near the critical point, at which $v \approx 0$ and $T \approx 0$, with $1 - \Sigma/\Sigma_c \ll 1$. This model has been analyzed at the upper critical dimension before for short range forces $d_c = 4$ at zero temperature [165], and the analysis here is similar, except we adapt it to long range forces at finite temperature.

At the upper critical dimension for long range interactions with $d = d_c = 2$, near zero velocity, we can take $\kappa \to 0$. This means that the terms in $\tilde{\Delta}(x + \kappa(t - t')) \approx \tilde{\Delta}(x) + \mathcal{O}(\kappa)$ and $\tilde{\Delta}'(x \pm \kappa t) \approx \tilde{\Delta}'(x) + \mathcal{O}(\kappa)$, where x is either 0 or u depending on the argument in eq. 4.35. Then the integrals can be carried out exactly so that eq. 4.35 becomes

$$\partial_\ell \tilde{\Delta}(u) = \tilde{\Delta}''(u)(\tilde{T} + \tilde{\Delta}(0) - \tilde{\Delta}(u)) - \tilde{\Delta}'(u)^2 \tag{4.36}$$

which is a much simpler equation. First, setting $\tilde{T} = 0$, we can take two derivatives with respect to u, giving

$$\partial_\ell \tilde{\Delta}'(u) = \tilde{\Delta}'''\tilde{\Delta}(0) - 3\tilde{\Delta}''(u)\tilde{\Delta}'(u) - \tilde{\Delta}'''(u)\tilde{\Delta}(u) \tag{4.37}$$

$$\partial_\ell \tilde{\Delta}''(u) = \tilde{\Delta}^{(4)}\tilde{\Delta}(0) - 4\tilde{\Delta}'''(u)\tilde{\Delta}'(u) - \tilde{\Delta}^{(4)}(u)\tilde{\Delta}(u) - 3\tilde{\Delta}''(u)^2 \tag{4.38}$$

$$\partial_\ell \tilde{\Delta}''(0) = -3\tilde{\Delta}''(0)^2 \tag{4.39}$$

where in the last line we have that $\Delta'''(0) = 0$ by symmetry. Since eq. 4.39 has no other derivatives of $\tilde{\Delta}$, we can solve it using separation of variables

$$\frac{\partial \tilde{\Delta}''(0)}{\partial \ell} = -3\tilde{\Delta}''(0)^2 \tag{4.40}$$

$$\int \frac{d\tilde{\Delta}''(0)}{\tilde{\Delta}''(0)^2} = -3 \int d\ell \tag{4.41}$$

$$-\frac{1}{\tilde{\Delta}''(0)} = -3\ell + c \tag{4.42}$$

$$\tilde{\Delta}''(0) = \frac{1}{3\ell - c} \tag{4.43}$$

with $c = -1/\tilde{\Delta}_0''(0)$ by plugging in $\ell = 0$. This results in

$$\tilde{\Delta}''(0) = 1/(3\ell + 1/\tilde{\Delta}_0''(0)) \tag{4.44}$$

that diverges when

$$\ell = \ell_c = -\frac{1}{3\tilde{\Delta}_0''(0)}, \tag{4.45}$$

where $\tilde{\Delta}_0$ is the initial disorder correlator before renormalization. Note that $\tilde{\Delta}_0''(0) < 0$ is necessary because $\tilde{\Delta}_0(0)$ is a correlation function, which must be maximum when the two disorder realizations are equal (i.e. when there is no relative shift in correlating the disorders, so that $u = 0$). The physical length is obtained by plugging in ℓ_c into eq. 4.27,

$$L_c = r_0 e^{\ell_c} = \Lambda^{-1} e^{\ell_c} \tag{4.46}$$

which is known as the Larkin length [79], and is the scale at which the disorder starts to dominate the interaction forces. In the context of long range forces, this means that below the length scale $L < L_c$, the disorder is weaker than the interactions and can be neglected when solving the equations of motion eq. 4.1, while above the length scale $L > L_c$, the disorder becomes relevant to solving the equations of motion eq. 4.1.

Luckily, a simple solution exists for eq. 4.36. We take $\tilde{\Delta}(u) = \phi(\ell)\rho(\psi(\ell)z)$, where ϕ and ψ are functions only of the scale parameter ℓ [165]. The reason we do this is that we wish to find a solution $\tilde{\Delta}(u)$ which is invariant to changes in scale ℓ, except for possible rescaling of the coordinates ($\psi(\ell)$), or as a factor of the entire function ($\phi(\ell)$). Here $u = \psi(\ell)z$, and z is a variable independent of ℓ. Here one can consider ρ to describe the shape of the disorder, ϕ to describe the scale of the disorder, and ψ to describe the range of the disorder (i.e. $\rho \to 0$ for $z \gg \psi(\ell)$). Then plugging this into eq. 4.36, for which we detail the calculations in the appendix to chapter 4, we get that

$$\phi(\ell) = (3a^2\ell)^{-1/3},\ \psi(\ell) = (3\ell/a)^{-1/3},\ a \approx \frac{1.55J^2}{2\pi c} \tag{4.47}$$

$$\frac{d}{dz}(z\rho(z)) = \frac{d^2}{dz^2}(\rho^2(z)/2 - \rho(z)\rho(0) - \hat{T}\rho(z)) \tag{4.48}$$

where $\hat{T} = \tilde{T}/\phi$ and $c = \int_{-\infty}^{\infty} du \tilde{\Delta}_0(u)$ (i.e. the total integral of the initial function before RG). The terms ϕ and ψ determine the overall scale of $\tilde{\Delta}$ and the width of $\tilde{\Delta}$ respectively. Solving eq. 4.48 (again detailed in appendix to chapter 4) we get that

$$\rho(z) - 1 - (1 + \hat{T})\ln(\rho(z)) = \frac{z^2}{2} \tag{4.49}$$

$$\tilde{\Delta}^*(u) = (3a^2\ell)^{-1/3}\rho(u/(3\ell/a)^{1/3}) \tag{4.50}$$

where eq. 4.49 and eq. 4.50 is similar to the equation derived for the upper critical dimension for short range potentials [165], except for the addition of the term $\hat{T}\ln(\rho(z))$ that occurs in eq. 4.49. This implicit equation cannot be solved, but when plotted there are two important regimes, namely $\hat{T}=0$ and $\hat{T}>0$.

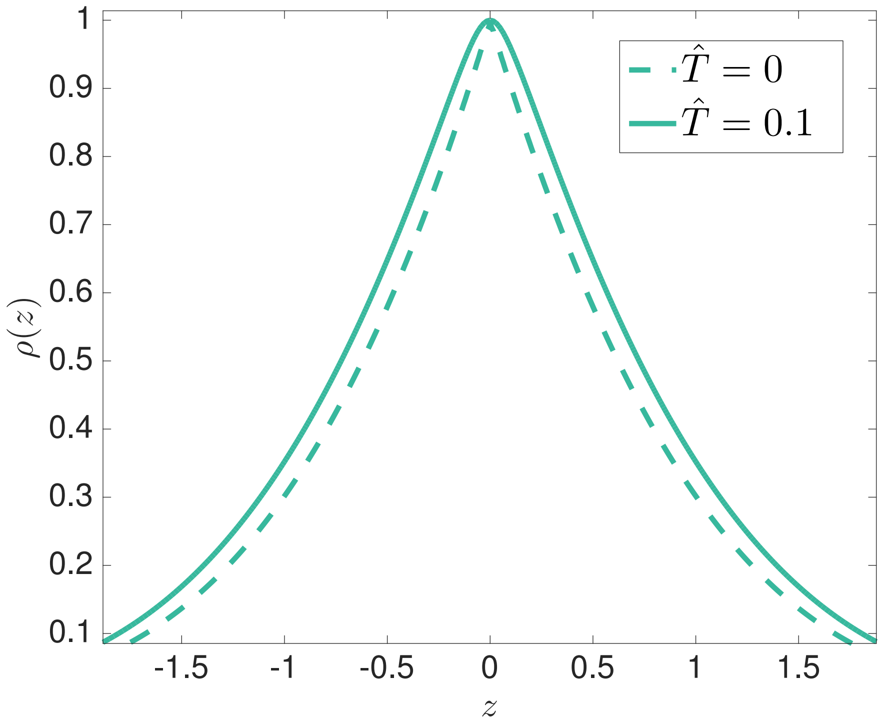

Figure 4.4: A plot of the implicit function eq. 4.49 for $\hat{T}=0$ and $\hat{T}=0.1$. The most important point is to note the cusp at $\hat{T}=0$ and the rounding $\hat{T}>0$ [85], which is important for analyzing the behavior of the system, as the cusp at $\hat{T}=0$ is non-analytic, and can only be expanded as $\rho(z,\hat{T}=0)\approx 1-|z|+\frac{1}{3}z^2+\mathcal{O}(|z|^3)$ [165].

We plot eq. 4.49 in fig. 4.4 for the two cases $\hat{T}=0$ and $\hat{T}=0.1$. Many of the conclusions derived (which we summarize below) from renormalization that hold at $d<d_c=2$ hold for $d=d_c$ [85, 158]. In fig. 4.4, we see that the function $\rho(z)$ decays past about $|z|=1$, so considering the full disorder correlator $\tilde{\Delta}^*(u)=\phi(\ell)\rho(\psi(\ell)z)$ as a function of z, means that $\tilde{\Delta}^*(u)$ has scale $1/\psi(\ell)$. To remind the reader, z is the scale independent coordinate of the scale indepedent part of the disorder correlator $\rho(z)$. To be precise, we define the scale of $\rho(u)$ as arguments $u>1$. Since the argument of ρ is $u=\psi(\ell)z=1$, we have that the scale of the disorder correlator is $1/\psi(\ell)$. At $\hat{T}>0$, what happens is that the temperature regulates the divergence seen in eq. 4.39 as $\tilde{\Delta}^{*\prime\prime}(0)\sim 1/\hat{T}$. This can be seen by implicitly differentiating eq. 4.48 twice with respect to z, and then setting $z=0$. This results in

$$\rho''-(1+\hat{T})\frac{\rho''}{\rho}+(1+\hat{T})\frac{\rho'^2}{\rho^2}=1. \tag{4.51}$$

For $\hat{T} > 0$, one has that $\rho(0) = 1$, $\rho'(0) = 0$, so $\rho''(0)\hat{T} = 1$, or $\rho''(0) = 1/\hat{T}$.

Since the correlator is rounded at $\hat{T} > 0$, this suggests that for any $\hat{T} > 0$, there is a finite velocity $v > 0$ for any stress $\Sigma > 0$, and therefore $\kappa > 0$ is possible in eqs. 4.32-4.35. If $\kappa > 0$, then the precise study of creep through these equations is difficult because the equations eqs. 4.32-4.35 are now nonlinear partial integro-differential equations, for which there are no general analytical methods of solution. Although one can derive velocity-force characteristics from eqs. 4.32-4.35 [85] when the stress $\Sigma \ll \Sigma_c$, or when the stress $\Sigma \to \Sigma_c$, it is difficult to derive distributions of waiting times, which can be derived at $\hat{T} = 0$ for a system at a slowly increasing force [75] $\Sigma(t) = \lambda t$. The primary hypothesis we make about creep in materials is that at low temperatures it is the result of many discrete activation events which we call slip avalanches that result in a finite average velocity $v > 0$. At zero temperature in mean field theory, these slip avalanches have been well understood [6, 13]. At finite temperature this is no longer true, and the concept of slip avalanches is still unresolved. Simulations such as those plotted in fig. 4.3(b) suggest that the idea of slip avalanches extends well to finite temperature, as long as the temperature is low.

A variety of exponents can be derived for the upper critical dimension using the ϵ expansion and then setting $\epsilon = 0$. For $\hat{T} = 0$, this has been done for long range forces [163], resulting in $\beta = 1 - 2\epsilon/9$, where β was exponent relating velocity to force in eq. 4.4, $\nu = 1/(1-\epsilon/3), 1/\sigma = (1-\epsilon/3)(d+\epsilon/3)$ for the avalanche cutoff S_{max} in eq. 4.5 with $\epsilon = 2 - d$. The expansions of ν and $1/\sigma$ are not to $\mathcal{O}(\epsilon)$, but instead believed to be exact relations [163]. These exponents do not depend on details of the system, instead depending only on the dimension and the form but not the constants of eq. 4.1. Therefore they are expected to be universal. At the upper critical dimension $\beta = 1$, $\nu = 1$, and $1/\sigma = 2$ if we neglect logarithmic corrections. However, many different estimates of γ, the energy exponent in eq. 4.6 exist, with simple estimates setting $\gamma = 2$ [154] while RG suggests (but it has not been rigorously shown) that $\gamma = 1$ for short range forces [158]. We show in the appendices that the RG analysis for γ extends to long range forces as well. With doubts as to what the exponent γ is at the upper critical dimension, we turn to a simpler theory to help us solve some of the problems presented here, known as the mean field theory of plasticity [13].

4.5 Mean Field Theory of Creep

In order to better understand the theory of creep, we reduce all the interactions to mean field interactions. In this case, mean field theory (MFT) applies for $d = d_c$ as long as we neglect the logarithmic corrections. This often yields simpler equations that can be analytically tractable or simulated much more quickly [17, 13]. First, to reduce eq. 4.1 to a tractable mean field form, we have to discretize the equation. This results in discrete sites, which is the reason why we have drawn discrete cells in fig. 4.2. We split the system into N sites. Here the sites should be thought of as discretizing the continuum theory, where $u(\mathbf{x}, t)$ is the continuum variable we are discretizing. If we denote these sites as $u_i(t)$, then the equation of motion, derived from eq. 4.1 is

$$\eta \partial_t u_i(t) = \frac{\tilde{J}}{N} \sum_j (u_j(t) - u_i(t)) + \Sigma + f_i(u_i(t)) + \zeta_i(t) \tag{4.52}$$

where $f(u(\mathbf{x}, t), \mathbf{x}) \rightarrow f_i(u_i(t))$ and $\zeta(\mathbf{x}, t) \rightarrow \zeta_i(t)$. Then $\overline{f_i(u_i(t)) f_j(u'_j(t))} = \Delta(u - u')\delta_{ij}$ and $\langle \zeta_i \zeta_j \rangle = \delta_{ij}\delta(t - t')$, so that all of the continuous $\mathbf{x}$ coordinates have been replaced with indices. Here δ_{ij} denotes the Kronecker delta. We denote $J = \frac{\tilde{J}}{N}$, and the need for the $1/N$ normalization occurs because coupling with all sites would cause infinitely strong interactions otherwise.

The second big simplification we make is to discretize time. In this case, discretizing time imposes that we neglect the $\partial_t u_i(t)$ in eq. 4.52 except during times when large changes in $u_i(t)$ occur. And this only happens when $u_i(t)$ avalanches. Therefore, we must specify dynamics of how avalanches will occur in this model. In this case, we take as our stress

$$s_i(t) = J \sum_j (u_j(t) - u_i(t)) + \Sigma = J(\bar{u}(t) - u_i(t)) + \Sigma \tag{4.53}$$

where the $\bar{u}(t)$ denotes the mean over all sites u_j [6, 7, 13]. So in order to first incorporate the random forces which pin the $u_i(t)$, we assume that each site is pinned to a stress, so that s_i does not change unless there is an avalanche. The point at which s_i avalanches is when $s_i > s_{f,i}$, where $s_{f,i}$ is known as the failure stress for site i [7]. In this case, s_i relaxes down to an arrest stress which we call $s_{a,i}$. The failure and arrest stresses can be drawn from a random distribution, but we usually take the failure stress to be fixed at s_f for all sites to simplify the model [7]. We assume initially the stresses are uniformly distributed. After failure, the site's stress is redistributed to all other sites, so that each site $j \neq i$ has $\delta s_j = -\delta s_i/(N-1) = (s_f - s_{a,i})/(N-1)$. This increase in stress can cause another site to have $s_j > s_f$, which can result in a cascade, or slip avalanche. The arrest stresses $s_{a,i}$ are distributed according to a distribution $p_a(s_a)$ which we will consider to have mean $\langle s_a \rangle = 0$ and width $\langle s_a^2 \rangle - \langle s_a \rangle^2 \propto W^2 \ll s_f^2$, where $\langle \cdot \rangle$ denotes averaging over the distribution $p_a(s_a)$ [7, 13].

For this model, the distribution of stresses can be worked exactly [7]. For later use we review some of the material from [7]. We assume that $\Sigma < \Sigma_c$. After many failure events (needed to forget the initial conditions) the system settles into a stable distribution, as shown in [7]. For a given arrest stress, the stable distribution of stresses is distributed uniformly so that

$$p(s|s_a) = \frac{1}{s_m - s_a} \text{ for } s_a \leq s \leq s_m \tag{4.54}$$

where s_m is a maximum stress. We will solve for s_m below. Note that s_m is the not the failure stress s_f, because we have assumed that $\Sigma < \Sigma_c$, so $s_m < s_f$. Then $p(s) = \int ds_a p(s|s_a)p_a(s_a)$ or

$$p(s) = \int_{-W/2}^{s} ds_a \frac{p_a(s_a)}{s_m - s_a} \tag{4.55}$$

for any distribution that has a width W, and mean zero. If $s > W/2$ then the integral is clearly constant and therefore

$$p(s) = \bar{p} = \langle (s_m - s_a)^{-1} \rangle \tag{4.56}$$

is a uniform distribution.

If we order the stresses so that $s_0 > s_1 > \ldots > s_{N-1}$, then letting $\delta s_i = s_i - s_{i+1}$, we observe that given the uniform distribution eq. 4.56, the probability of observing s_i after observing s_{i+1} does not change as we move up in stress. Therefore δs_i is an exponentially distributed variable with mean $1/\bar{p}N$, as was derived for the mean field model of earthquakes [7]. We can express s_i as

$$s_i = s_{N-1} + \sum_{n=i}^{N-1} \delta s_n \tag{4.57}$$

$$\langle s_i \rangle = \langle s_{N-1} \rangle + \sum_{n=i}^{N-1} \langle \delta s_n \rangle \approx \sum_{n=i}^{N-1} \frac{n}{N\bar{p}} = \frac{N-i}{N\bar{p}} \tag{4.58}$$

where we assumed $\langle s_{N-1} \rangle \approx 0$. From eq. 4.53, we have that

$$\Sigma = \langle s \rangle = \frac{1}{N} \sum_i \langle s_i \rangle \approx \frac{1}{2\bar{p}} \approx \frac{s_m}{2} - \frac{\langle s_a^2 \rangle}{2 s_m} + \mathcal{O}(W^4/s_m^3) \tag{4.59}$$

where in the last line we expanded eq. 4.55 since $W \ll s_m$. At Σ_c, we should have that $s_m = s_f$, since at this point the infinite system should have at least one site that is always at the failure stress (i.e. it is in a state of constant avalanching) resulting in

$$\Sigma_c \approx \frac{s_f}{2} - \frac{\langle s_a^2 \rangle}{s_f} \tag{4.60}$$

We will use this result later in chapter 6.

At this point, we remind the reader of three different, but equivalent methods that describe the disorder. The first is the original disorder force $f(u)$, which we take as a function of u only since it is uncorrelated in the $\mathbf{x}$ direction. The second is the disorder potential $V(u)$, which is equivalent to the potential that would arise from the disorder force $f(u)$. The third is the disorder force correlator (which we call the disorder correlator) $\overline{f(u)f(u')} = \Delta(u-u')$, which played a prominent role in the renormalization of the equations of motion.

Various types of disorder forces $f(u)$ (or equivalently disorder potential $V(u)$) will determine the exponent γ, so that the energy barriers $\Delta E \propto (\Sigma_c - \Sigma)^{\gamma}$. For smooth disorder forces (i.e. no discontinuity of the derivative), this results in $\gamma = 3/2$ [155, 154]. We need a type of disorder force that will reproduce the renormalized disorder correlator at zero temperature in eq. 4.50. The disorder force must result in a correlator which is cusped at the origin, as shown in fig. 4.4, which as we have shown above is necessary for the presence of a critical force. The zero temperature disorder correlator is known to arise from a potential that meets at cusps [11].

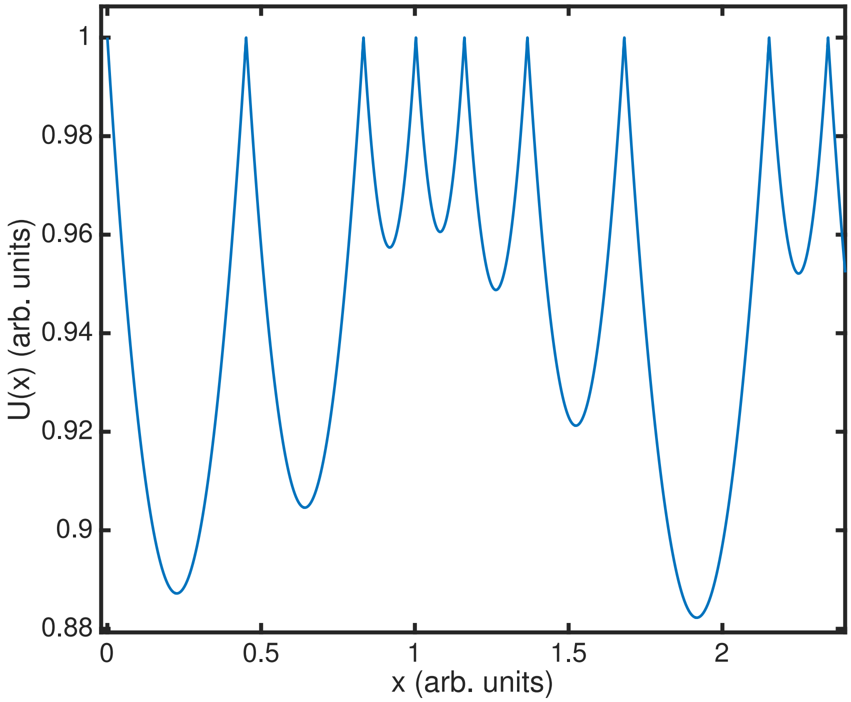

Figure 4.5: An example of the disorder potential $V(u)$ in $d=1$. The $d=2$ case is readily understandable as an extension of this potential. The cusped potential is an example of a potential that causes a cusped force correlator $\overline{f(u)f(u')} = \Delta(u-u')$, and is the result of RG flow [11, 166].

An example of the cusped potential is shown in fig. 4.5, which shows what are essentially a random sequence of harmonic wells placed together. For this kind of cusped potential, the exponent $\gamma = 2$ [154], and that this cusped potential is also responsible for another observed exponent, $\beta = 1$ [10, 6, 13]. Note that in the case of a rounded potential (i.e. $\Delta'(0) = 0$) the exponent $\gamma = 3/2$, and the exponent $\beta = 3/2$ [167]. Since $\beta = 1$ is usually observed [13], we expect that at the prediction $\gamma = 2$ is the correct limit of the behavior at the upper critical dimension. We will use this result together with the critical force eq. 4.60 to determine how the distribution of times between activation events (interevent times) changes with temperature and applied stress in chapter 6. In the chapter 5 appendices, we will show how the cusped disorder potential results in an energy barrier with exponent $\gamma = 2$ [154].

Chapter 5

Simulation of Creep

5.1 Introduction

In the previous chapter, we found that plastic deformation, as we study it in $d = 2$ can be understood at the level of mean field theory, as the equations describing creep have an upper critical dimension $d_c = 2$. As we showed before, for stresses $\Sigma < \Sigma_c$ (the critical stress), motion of a shear plane is impeded by the presence of disorder at $T = 0$. At $T > 0$, this no longer happens, because thermal activation above disorder energy barriers will allow motion of the shear plane. Near $T \to 0$ (for $\Sigma < \Sigma_c$) however, the motion of this plane happens very slowly, and we will derive the distribution of times between such activation events, known as the interevent times in chapter 6. In this chapter, we show how to simulate the slip events.

There have been many attempts to simulate creep motion. Perhaps the simplest method is to numerically integrate a Langevin equation of the form

$$\eta \partial t u_i = \sum_j J_{ij}(u_j - u_i) + \Sigma + f_{p,i}(u_i) + \zeta, \tag{5.1}$$

which has been done for short range interactions [168], but not long range interactions. The problem with the Langevin approach is that creep motion is often so slow that simulation times can be very long. Here $\zeta \propto \sqrt{T}\xi$, where T is the temperature and ξ is a Gaussian random variable with mean zero and variance 1 [155]. Therefore for small T the problem is essentially that large values of the random number ζ will not occur with a high frequency as a function of time. These simulation times diverge in the $T \to 0$ limit as $e^{U_c/T}$, where U_c is the energy barrier between metastable states. A similar problem will plague any molecular dynamics simulations of creep [169, 170].

Another option is to use a form of activation dynamics coupled with the zero temperature mean field equations given in mean field section of chapter 4. In these types of discrete simulations, the thermal noise ζ is replaced by some other form of activation. The challenge of systematically replacing a Gaussian random variable ζ with another form of noise is that it is not trivial to do this in a way that reproduces the statistics observed through the more physical Langevin approach. A Kinetic Monte Carlo (KMC) approach is usually adopted in this case [171, 172, 173, 174].

5.2 Kinetic Monte Carlo

The goal of Kinetic Monte Carlo algorithms when simulating thermal activation is to try transitioning the simulated system from one metastable state to another. In order to add thermal activation to the zero temperature model, we use a KMC algorithm. The advantage of using KMC is that such an algorithm avoids the rejection sampling methods of Markov Chain Monte Carlo (MCMC) [175]. Rejection sampling allows moves in MCMC to be rejected with some probability, typically dependent on temperature as $p_r/p_a \sim \exp(-\Delta E/k_B T)$. Here ΔE is an energy barrier to activation with p_r being the rejection probability, and p_a being the cumulative activation probability. At low temperatures, $\Delta E/k_B T$ can be large, so that many rejections happen before a valid activation event to another metastable state. However, KMC is particularly suited to systems which evolve slowly with time. In lieu of a rejection probability, KMC keeps track of a temporal variable t. The algorithm only considers valid movement between metastable states, and updates the time variable t to keep track of how long the system spends in a given metastable state.

Let us review a derivation of the KMC algorithm from first principles because this will be important in the following discussion [176]. Given a Langevin equation like eq. 5.1, we can recast our equation to try and find the probability distribution. Let the state of the system at any time step be $X(t) = [s_0(t), s_1(t), \ldots, s_{N-1}(t)]^T$, where the $s_i(t)$ are the various stresses mentioned in eq. 4.52 and the superscript T means transpose. Let $P\{X(t) = \mathbf{s}_\mu\}$ represent the probability that $X(t) = \mathbf{s}_\mu$ at some time t, where $\mathbf{s}_\mu$ represents different possible states of the vector $[s_0(t), s_1(t), \ldots, s_{N-1}(t)]^T$. Greek subscripts like μ and ν denote the enumeration of possible states of the full vector such as $\mathbf{s}_\mu = [s_0(t), s_1(t), \ldots, s_{N-1}(t)]^T$. Additionally, we must take into account the dynamics specified previously. Those dynamics were for a specific transition, when the stress s_i exceeds the failure stress s_f. In this case the allowed transition was to a state with $s_i = s_{a,i}$, where $s_{a,i}$ is the arrest stress. Therefore only transitions between $s_i \to s_{a,i}$ are available. In other words, either a site fails at a given transition or it remains pinned at a given stress $s_i < s_f$. They can be categorized as each site either failing or remaining pinned. Since each site can either remain pinned or fail, each site has two possible transitions, so for N sites there are 2^N possible transitions.

We are primarily interested in two quantities for Monte Carlo simulation. These are the transition rates $q_{\mathbf{s}_\mu \mathbf{s}_\nu}$ from state $\mathbf{s}_\mu$ to state $\mathbf{s}_\nu$ (the order of the subscripts is important in the definition of $q_{\mathbf{s}_\mu \mathbf{s}_\nu}$) and the probability that the state is in the state $\mathbf{s}_\mu$, $P\{X(t) = \mathbf{s}_\mu\}$. The transition rates $q_{\mathbf{s}_\mu \mathbf{s}_\nu}$ are defined as

$$P\{X(t + \delta t) = \mathbf{s}_\nu | X(t) = \mathbf{s}_\mu\} = q_{\mathbf{s}_\mu \mathbf{s}_\nu} \delta t \tag{5.2}$$

which gives the conditional probability that if $X(t) = \mathbf{s}_\mu$ at time t, $X(t+\delta t) = \mathbf{s}_\nu$ at some infinitesimal time later $t + \delta t$. Then the probability that at time t, the state is $\mathbf{s}_\mu$, $P\{X(t) = \mathbf{s}_\mu\}$, evolves to time $t + \delta t$

$$\begin{aligned} P\{X(t + \delta t) = \mathbf{s}_\mu\} = P\{X(t) = \mathbf{s}_\mu\} + \sum_{\mathbf{s}_\nu \neq \mathbf{s}_\mu} P\{X(t + \delta t) = \mathbf{s}_\mu | X(t) = \mathbf{s}_\nu\} P\{X(t) = \mathbf{s}_\nu\} \\ - \sum_{\mathbf{s}_\nu \neq \mathbf{s}_\mu} P\{X(t + \delta t) = \mathbf{s}_\nu | X(t) = \mathbf{s}_\mu\} P\{X(t) = \mathbf{s}_\mu\} \end{aligned} \tag{5.3}$$

where the first term on the right hand side is the current probability $P\{X(t) = \mathbf{s}_\mu\}$, the second term represents the probability that any state $\mathbf{s}_\nu$ transitions into $\mathbf{s}_\mu$ in time δt (and hence add to the probability), and the third term represents all probability of transitioning from $\mathbf{s}_\mu$ to other states $\mathbf{s}_\nu$ with within time δt (and hence subtract from the probability). Using eq. 5.2 we have

$$P\{X(t + \delta t) = \mathbf{s}_\mu\} = P\{X(t) = \mathbf{s}_\mu\} + \sum_{\mathbf{s}_\nu \neq \mathbf{s}_\mu} q_{\mathbf{s}_\nu \mathbf{s}_\mu} \delta t P\{X(t) = \mathbf{s}_\nu\} - q_{\mathbf{s}_\mu \mathbf{s}_\nu} \delta t P\{X(t) = \mathbf{s}_\mu\} \tag{5.4}$$

$$\frac{P\{X(t + \delta t) = \mathbf{s}_\mu\} - P\{X(t) = \mathbf{s}_\mu\}}{\delta t} = \sum_{\mathbf{s}_\nu \neq \mathbf{s}_\mu} q_{\mathbf{s}_\nu \mathbf{s}_\mu} P\{X(t) = \mathbf{s}_\nu\} - q_{\mathbf{s}_\mu \mathbf{s}_\nu} P\{X(t) = \mathbf{s}_\mu\} \tag{5.5}$$

$$\frac{dP\{X(t) = \mathbf{s}_\mu\}}{dt} = \sum_{\mathbf{s}_\nu \neq \mathbf{s}_\mu} q_{\mathbf{s}_\nu \mathbf{s}_\mu} P\{X(t) = \mathbf{s}_\nu\} - q_{\mathbf{s}_\mu \mathbf{s}_\nu} P\{X(t) = \mathbf{s}_\mu\} \tag{5.6}$$

which is known as the master equation of Markov chains [176]. Note that in assuming that $P\{X(t+\delta t) = \mathbf{s}_\mu\}$ depends only on the time immediately prior in eq. 5.2, we have assumed the Markov property. Additionally, by assuming the fact that the transition rates (defined in eq. 5.2) $q_{\mathbf{s}_\mu \mathbf{s}_\nu}$ are time independent, we have assumed that we are dealing with a time-homogeneous Markov chain, where the rates do not depend on time. This is justified since we are considering the steady state regime of creep motion, for which the system has forgotten the initial conditions that cause creep motion, so we can ignore time dependence of $q_{\mathbf{s}_\mu \mathbf{s}_\nu}$. As consequence of the time independence of the rates $q_{\mathbf{s}_\mu \mathbf{s}_\nu}$, we can find a simple expression for the interevent time given the current state.

Let $T_{\mathbf{s}_\mu}$ denote the duration that the system is in state $\mathbf{s}_\mu$. The duration $T_{\mathbf{s}_\mu}$ is important because it represents how long the system spends in state $\mathbf{s}_\mu$, which is important when considering the interevent time between two events (transitions). The cumulative distribution function of $T_{\mathbf{s}_\mu}$, denoted $P(T_{\mathbf{s}_\mu} > t)$ is the simplest quantity we can use to find the distribution of $T_{\mathbf{s}_\mu}$. We use the conditional probability

$P\{X(t+\delta t) = \mathbf{s}_\mu | X(t) = \mathbf{s}_\mu\}$ to help us with this problem. Here $P\{X(t+\delta t) = \mathbf{s}_\mu | X(t) = \mathbf{s}_\mu\}$ is the probability that the state remains in $\mathbf{s}_\mu$ for time δt, conditioned on the fact that at time t it is in state $\mathbf{s}_\mu$. We have

$$P(T_{\mathbf{s}_\mu} > t + \delta t) = P\{X(t+\delta t) = \mathbf{s}_\mu | X(t) = \mathbf{s}_\mu\} P(T_{\mathbf{s}_\mu} > t), \tag{5.7}$$

In words, the above equation states that the probability that the system remains in state $\mathbf{s}_\mu$ at time $t + \delta t$ is the probability that it has remained in state $\mathbf{s}_\mu$ till time t multiplied by the probability that it does not transition within time δt. Since the state must remain in $\mathbf{s}_\mu$ or transition to another state $\mathbf{s}_\nu \neq \mathbf{s}_\mu$,

$$P\{X(t+\delta t) = \mathbf{s}_\mu | X(t) = \mathbf{s}_\mu\} + \sum_{\mathbf{s}_\nu \neq \mathbf{s}_\mu} P\{X(t+\delta t) = \mathbf{s}_\nu | X(t) = \mathbf{s}_\mu\} = 1 \tag{5.8}$$

and we can apply eq. 5.2 so that

$$P\{X(t+\delta t) = \mathbf{s}_\mu | X(t) = \mathbf{s}_\mu\} = 1 - \sum_{\mathbf{s}_\nu \neq \mathbf{s}_\mu} P\{X(t+\delta t) = \mathbf{s}_\nu | X(t) = \mathbf{s}_\mu\} \tag{5.9}$$

$$P\{X(t+\delta t) = \mathbf{s}_\mu | X(t) = \mathbf{s}_\mu\} = 1 - \sum_{\mathbf{s}_\nu \neq \mathbf{s}_\mu} q_{\mathbf{s}_\mu \mathbf{s}_\nu} \delta t \tag{5.10}$$

which we can then plug into eq. 5.7 to get

$$P(T_{\mathbf{s}_\mu} > t + \delta t) = \left(1 - \sum_{\mathbf{s}_\nu \neq \mathbf{s}_\mu} q_{\mathbf{s}_\mu \mathbf{s}_\nu} \delta t\right) P(T_{\mathbf{s}_\mu} > t) \tag{5.11}$$

$$\frac{P(T_{\mathbf{s}_\mu} > t + \delta t) - P(T_{\mathbf{s}_\mu} > t)}{\delta t} = - \sum_{\mathbf{s}_\nu \neq \mathbf{s}_\mu} q_{\mathbf{s}_\mu \mathbf{s}_\nu} P(T_{\mathbf{s}_\mu} > t) \tag{5.12}$$

$$\frac{dP(T_{\mathbf{s}_\mu} > t)}{dt} = - \sum_{\mathbf{s}_\nu \neq \mathbf{s}_\mu} q_{\mathbf{s}_\mu \mathbf{s}_\nu} P(T_{\mathbf{s}_\mu}) \tag{5.13}$$

$$r_{\mathbf{s}_\mu} = \sum_{\mathbf{s}_\nu \neq \mathbf{s}_\mu} q_{\mathbf{s}_\mu \mathbf{s}_\nu} \tag{5.14}$$

$$\frac{dP(T_{\mathbf{s}_\mu} > t)}{dt} = -r_{\mathbf{s}_\mu} P(T_{\mathbf{s}_\mu}) \tag{5.15}$$

$$P(T_{\mathbf{s}_\mu} > t) = e^{-r_{\mathbf{s}_\mu} t}. \tag{5.16}$$

Hence we arrive at the very simple exponential distribution to describe the persistence time of a state.

That we arrived at an exponential distribution is a little disturbing given that we have made only a few simple assumptions, particularly that of the transitions $q_{\mathbf{s}_\mu \mathbf{s}_\nu}$ are time-independent and the system is Markovian. However, as we will see, although the transitions $q_{\mathbf{s}_\mu \mathbf{s}_\nu}$ do not depend on time, implicitly they must still depend on the state of the system. Therefore, we must integrate over all possible states to find the correct distribution of interevent times. Although Markov chains are often used to model systems with a small number of states, in this case, the state of the system $X(t) = \mathbf{s}_\mu$ denotes not just a scalar quantity, but a full vector of quantities describing the position discontinuities of the shear band.

The exponential waiting times hints at the possibility of simulating eq. 5.6 without fully integrating the equation. Given an initial state $\mathbf{s}_\mu$, the time to transition out of the state is just an exponential random variable with mean $1/r_{\mathbf{s}_\mu} = 1/\sum_{\mathbf{s}_\nu \neq \mathbf{s}_\mu} q_{\mathbf{s}_\mu \mathbf{s}_\nu}$. Then the question becomes what state we land on after leaving state $\mathbf{s}_\mu$. Taking eq. 5.2, we can say that the transition

$$P\{X(t+\delta t) = \mathbf{s}_\nu | X(t+\delta t) \neq \mathbf{s}_\mu, X(t) = \mathbf{s}_\mu\}\delta t = P(T_{\mathbf{s}_\mu} > t) q_{\mathbf{s}_\mu \mathbf{s}_\nu} \delta t \tag{5.17}$$

$$P\{X(t+\delta t) = \mathbf{s}_\nu | X(t+\delta t) \neq \mathbf{s}_\mu, X(t) = \mathbf{s}_\mu\} = q_{\mathbf{s}_\mu \mathbf{s}_\nu} e^{-r_{\mathbf{s}_\mu} t}. \tag{5.18}$$

Then the transition itself happens with certainty by integrating over time, giving a transition probability

$$P_{\mathbf{s}_\mu \to \mathbf{s}_\nu} = \int_0^\infty dt q_{\mathbf{s}_\mu \mathbf{s}_\nu} e^{-r_{\mathbf{s}_\mu} t} \tag{5.19}$$

$$P_{\mathbf{s}_\mu \to \mathbf{s}_\nu} = \frac{q_{\mathbf{s}_\mu \mathbf{s}_\nu}}{r_{\mathbf{s}_\mu}} = \frac{q_{\mathbf{s}_\mu \mathbf{s}_\nu}}{\sum_{\mathbf{s}_\nu \neq \mathbf{s}_\mu} q_{\mathbf{s}_\mu \mathbf{s}_\nu}}. \tag{5.20}$$

In eq. 5.20, states $\mathbf{s}_\nu$ with larger transition rates $q_{\mathbf{s}_\mu \mathbf{s}_\nu}$ have a higher probability of being transitioned into. In eq. 5.20, the sum over all states $\mathbf{s}_\nu \neq \mathbf{s}_\mu$ results in unity, confirming that the transition probabilities assigned do represent a normalized probability distribution of states $\mathbf{s}_\nu$ to select after transitioning from $\mathbf{s}_\mu$. Note that this is a probability distribution over all position states $\mathbf{s}_\nu$ that can result after a transition out of state $\mathbf{s}_\mu$, since the various rates $q_{\mathbf{s}_\mu \mathbf{s}_\nu}$ depend on both the pre-transition state $\mathbf{s}_\mu$ and the various possible post-transition states $\mathbf{s}_\nu$.

With the results eq. 5.16 and eq. 5.20, it is simple to specify the KMC algorithm [170]. Sometimes this is known as the Bortz-Kalos-Lebowitz (BKL) algorithm [175] or the Gillespie algorithm [177]. We use the term kinetic monte carlo in this thesis.

1. Calculate the total rate of transition out of state $\mathbf{s}_\mu$

$$r_{\mathbf{s}_\mu} = \sum_{\mathbf{s}_\nu \neq \mathbf{s}_\mu} q_{\mathbf{s}_\mu \mathbf{s}_\nu}. \tag{5.21}$$

2. Select a random number ρ_0 uniformly from $[0, r_{\mathbf{s}_\mu})$.

3. The state $\mathbf{s}_\nu$ that results after transitioning out of state $\mathbf{s}_\mu$ is selected as the state for which

$$\sum_{\mathbf{s}_\kappa \neq \mathbf{s}_\mu}^{\mathbf{s}_{\nu-1}} q_{\mathbf{s}_\mu \mathbf{s}_\kappa} \leq \rho_0 < \sum_{\mathbf{s}_\kappa \neq \mathbf{s}_\mu}^{\mathbf{s}_\nu} q_{\mathbf{s}_\mu \mathbf{s}_\kappa}. \tag{5.22}$$

   where the sum is over all possible transitions $\mathbf{s}_\mu \to \mathbf{s}_k$, and we have assumed that they can be enumerated $\mathbf{s}_1, \mathbf{s}_2, \ldots, \mathbf{s}_M$. The schematic version of this will be shown below in fig. 5.1. This is equivalent to sampling a random transition from the distribution $P_{\mathbf{s}_\mu \to \mathbf{s}_\nu} = q_{\mathbf{s}_\mu \mathbf{s}_\nu} / r_{\mathbf{s}_\mu}$.

4. Carry out the transition $\mathbf{s}_\mu \to \mathbf{s}_\nu$ through the zero temperature algorithm [7]. We find the time elapsed by drawing an exponential random variable with rate constant $r_{\mathbf{s}_\mu}$ as the time needed to transition out of state $\mathbf{s}_\mu$.

5. Update the rates to reflect the new state, and begin again with step 1.

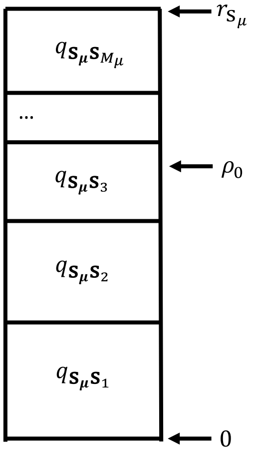

Figure 5.1: A schematic example of how step 3 in the KMC works. We call the current state $\mathbf{s}_\mu$. We put all the potential post-transition states $\mathbf{s}_\nu$ into a list $\mathbf{s}_1$ to $\mathbf{s}_{M_{\mathbf{s}_\mu}}$ and calculate the rates $q_{\mathbf{s}_\mu \mathbf{s}_\nu}$ for each transition. Here $M_{\mathbf{s}_\mu}$ is the total number of transitions possible (which is dependent on the state $\mathbf{s}_\mu$ itself). Then we sum these rates to get $r_{\mathbf{s}_\mu}$, and draw a random number ρ_0 from $[0, r_{\mathbf{s}_\mu})$. We select the state to transition to based on what index the inequality eq. 5.22 holds. For example, in the above picture, we would pick the transition $\mathbf{s}_\mu \to \mathbf{s}_3$.

The most important part of this algorithm is that it is rejection free, so that at every time step of the algorithm (steps 1-5 constitute 1 time step) the state transitions to a different state. This avoids the problem of rejection based monte carlo, which would typically be stuck in a single metastable state if the energy barriers are large relative to the temperature.

Naively this algorithm would run in $\mathcal{O}(M)$ time, where $M = \langle M_{\mathbf{s}_\mu} \rangle$ is the average number of transitions in each state $\mathbf{s}_\mu$. Improvements have been made so that step 3 requires only $\mathcal{O}(\log(M))$ time, but those also require the storage of $\mathcal{O}(M)$ partial sums [178]. If each rate changes at every step, then no algorithm currently allows for less than $\mathcal{O}(M)$ time because of the calculation involved in step 1 and the update involved in step 5.

5.3 Creep Using Kinetic Monte Carlo

In the simulation of creep, there are two problems faced in using KMC. The first is known as the futility problem. If the system is stuck in a relatively flat well of the potential, transitions will move the system locally within this flat well [179]. However, the system will not evolve because it will not escape this flat well. This problem manifests itself in KMC by transitions to and from a given configuration repeatedly. We avoid this problem by staying in the low temperature regime, and by assuming that the stress Σ/Σ_c on the system close to unity. Near the critical stress, energy barriers for backwards slips are exponentially larger than energy barriers for forward slips, as we will show below. Since we are concerned especially with creep near the critical force Σ_c [155], we neglect backwards motion of the slip plane. We assume the scaling form eq. 4.6 is the correct form of energy barrier scaling for the system. Each site can only slip forwards if it overcomes an energy barrier

$$\Delta E_i = \Omega(s_{f,i} - s_i)^\gamma = \Omega \delta s^\gamma, \tag{5.23}$$

which is a common form for the energy barrier [155, 180, 154]. The exponent γ depends the shape of the pinning potential, and with the cusped potential we plotted in fig. 4.5 the resulting value is $\gamma = 2$ [155, 154]. Here Ω is a constant independent of the stress. As a rough estimate to how good an approximation it is to neglect backwards slips, we note that the forward energy barrier is $\Delta E_f \approx \Omega(\Sigma_c - \Sigma)^\gamma$, while the backwards energy barrier is $\Delta E_b \approx \Omega(\Sigma_c + \Sigma)^\gamma$. Therefore, the ratio of probabilities of a backwards slip to a forwards slip is approximately $\exp\left[-\Omega((\Sigma_c + \Sigma)^\gamma - (\Sigma_c - \Sigma)^\gamma)/k_B T\right] \approx \exp\left[-\Omega(2\Sigma_c)^\gamma/k_B T\right] \ll 1$ for F close to F_c. A slip forwards to another state means that the site i that has failed relaxes to its arrest stress $s_{a,i}$, while redistributing its previous stress s_i to all other sites. The redistribution of stress can result in an avalanche, which will scramble the stresses of all other sites. This leads to the second problem encountered in KMC simulations of creep.

The second problem faced by KMC methods to simulate creep is what we term the combination problem. At the beginning of the KMC, we must calculate the total rate constant $r_{\mathbf{s}_\mu}$. Recalling our discussion about the state of the system, we note that the state of the system is a vector quantity with N entries. Each site in the system can either fail or remain at its current stress, so each entry can be labeled by a 1 for failure and a 0 otherwise. Each KMC step can involve more than a single site, and it is known that large combinations of activation events are required to properly simulate the creep problem [181, 182, 180] at finite temperature. For proper KMC simulation, each possible combination of failing cells must be taken into account. For N sites, each site has 2 transitions, either staying fixed or failing, resulting in 2^N possible transitions. In counting the number of transitions, the transition where all sites stay fixed should not be counted, so there are $2^N - 1$ total transitions possible. In other words, a direct implementation of the algorithm would run in $\mathcal{O}(2^N)$ time. Several other papers have attempted to address this problem in the context of short range interactions, by assuming only sites locally connected to each other will fail [182] in their MC calculations or assuming the temperature is so low that only single site failures are possible [180, 183]. In mean field theory, this problem is more acute because each site is coupled to every other site, and the notion of locality does not exist. This problem is also present in any system with long range interactions. Therefore, each possible combination of site failures must be accounted for in a proper KMC simulation.

Our main contribution is to show that for a certain class of rate constants, there is an algorithm that finds exactly the sum of all the rate constants within $\mathcal{O}(N^2)$ time and $\mathcal{O}(N^2)$ memory. In addition to this, there is a related algorithm that finds a selected state that is needed to execute step 4 of the KMC with the correct probability of transition in eq. 5.20.

In order to describe this algorithm, it is best to fix the notation for multiple activation events. First, we will need notation for summing over multiple activation events. In this case, we will use numbered indices $i_1, i_2, \ldots, i_m$, where each index $1 \leq i_p \leq N$ can run over the full set of possible values. Second we will assume that the rate constants for single activation events are of the form $k_i = \lambda_0 e^{-\Delta E_i / k_B T}$, where ΔE_i is the energy barrier of the ith site, and λ_0 is a constant needed for correct units. For example, if the 3rd site is considered, we will assume a rate constant of activation $k_3 = \lambda_0 e^{-\Omega (s_f - s_3)^\gamma / k_B T}$, where k_3 denotes that the third site is considered for failure. Again the constant λ_0 is needed to correct units. In general this simple form of activation rates is probably not true [184, 170], as the constant λ_0 is not a true constant as ΔE varies. In other words, $\lambda_0 = \lambda_0(\Delta E_i)$. However, both for simplicity, and because the dependence of λ_0 on energy barriers is usually polynomial [184] rather than exponential, we expect to capture much of the first order behavior by assuming λ_0 is a constant as ΔE is varied. For general single activation events we have

$$\lambda_i = e^{-\Omega (s_f - s_i)^\gamma / k_B T} \tag{5.24}$$

$$k_i = \lambda_0 e^{-\Omega (s_f - s_i)^\gamma / k_B T} = \lambda_0 \lambda_i, \tag{5.25}$$

where again, we have assumed that λ_0 is a constant of proportionality needed for correct units that to lowest order does not vary as ΔE is varied. In trying to touch notation with the previous discussion, $k_i = q_{\mathbf{s}_\mu \mathbf{s}_\nu} = q_{[s_{\mu,0},\ldots,s_{\mu,i},\ldots,s_{\mu,N-1}]^T \to [s_{\nu,0},\ldots,s_{\nu,i},\ldots,s_{\nu,N-1}]^T}$. In this case, if the ith site has failed, then $s_{\nu,i} = s_{a,i}$ (the arrest stress for the ith site). The notation k_i can also be extended to multiple slips by including more indices so that

$$k_{i_1,i_2,\ldots,i_m} = \lambda_0 e^{-\Omega\{(s_f - s_{i_1})^\gamma + (s_f - s_{i_2})^\gamma + \ldots + (s_f - s_{i_m})^\gamma\}/k_B T} = \lambda_0 \lambda_{i_1} \lambda_{i_2} \ldots \lambda_{i_m}. \tag{5.26}$$

Since this form is more compact than writing $\mathbf{s}_\mu$ and $\mathbf{s}_\nu$ for each specific combination of failures, we use this notation in the following discussion. In eq. 5.26, we have made the important assumption that the rate constants do not take into account interactions between sites. In reality this assumption is only valid up to $\mathcal{O}(1/N)$ in mean field theory, because clearly if more than 1 site fails, their mutual interaction (since $J \sim \mathcal{O}(1/N) > 0$) will make it easier for other sites to fail simultaneously. In fact, it is possible to take into account the $\mathcal{O}(1/N)$ term and arrive at an algorithm which is accurate to $\mathcal{O}(1/N^2)$, which we describe in the appendices. This algorithm can be extended to $\mathcal{O}(1/N^l)$ for any l, but unsurprisingly the time for simulation then grows like $\mathcal{O}(N^2 l!)$. We will not pursue this line of inquiry as it is inessential in the limit $N \to \infty$.

Let us call the current state of the system $\mathbf{s}_\mu$. Then we must first compute $r_{\mathbf{s}_\mu}$. The general strategy to compute $r_{\mathbf{s}_\mu}$ is to compute the sum eq. 5.21 in terms of single site activations, pair activations, and so on, which we label by an integer m. For example, $m = 1$ means we only consider single site failures, while $m = 2$ means we consider pairs of sites failing. Clearly $1 \leq m \leq N - 1$. Of course, such a sum eq. 5.21 will then take $\mathcal{O}(2^N)$ time, so to speed up the computation, we use results from computing the $m - 1$ combinations of failed sites to compute the sum for m combinations of failed sites. First we write

$$r_{\mathbf{s}_\mu} = \sum_{m=1}^{N-1} \sum_{1=i_1<i_2<\ldots<i_m}^{N} k_{i_1,i_2,\ldots,i_m} = \sum_{m=1}^{N-1} R_m \tag{5.27}$$

$$R_m = \sum_{1=i_1<i_2<\ldots<i_m}^{N} k_{i_1,i_2,\ldots,i_m} \tag{5.28}$$

where R_m is the sum of combinations of m sites failing, and the sum constraint $i_1 < i_2 < \ldots < i_m$ enforces that two indices are never the same (no site can fail twice!).

Initially, it is useful to have precomputed the rate constants λ_i from eq. 5.24, of which there are N terms. The starting point is to compute the $m = 1$ sum, which we will call R_1. Using eq. 5.28 and eq. 5.26 this is just

$$R_1 = \sum_{i=0}^{N-1} k_i = \sum_{i=1}^{N} \lambda_0 \lambda_i = \sum_{i=1}^{N} \lambda_0 e^{-\Omega(s_f - s_i)^\gamma / k_B T}. \tag{5.29}$$

This sum can be done in $\mathcal{O}(N)$ time. The $m = 2$ sum is more complicated, because it involves pairs of sites i_1, i_2

$$R_2 = \sum_{1=i_1<i_2}^{N} k_{i_1,i_2} = \sum_{1=i_1<i_2}^{N} \lambda_0 \lambda_{i_1} \lambda_{i_2} = \lambda_0 \sum_{1=i_1}^{N-1} \lambda_{i_1} \sum_{i_1<i_2}^{N} \lambda_{i_2}. \tag{5.30}$$

We can compute eq. 5.30 by keeping track of the partial sums while computing eq. 5.29 (dividing out the inessential factor of λ_0). Let us call these partial sums, which can be done with $\mathcal{O}(N)$ time and $\mathcal{O}(N)$ space

$$\sigma_{1,n} = \sum_{i=n}^{N} \lambda_i. \tag{5.31}$$

Then

$$R_2 = \sum_{i_1=1}^{N-1} \lambda_{i_1} \sigma_{1,i_1+1} \tag{5.32}$$

which can be computed in $\mathcal{O}(N)$ time. Comparatively, a direct computation of R_2 takes $\mathcal{O}(N^2)$ time, showing that for pairs we have a quadratic speedup. As a further example, let us compute

$$R_3 = \sum_{1=i_1<i_2<i_3}^{N} k_{i_1,i_2,i_3} = \sum_{1=i_1<i_2<i_3}^{N} \lambda_0 \lambda_{i_1} \lambda_{i_2} \lambda_{i_3} = \lambda_0 \sum_{i_1=1}^{N-1} \lambda_{i_1} \sum_{i_1<i_2}^{N-1} \lambda_{i_2} \sum_{i_2<i_3}^{N} \lambda_{i_3} \tag{5.33}$$

where we have again split the sum into pieces which can be computed from previous computations. Taking the partial sums

$$\sum_{i_2=n}^{N-1} \lambda_{i_2} \sum_{i_2<i_3}^{N} \lambda_{i_3} = \sum_{i_2=n}^{N-1} \lambda_{i_2} \sigma_{1,i_2+1} = \sigma_{2,n} \tag{5.34}$$

can be done again in linear time while computing eq. 5.32. Then

$$R_3 = \lambda_0 \sum_{i_1=1}^{N-2} \lambda_{i_1} \sigma_{2,i_1+1} \tag{5.35}$$

which can be done in linear time. So far we have a computation that can take about $\mathcal{O}(3N)$ time and $\mathcal{O}(3N)$ memory. Computing the sum eq. 5.33 directly would take $\mathcal{O}(N^3)$ time, as there are $\mathcal{O}(N^3)$ terms. At this point, it is probably easier to approach the general case

$$R_m = \lambda_0 \sum_{1=i_1<i_2<\ldots<i_m}^{N} \lambda_{i_1}\lambda_{i_2}\ldots\lambda_{i_m} \tag{5.36}$$

$$R_m = \lambda_0 \sum_{i_1=1}^{N-m+1} \lambda_{i_1} \sum_{i_1<i_2}^{N-m+2} \lambda_{i_2} \ldots \sum_{i_{m-1}<i_m}^{N} \lambda_{i_m} \tag{5.37}$$

$$R_m = \lambda_0 \sum_{i_1=1}^{N-m+1} \lambda_{i_1}\sigma_{m-1,i_1+1} \tag{5.38}$$

where

$$\sigma_{m-1,i_1+1} \equiv \sum_{i_2=i_1+1}^{N-m+2} \lambda_{i_2}\sigma_{m-2,i_2+1} \tag{5.39}$$

with the triple equals sign mean we define σ_{m-1,i_1+1} as the quantity on the right hand side.

This should make the full recursive nature of the computation clear. Basically we keep track of the partial sums $\sigma_{m-1,i}$ to compute $\sigma_{m,i}$, which we then use to compute R_m using eq. 5.38. Now

$$r_{\mathbf{s}_\mu} = \sum_{m=1}^{N-1} R_m \tag{5.40}$$

with each R_m taking $\mathcal{O}(N)$ time and storage. Since $1 \leq m \leq N-1$ the resulting algorithm is $\mathcal{O}(N^2)$ running time and storage.

If we now go back to the KMC algorithm, we still need to draw a random new state from the probability distribution $q_{\mathbf{s}_\mu \mathbf{s}_\nu}/r_{\mathbf{s}_\mu}$, where $\nu \neq \mu$ refers to a new state. Naively, this part of the computation is just as difficult as the first part, requiring $\mathcal{O}(2^N)$ computations. However, we can leverage many of the computations in the first part of the algorithm to reduce the time complexity to $\mathcal{O}(N^2)$. The algorithm presented below is similar to several combinatorial enumeration algorithms [185], except that it takes into account weighting of the combinations correctly.

First, we must come up with a way to more systematically order the set of possible transitions. Let $\{\cdot\}$ denote that a given set of sites fail. For example, $\{1, 2\}$ means sites 1 and 2 fail. Then there is a well defined ordering of possible transitions known as the dictionary order [185]. The formal definition is that if we have 2 sets of n items $\{\mu_1, \mu_2, \ldots, \mu_n\}$ and $\{\nu_1, \nu_2, \ldots, \nu_n\}$, then the first is less than the second if $\mu_i < \nu_i$ for the first i at which $\{\mu_1, \mu_2, \ldots, \mu_n\}$ and $\{\nu_1, \nu_2, \ldots, \nu_n\}$ differ. The ordering is similar to how words in a dictionary are ordered, which explains the namesake. More concretely, an example of the ordering is

$\{1,2,3\} < \{1,2,4\} < \{2,3,4\}$ and so on. The full set of possible transitions can be ordered as

$$\{1\} < \{2\} < \ldots < \{N\} < \{1,2\} < \{1,3\} < \ldots < \{N-1,N\} < \{1,2,3\} < \ldots < \{1,\ldots,N\}. \tag{5.41}$$

As a reminder to the reader, we have found the total rate constant $r_{\mathbf{s}_\mu}$ using eq. 5.40. We now need to find the state $\mathbf{s}_\nu$ to which $\mathbf{s}_\mu$ transitions. Given the general sum eq. 5.27, we can draw a random number $0 \leq \rho_0 < r_{\mathbf{s}_\mu}$. The state that we select can be labeled by a set of integers $\{\nu_1, \ldots, \nu_n\}$, where we assume that ρ_0 selects a transition where n sites fail. The integers $\nu_1, \ldots, \nu_n$ represent the sites that fail in a transition selected by the random number ρ_0. Recall from eq. 5.22 that the way this is done in KMC is to choose the state with $\sum_{\mathbf{s}_\kappa \neq \mathbf{s}_\mu}^{\mathbf{s}_{\nu-1}} q_{\mathbf{s}_\mu \mathbf{s}_\kappa} \leq \rho_0 < \sum_{\mathbf{s}_\kappa \neq \mathbf{s}_\mu}^{\mathbf{s}_\nu} q_{\mathbf{s}_\mu \mathbf{s}_\kappa}$. Note that the sums in the inequality are arbitrarily ordered, so that we can choose the dictionary ordering after labeling the sites from 1 to N. As we explain below, we have already computed $r_{\mathbf{s}_\mu}$ using dictionary ordering, we can take advantage of the ordering structure to find our list of failed sites. Let us state how the dictionary ordering is used in eq. 5.27. The very first term in computing $r_{\mathbf{s}_\mu}$ is just the rate constant that the site labeled 1 fails. The next term is that the site labeled 2 fails, and so forth. The full set of these single failed sites is what we originally called R_1, as defined in eq. 5.29. The second set of terms starts with the combination of sites $\{1,2\}$ failing, and so forth. Therefore, the sum is done in the dictionary order in our computation. Writing it out to be explicit,

$$r_{\mathbf{s}_\mu} = \sum_m R_m = k_1 + k_2 + \ldots + k_N + k_{1,2} + \ldots + k_{1,N} + \ldots + k_{N-1,N} + k_{1,2,3} + \ldots + k_{1,2,\ldots,N}. \tag{5.42}$$

The $k_{i_1,\ldots,i_n}$ represent the sites $i_1, \ldots, i_n$ slipping, and the sum is written dictionary order by comparing the subscripts of the ks to the definition of dictionary ordering eq. 5.41 above.

One can think of computing $r_{\mathbf{s}_\mu}$ as stacking boxes similar to figure 5.1, with the first layer of boxes being all single failed sites, the second layer of boxes being double failed sites, and so forth. An example of this is shown in the figure 5.2 below.

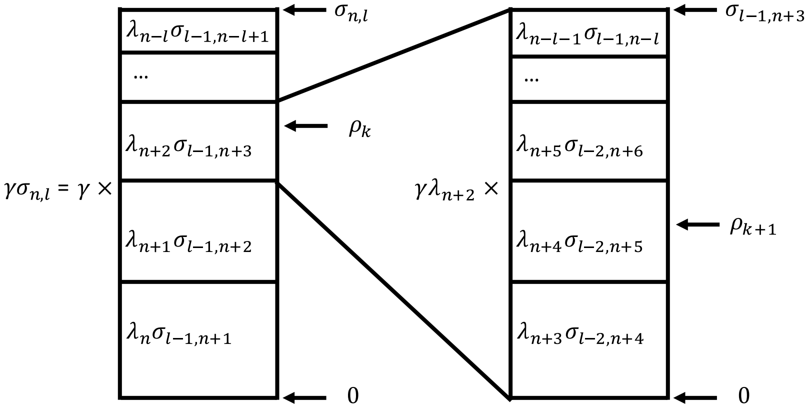

Figure 5.2: A schematic example of the algorithm to be described, similar to fig. 5.1. We have set $\lambda_0 = 1$ to simplify the number of variables. Here γ is a variable that keeps track of previous multipliers. We show here an example of a single iteration of the algorithm, here the kth iteration. The random number ρ_k selects the kth state that fails. In the case illustrated in the figure, that state is the third state from the bottom (on the left hand side). As can be seen on the left hand side of the figure, $\gamma\lambda_n\sigma_{l-1,n+1} + \gamma\lambda_{n+1}\sigma_{l-1,n+2} < \rho_k < \gamma\lambda_n\sigma_{l-1,n+1} + \gamma\lambda_{n+1}\sigma_{l-1,n+2} + \gamma\lambda_{n+2}\sigma_{l-1,n+3}$. Therefore, $0 < \rho_k - \gamma\lambda_n\sigma_{l-1,n+1} + \gamma\lambda_{n+1}\sigma_{l-1,n+2} < \gamma\lambda_{n+2}\sigma_{l-1,n+3}$, so we define $\rho_{k+1} = \rho_k - \gamma\lambda_n\sigma_{l-1,n+1} + \gamma\lambda_{n+1}\sigma_{l-1,n+2}$ and we know that $\rho_{k+1} \in [0, \gamma\lambda_{n+2}\sigma_{l-1,n+3})$. Therefore, the factor $\sigma_{l-1,n+3}$ is then expanded (i.e. written term by term using eq. 5.39) like the right hand side of the figure. In addition to this, the factor γ now becomes $\gamma\lambda_{n+2}$. Since this term is included, we know that $n+2$ labels one of the sites that has failed. The new term, ρ_{k+1}, lies within the expansion on the right hand side of the figure. This piece is then used to find the $k+1$th failure site (i.e. $n+5$), which is in this case the second from the bottom on the right hand side. The algorithm continues until $l = 0$, so that there are no more $\sigma_{l,n}$ to expand. The set of sites is enumerated by listing off the site selected by each ρ_k at each step.

To find the generic transition selected by the random number $0 \leq \rho_0 < r_{\mathbf{s}_\mu}$, we should group as many terms together as possible in the sum eq. 5.40 that computes $r_{\mathbf{s}_\mu}$. The very first thing we want to find is how many sites have failed, which we call the zeroth layer. For example, if the KMC algorithm selects a post-transition state using ρ_0 where 3 sites have failed, then we know that $R_1 + R_2 < \rho_0 < R_1 + R_2 + R_3$, since R_1 and R_2 denote the full sum of single and double failures, while R_3 describes the full sum of triple failures. In general, we know the R_i from the previous computation eq. 5.38, so if

$$R_1 + R_2 + \ldots + R_{n-1} < \rho_0 < R_1 + R_2 + \ldots + R_{n-1} + R_n \tag{5.43}$$

then n sites have failed. Then the state we select can be labeled by a set of integers $\{\nu_1, \ldots, \nu_n\}$. We know that $1 \leq \nu_p \leq N$, and since each ν_p with $1 \leq p \leq N$ is unique, we can order them so that $\nu_1 < \nu_2 < \ldots < \nu_n$.

In order to calculate the transition $\{\nu_1, \ldots, \nu_n\}$, we then have to plug in the definition of R_n using eq. 5.38, since R_n represents the full sum of n sites failing. This is the next layer that we compute. We know that the difference $\rho_1 = \rho_0 - (R_1 + R_2 + \ldots + R_{n-1})$ is in the interval $[0, R_n)$ by the above inequality eq. 5.43. Next, we can plug in R_n using eq. 5.38. As a reminder, the equation defining R_n is

$$R_n = \lambda_0 \sum_{i_1=1}^{N-n+1} \lambda_{i_1} \sigma_{n-1,i_1+1}. \tag{5.44}$$

We know that $0 < \rho_1 < R_n$, but since we have already computed each term in the sum defining R_n, we can actually find the index ν_1 at which

$$\lambda_0 \sum_{i=1}^{\nu_1-1} \lambda_i \sigma_{n-1,i+1} < \rho_1 < \lambda_0 \sum_{i=1}^{\nu_1} \lambda_i \sigma_{n-1,i+1}. \tag{5.45}$$

From here, want know that ρ_1 has selected a state that includes an index ν_1. In order to find further indices, we must write out the terms in layer (i.e. write out the term $\lambda_0 \lambda_{\nu_1} \sigma_{n-1,\nu_1+1}$ just like the right half of figure 5.2). We can define $\rho_2 = \rho_1 - \lambda_0 \sum_{i=1}^{\nu_1-1} \lambda_i \sigma_{n-1,i+1}$ since we will then know that ρ_2 is in the interval $[0, \lambda_0 \lambda_{\nu_1} \sigma_{n-1,\nu_1+1})$. In addition, we now know that ν_1 is one of the activated sites. We can expand σ_{n-1,i_1+1} recursively using eq. 5.39, at each step subtracting the correct amount and multiplying by any collected prefactors to find the indices $\nu_2, \ldots, \nu_n$.

Let us go through this procedure for the next layer to find ν_2 before explaining the general algorithm. The first thing we will do is expand σ_{n-1,ν_1+1} using eq. 5.39. We know that $\rho_2 \in [0, \lambda_0 \lambda_{\nu_1} \sigma_{n-1,\nu_1+1})$, so we must multiply our expansion of σ_{n-1,ν_1+1} by $\lambda_0 \lambda_{\nu_1}$.

Then to find the next index, which we call ν_2, we simply look for the index

$$\lambda_0 \lambda_{\nu_1} \sum_{i=\nu_1+1}^{\nu_2-1} \lambda_i \sigma_{n-2,i+1} < \rho_2 < \lambda_0 \lambda_{\nu_1} \sum_{i=\nu_1+1}^{\nu_2} \lambda_i \sigma_{n-2,i+1} \tag{5.46}$$

Note that above the summation starts on $\nu_1 + 1$, and hence $\nu_2 > \nu_1$, as expected from our assumption that $\nu_1 < \nu_2 < \ldots < \nu_n$. Now the next step is to define $\rho_3 = \rho_2 - \lambda_{\nu_1} \sum_{i=\nu_1+1}^{\nu_2-1} \lambda_i \sigma_{n-2,i+1}$ and expand σ_{n-2,ν_2+1}. We will have a string of prefactors $\lambda_0 \lambda_{\nu_1} \lambda_{\nu_2} \ldots$ that we must track. We call this overall prefactor γ, initially with $\gamma = \lambda_0$. We specify the full algorithm now for finding these indices starting from ν_1. For each iteration, we let t be the iteration, starting with $t = 1$. We will terminate once we have all n sites. We will use the notation $\sigma_{l,m}$ to refer generically to the various sums we must expand using eq. 5.39.

1. Initialize $\gamma_1 = \lambda_0, m_1 = 1$, and $l_1 = n$, where n is the number of sites that will fail determined by eq. 5.45.

2. **for** $t = 1,\, t \leq n,\, t \to t+1$

    2.1. Expand σ_{l_t,m_t} using eq. 5.39 while keeping track of the total mulitplier γ

    $$\gamma_t \sigma_{l_t,m_t} = \gamma \sum_{i=m_t}^{N-l_t+1} \lambda_i \sigma_{l_t-1,i+1} \tag{5.47}$$

    2.2. Find the index ν_t where

    $$\gamma \sum_{i=m_t}^{\nu_t-1} \lambda_i \sigma_{l_t-1,i+1} < \rho_t < \gamma \sum_{i=m_t}^{\nu_t} \lambda_i \sigma_{l_t-1,i+1}. \tag{5.48}$$

    2.3. Store the value ν_t, setting:

    $$l_{t+1} = l_t - 1 \tag{5.49}$$

    $$m_{t+1} = \nu_t + 1 \tag{5.50}$$

    $$\gamma_{t+1} = \gamma_t \lambda_{\nu_t} \tag{5.51}$$

    $$\rho_{t+1} = \rho_t - \gamma \sum_{i=m_t}^{\nu_t-1} \lambda_i \sigma_{l_t-1,i+1} \tag{5.52}$$

The resulting set of indices $\{\nu_1, \ldots, \nu_n\}$ will then determine the sites that fail. Since each index takes $\mathcal{O}(N)$ time to search through the list of partial sums, the total time is $\mathcal{O}(Nn)$, with usual worst case time being $\mathcal{O}(N^2)$, as many sites can fail at high temperatures

This algorithm, and the extension to the case where interactions are taken into account, allow us to simulate creep at finite temperatures $T > 0$, rather than constraining ourselves to the case $T \to 0$ [180], which has long been a problem with the simulations of creep. As an example, brute force simulation of creep, as well as our method, are shown below in fig. 5.3.

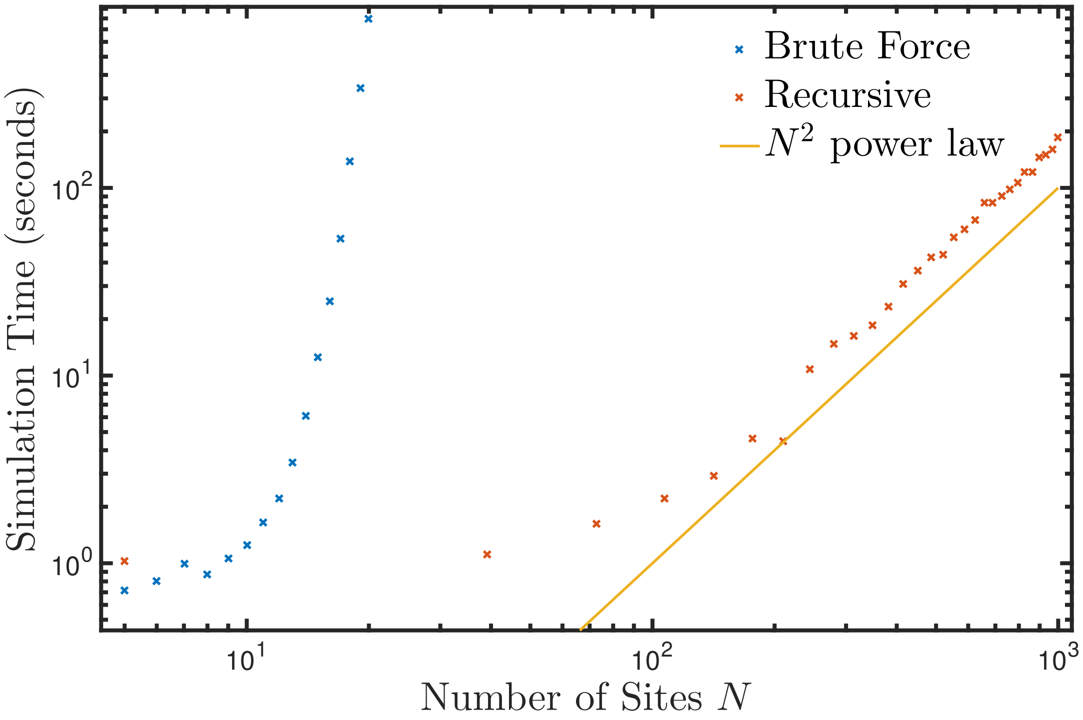

Figure 5.3: The time complexity of creep simulation as a function of the number of sites N. The blue dots represent the brute force method, where each combination is manually computed. Our method is shown in red. We also plot the N^2 relation, showing that our algorithm scales well as N increases, as opposed to the exponential scaling of the brute force method.

In the next chapter, we will use this algorithm, along with previous results from chapter 4, to derive the interevent time distribution at various temperatures.

Chapter 6

Simulation and Analytic Results for the Interevent Time Distribution During Creep

6.1 Introduction

Experiments in steady state creep often involve macroscopic measurements of time dependence of strain as a function of temperature, load, or material variables such as composition [86, 146, 134, 186, 42, 87, 187, 89]. More precise experiments have resulted in the extraction of avalanche-like behavior during creep deformation [88]. In these experiments, a threshold strain (of 15 nm) is set, and a machine is used to measure the strain increase of a material under load. When the next threshold strain is reached, the approximate interevent time (waiting time) distribution between original strain and the next threshold can be extracted in the steady state regime [88] at various stresses and temperatures [90] (see fig. 6.1 for an intuitive picture of interevent times). This interevent time distribution can be computed using the mean field model [13] introduced to study the plastic deformation of materials. We derive a proposed analytic form for this distribution in different regimes, and compare to experiments below. The one important assumption we make is that the energy exponent eq. 4.6 $\gamma = 2$. Other promising studies of dislocation mediated creep in crystalline materials has been performed using acoustic emission to study slip avalanches during creep motion of ice [23, 24]. Unfortunately, these studies do not report the time between events.

Although interevent time studies are not new, often the conditions under which they are obtained preclude them from study in this chapter. Two such studies are the interevent time between events in stressed paper [188] and porous sandstone [189]. For paper, the creep measurements involved an increasing stress on the paper, so that the stress was not constant. For porous sandstone, creep is thought reflect the collapse of weakly bound grains [189] resulting from the slow viscous flow of the material, rather than from discrete thermal activation. In our model, we assume the following:

1. At zero temperature, a slowly increasing (stress or strain) driven plastic deformation of the material occurs in avalanches, whose statics and dynamics are well described by mean field theory [13].

2. During the creep situation modeled here, the stress on the material is constant, and near the failure

stress of the material.

3. Creep is due to thermal activation, and the temperature is low enough that the interevent time is larger than all other time scales, including the avalanche durations. We denote the temperature at which other time scales reach the interevent time scale as T_f.

In the paper-fracture study [188] assumption 2 is invalid, since the stress is not constant, and in the porous sandstone study [189] assumption 3 is invalid since creep is thought to be due to viscous flow of the material. We will first discuss the model results and then discuss how experimental creep tests that fullfill the above three assumptions can be implemented.

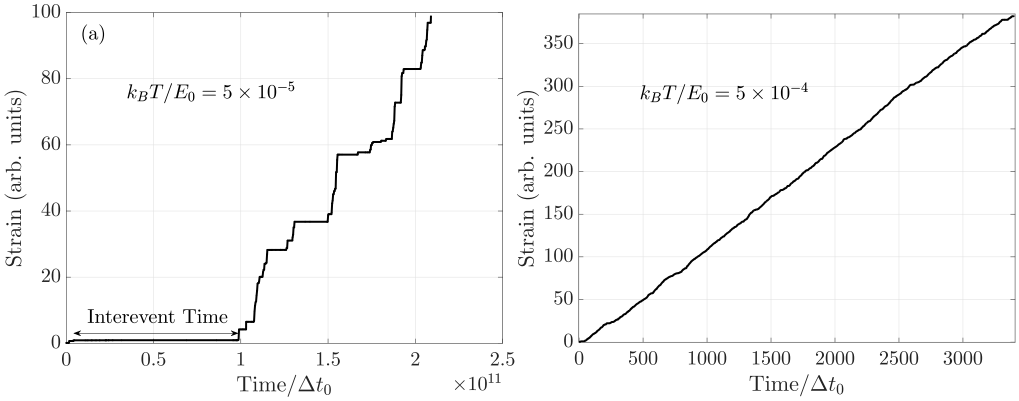

Figure 6.1: The strain vs. time at different temperatures. T is the temperature and E_0 is the energy needed to excite a weak spot, as defined below. We have observed through simulations that there are distinct regimes, which we call the low and high temperature regimes. (a) The low temperature regime. We show a schematic of an interevent (waiting) time between two events. In the low temperature regime the strain curve is composed of large intermittent jumps followed by long quiet periods. (b) The analogous curve in the high temperature regime. The curve is composed of much smaller, more frequent jumps, and the interevent times are much shorter. The difference in scales is dramatic, and a result of the fact that the temperature is 10× lower in (a) than in (b). The advantage of the KMC algorithm is the time scale is found indirectly through the use of eq. 5.16 rather than direct simulation, which would be prohibitively long in simulating (a).

A simulated example of strain curves is shown in Fig. 6.1. In Fig. 6.1a, the strain curve is obtained for low temperatures, which shows jumps are followed by long interevent times. Fig. 6.1b shows the strain curve for high temperatures, where jumps followed by short interevent times. The notion of low and high temperature will be made precise below.

6.2 Analytic Results

Recalling the mean field model presented in chapter 4, the stress on the system

$$s_i = J(u_i - \bar{u}) + \Sigma, \tag{6.1}$$

and the mean stress is $\bar{s} = \Sigma$. When site i fails ($s_i > s_f$), the reduction in stress of site i, $\delta s_i = s_{a,i} - s_f$, is compensated in an increase in stress $\delta s_j = (s_f - s_{a,i})/(N-1)$ for all other sites. This is the mechanism by which slip avalanches are generated in the model. The scaling of the energy barrier as a function of stress is given by

$$\Delta E = \Omega(s_f - s)^{\gamma}. \tag{6.2}$$

Physically, the $\gamma = 2$ exponent is the result of a cusped pinning potential [11, 166], which has long been proposed to play an important role in avalanches in mean field theory [10]. To simulate the thermal activation, we use the kinetic monte carlo (KMC) algorithm [170, 177]. We make a simplifying assumption that between avalanches, a site remains at a fixed stress, and either slips because it is thermally activated or due to an avalanche. The transition rates correspond to activation events, so that either a given site fails or it remains at its current stress. The rates of each site failing are proportional to $k_i = \lambda_0 \exp(-\Delta E/k_B T) = \lambda_0 \lambda_i$ like in eq. 5.25. Recalling that the total transition rate is the sum over all such failure events eq. 5.21

$$r_{\mathbf{s}_\mu} = \sum_{m=1}^{N-1} \sum_{1=i_1<i_2<\ldots<i_m}^{N} k_{i_1,i_2,\ldots,i_m}, \tag{6.3}$$

where $k_{i_1,\ldots,i_m} = \lambda_0 \lambda_{i_1} \ldots \lambda_{i_m}$ we use our modified KMC algorithm to take into account these combinations. The KMC algorithm used here allows for multiple simultaneous activations and then allows for an avalanche to develop following the zero temperature algorithm [7]. On the other hand, the KMC algorithm neglects backwards motion (motion opposite the direction of force), which has vanishingly small probability for Σ near Σ_c. Physically eq. 6.3 calculates a total transition rate $r_{\mathbf{s}_\mu}$ by taking into account all transition paths. Transition paths with large barriers are exponentially suppressed. As more transition paths with small barriers become available, the total transition rate grows. Eq. 6.3 is the key equation that we will have to estimate to arrive at analytic results.

We use the algorithm described in the previous chapter to model creep with N sites to simulate, resulting in $2^N - 2$ transitions. Here we use these simulations to verify our analytic derivations. Results in Fig. 6.3 and Fig. 6.5 show the interevent time distributions at different temperatures for a fixed stress $\Sigma = 0.98 \times \Sigma_c$, where Σ_c is the failure stress. The solid lines in Fig. 6.3 and Fig. 6.5 show the analytic forms derived below, while the markers show simulated results.

To derive analytic distributions for the interevent time, we approximate eq. 6.3. At low temperatures, all multiple activations are suppressed, so that only $m = 1$ activations are valid. In fact, in the low temperature regime, we will consider only the smallest activation barrier to be thermally active. In the low tempeature regime, the material has essentially one transition path between metastable states. This is the transition path with the smallest energy barrier, so eq. 6.3 is well approximated by

$$r_{\mathbf{s}_\mu}(s_m) \approx \lambda_0 \exp(-\Delta E_{min}/k_BT) = \lambda_0 \exp(-\Omega(s_f - s_m)^2/k_BT), \tag{6.4}$$

where s_m is the maximum stress among the sites, and we have used the energy barrier scaling eq. 6.2.

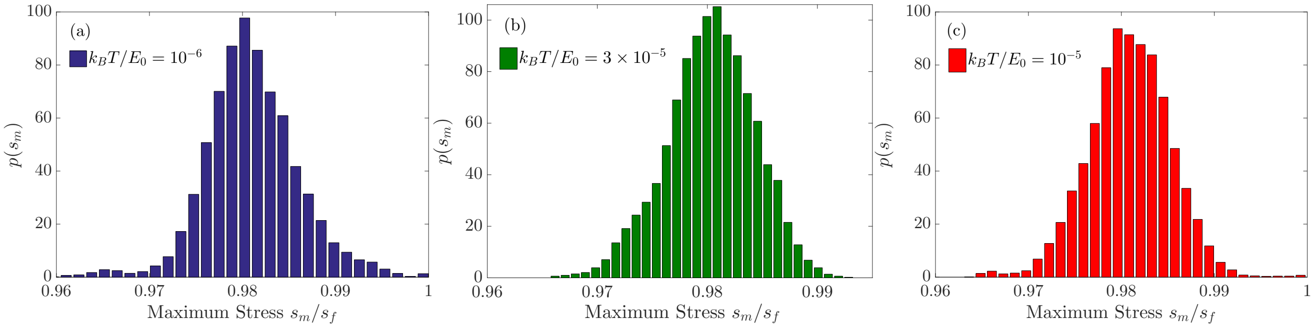

Figure 6.2: The distribution of maximum stresses for 3 different temperatures at fixed force $\Sigma = 0.98 \times \Sigma_c$, number $N = 1000$, and width of arrest stresses $W = 0.1 \times \Sigma_c$. The total number of time steps is 10^4, which does not include the time steps required to forget initial conditions. We set the total number of time steps to forget initial conditions as 2000 time steps. The distribution is Gaussian in the limit $N \to \infty$, and clearly not an extreme value distribution (which for a uniform distribution is exponential [190]). The reason for this is that each step is not independent of the steps before it. The temperature k_BT is defined relative to E_0. We define E_0 below, with $E_0 = \Omega s_f^2$, where s_f is the failure stress. The mean value of this distribution is approximately $0.98 \times s_f$ as seen by the graphs, where the factor of 0.98 is the same as the $\Sigma/\Sigma_c = 0.98$.

The distribution of maximum stress is plotted in fig. 6.2, and it is easier to understand this distribution rather than the distribution of minimum energy barriers. The maximum stress after many failure events will be approximately normally distributed. This arises from the central limit theorem, because maximum stress at any time is the sum of many random small stress increases from past sites that have slipped. We show this more clearly in the appendices, and we derive the properties of this normal distribution. Note that the distribution is not an extreme value distribution [84]. This is because the maximum stress is not independent of stresses from previous iterations. Another important feature seen in fig. 6.2 is that the width of the maximum stress distribution is roughly independent of temperature for low temperatures.

For each given rate $r_{\mathbf{s}_\mu}$, the interevent time Δt is exponentially distributed by eq. 5.16. The interevent times are defined as the times between the activation events, and found directly from the KMC algorithm. The reason that the full distribution of interevent times is not itself exponential is that the rates $r_{\mathbf{s}_\mu}$ themselves are random. Therefore the distribution of Δt given $r_{\mathbf{s}_\mu}$, $p(\Delta t|r_{\mathbf{s}_\mu}) = r_{\mathbf{s}_\mu} e^{-r_{\mathbf{s}_\mu}\Delta t}$. Given a probability distribution $p(r_{\mathbf{s}_\mu})$ for the rate constant $r_{\mathbf{s}_\mu}$, we can express the distribution of interevent times as

$$p(\Delta t) = \int dr_{\mathbf{s}_\mu} p(r_{\mathbf{s}_\mu}) p(\Delta t|r_{\mathbf{s}_\mu}) \tag{6.5}$$

$$p(\Delta t) = \int dr_{\mathbf{s}_\mu} p(r_{\mathbf{s}_\mu}) r_{\mathbf{s}_\mu} e^{-r_{\mathbf{s}_\mu}\Delta t} \tag{6.6}$$

$$= \int ds_m p(s_m) r_{\mathbf{s}_\mu}(s_m) e^{-r_{\mathbf{s}_\mu}(s_m)\Delta t} \tag{6.7}$$

where we have used that $p(r_{\mathbf{s}_\mu}) dr_{\mathbf{s}_\mu} = p(s_m) ds_m$ by changing variables in the integration. This substitution is valid because we are changing variables in a probability distribution. Here $p(s_m)$ is the probability distribution of the maximum stress. Note that this is similar to several approaches taken for short range theories [84], except we do not assume that s_m follows an extreme value distribution [84]. As stated above, we assume s_m is normally distributed with mean μ and variance σ^2. We make this assumption based on empirical evidence (fig. 6.2) and through arguments in the appendix to this chapter. The essence of this argument is that since each site is connected to every other site (i.e. the main assumption of mean field theory), the maximum value of the stress at any given time is not an independent of the stress distribution at previous times. Extreme value distributions rely on the assumption that the maximum value at any time is a independent of the stress distribution at previous times [190], so it is not an extreme value distribution. Rather, one has a situation in which the maximum value is the result of many small nudges from previous slip avalanches, and hence by the central limit theorem should converge to a normal distribution

$$p(s_m) = \frac{1}{\sqrt{2\pi\sigma^2}} \exp(-(s_m - \mu)^2/2\sigma^2). \tag{6.8}$$

Then plugging in the approximation to $r_{\mathbf{s}_\mu}(s_m)$ eq. 6.4 and distribution of maximum stresses eq. 6.8 into eq. 6.7

$$p(\Delta t) \propto \int_0^{s_f} ds_m e^{-\frac{(s_m-\mu)^2}{2\sigma^2} - \frac{\Omega(s_f - s_m)^2}{k_B T} - \lambda_0 \Delta t e^{-\frac{\Omega(s_f-s_m)^2}{k_B T}}}. \tag{6.9}$$

In chapter 4, we we showed that $s_f \approx 2\Sigma_c$. In the appendices, we show that $\mu \approx 2\Sigma$, and $\sigma^2 \approx \epsilon s_f W/N$, where $\epsilon \approx 1/8$ for uniformly distributed arrest stresses. The integral eq. 6.9 cannot be performed analytically, but saddle point analysis can be used to evaluate the integral. We define $\gamma = k_B T/(2\Omega\sigma^2)$ and $\Delta f =$

$2\sqrt{\Omega}(\Sigma_c - \Sigma)/\sqrt{k_B T}$. Then the integral results in:

$$p(\Delta t) \sim \frac{1}{\Delta t_0} \left(\frac{\Delta t_0}{\Delta t} \right)^{1+\gamma} e^{\gamma \Delta f \left(2\sqrt{\log\left(\frac{\Delta t}{(\gamma+1)\Delta t_0} \right)} - \Delta f \right)} \tag{6.10}$$

with details given in the appendix to chapter 6. The result eq. 6.10 is interpreted below in several different limits.

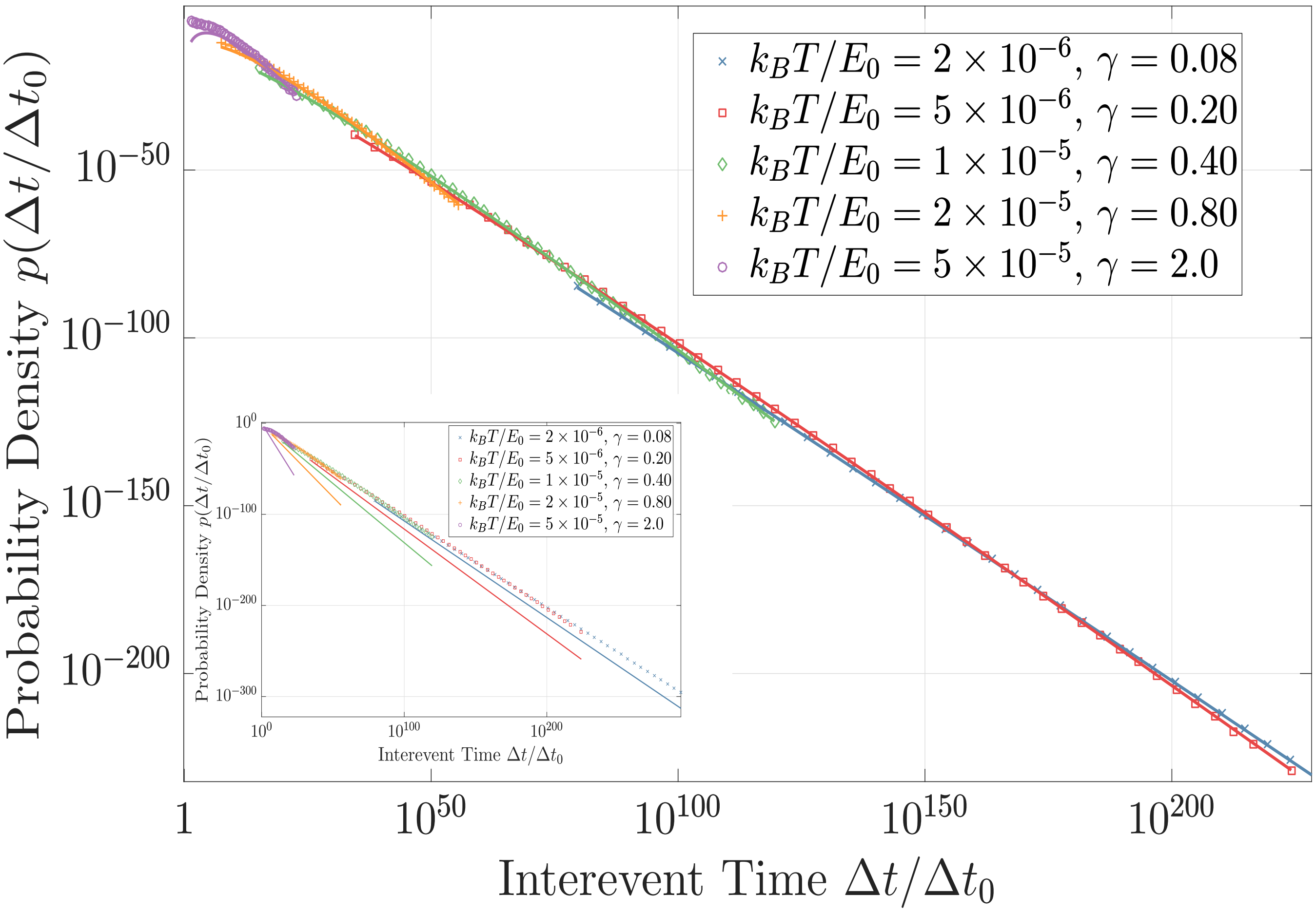

Figure 6.3: The analytic comparison to the theoretical distribution eq. 6.10. The solid lines represent the analytic distribution, while markers represent binned values of the probability distribution from simulations. The force was set at $0.98 \times \Sigma_c$, where Σ_c is the critical force, with $100,000$ interevent times recorded at each temperature and $N = 1,000$ cells. The width of the arrest stress distribution is $W = 0.1 \times \Sigma_c$. In the inset we show the same set of temperatures without taking into account the exponential term in equation 6.10, which results in a power law that is very different from the simulated interevent distributions. We do this to show that the exponential term in eq. 6.10 is very important to the shape of the distribution, and renders it different from the pure power law derived for short range forces [84], which had no subleading terms. As the coefficient $\gamma = 4NT\Sigma_c/(WE_0)$ increases, the exponential in equation 6.10 becomes more important, and changes the shape of the distribution. Therefore it is necessary to include this term in the interevent time distribution. For temperatures greater than $k_BT/E_0 = 5 \times 10^{-5}$, equation 6.15 better describes the distribution of interevent times. This is the result of multiple activation pathways that invalidate using the rate approximation assumption eq. 6.4, which assumes that the site with maximum stress is the site that fails.

In the limit of small γ, corresponding to small $k_B T \ll 2\Omega\sigma^2$, eq. 6.10 simplifies to $p(\Delta t) \sim \Delta t^{-1-\gamma}$. This power law has been derived before for short range disorder [84], where a similar power law was shown with an exponent proportional to $k_B T$. Our result deviates because of the second exponential term that multiplies the power law in eq. 6.10, which causes changes in temperature to manifest in a much weaker fashion than a pure power law (see fig. 6.3). Define an energy scale $E_0 = \Omega s_f^2$. This energy corresponds to exciting a cell from the zero stress to the failure stress in eq. 6.2. Then (see appendices for details)

$$\gamma = NTF_c/(2\epsilon W E_0). \tag{6.11}$$

again, with $\epsilon = 1/8$ for the uniformly distributed arrest stress. In the limit $\Delta f \to 0$ (too close to the failure stress), our assumption 3 is violated, as avalanche durations diverge and are no longer shorter than interevent times. For $N \to \infty$, at fixed temperature, assumption 3 is also violated as there will always be sites near enough to failure to shorten the interevent time until only continuous flow is possible. This physical problem can be circumvented by taking $T \to 0$ as $N \to \infty$ for the appropriate function of N. In fact, looking at the form of γ, we can take $T^{-1} \sim N$ to keep γ constant.

The comparison between the analytic form eq. 6.10 and the simulation results is shown in Fig. 6.3. The symbols represent simulated data, while the solid lines represent analytic predictions. As temperature increases, interevent times become shorter. Physically the disorder prevents the system from jumping from one metastable state to another and therefore longer interevent times are observed. For small disorder $W/F_c \to 0$, at fixed temperature $T > 0$ and fixed N, the exponent $\gamma \to \infty$. In this case, the Gaussian maximum stress distribution in eq. 6.9 becomes sharply peaked, so we approximate it by a delta function $p(s_m) = \delta(s_m - \mu)$. From this we get plugging into eq. 6.7

$$p(\Delta t) \propto \int_0^{s_f} ds_m \delta(s_m - \mu) e^{-\frac{\Omega(s_f - s_m)^2}{k_B T} - \lambda_0 \Delta t e^{-\frac{\Omega(s_f - s_m)^2}{k_B T}}} \tag{6.12}$$

$$p(\Delta t) = \bar{\lambda} \exp(-\overline{r_{\mathbf{s}_\mu}} \Delta t), \tag{6.13}$$

where $\overline{r_{\mathbf{s}_\mu}} = \lambda_0 \exp(-\Omega(s_f - \mu)^2/k_B T)$ is most likely value of the rate constant. This is expected, since in a system without disorder only the force Σ can set how long an activation event will take (i.e. the distribution of maximum stresses of fig. 6.2 is 0), and this leads to a highly peaked distribution of rate constants. In the opposite direction, as W grows, we have an almost pure Δt^{-1} power law for fixed N and T. The contrast of these two regimes shows that without disorder, the system exhibits narrow interevent times, while for a system with large amounts of disorder this distribution widens dramatically.

In deriving eq. 6.10, we have assumed in eq. 6.4 that only the smallest energy barrier will play a role. This is true at low temperature, when all other excitations are exponentially suppressed by an amount $\exp(-(\Delta E - \Delta E_{min})/k_B T)$. As temperature increases this is no longer true. If we order $\Delta E_{min} = \Delta E_0 < \Delta E_1 < \ldots < \Delta E_{N-1}$, then when $k_B T > \langle \Delta E_1 - \Delta E_0 \rangle$ the second energy barrier will also contribute. Letting $\Delta E_n = \Omega(s_f - s_{i(n)})^2$, where $i(n)$ is the site that has the nth largest energy barrier, we have $\langle \Delta E_1 - \Delta E_0 \rangle = \Omega \langle 2 s_f (s_{i(0)} - s_{i(1)}) + s_{i(1)}^2 - s_{i(0)}^2 \rangle$. In the supplementary material [191], we show that $2\langle s_f (s_{i(0)} - s_{i(1)}) \rangle = 8\Sigma_c \Sigma / N$ and $\langle s_{i(1)}^2 - s_{i(0)}^2 \rangle = -8\Sigma^2/N + \mathcal{O}(1/N^2)$. Therefore $\langle \Delta E_1 - \Delta E_0 \rangle = 8\Omega\Sigma(\Sigma_c - \Sigma)/N$. When $k_B T > 8\Omega F(\Sigma_c - \Sigma)/N$, the system enters the high temperature regime. As either Σ approaches Σ_c or N increases, the difference between energy barrier and the next largest energy barrier decreases rapidly. This is true for a two reasons. First, Σ is the mean stress of the system in mean field theory, so even for fixed N, two stresses, say $s_{i(0)}$ and $s_{i(1)}$, are piled up near the failure stress s_f since the stresses must increase as a whole if the mean increases. Note that the stresses cannot exceed the failure stress, as that would result in an avalanche immediately. Second, for fixed Σ, larger N means a larger density of stresses, decreasing the overall energy spacing.

Physically, in the high temperature regime, there is more than one transition pathway for the material to creep along between metastable states. Therefore, the interevent time distribution is a sum of several exponentials of energy barriers in eq. 6.3. Each energy barrier can be written in terms of stress, so that $\Delta E_n = \Omega(s_f^2 - 2 s_f s_{i(n)} + s_{i(n)}^2)$. Each $s_{i(n)} = \mu_n + \sigma\xi$ [191], where $\mu_n \approx 2\Sigma(N-n)/N$, $\sigma^2 \propto 1/N$ as above, and ξ a normally distributed random variable with mean 0 and variance 1, for the same reasons that we argue that $s_{i(0)} = s_m$ is normally distributed. The nth largest stress (for $n \ll N$) is the sum of many iterations of avalanches with randomized stress redistribution $J(s_f - s_{a,i})/(N-1)$ as mentioned above, and can therefore be approximated as a normal distribution. We can neglect the quadratic term in $s_{i(n)}^2 = \mu_n^2 + 2\sigma\mu_n\xi + \sigma^2\xi^2$, since $\sigma^2\xi^2 \sim \mathcal{O}(1/N)$. Then each energy barrier is also a normally distributed variable as we neglect the ξ^2. Therefore, exponentials of energy barriers are lognormally distributed. The sum of lognormal variables can be well approximated by a lognormal variable [192], so the total transition rate is $\lambda_s(\tilde{E}) = \exp\left(-\Delta\tilde{E}/T\right)$. $\Delta\tilde{E}$ is an effective energy barrier, taking into account the different transition paths available to the material. The effective energy barrier $\Delta\tilde{E}$ will be normally distributed with mean μ_E and variance σ_E^2.

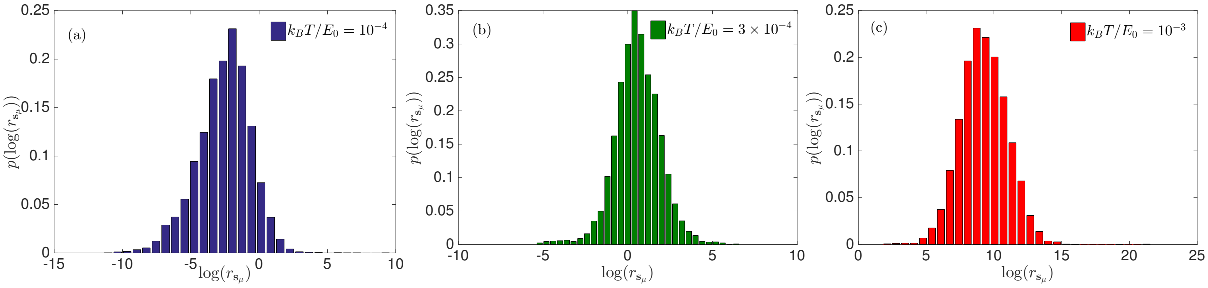

Figure 6.4: The distribution of $\log(r_{\mathbf{s}_\mu})$ at different temperatures. Here $r_{\mathbf{s}_\mu}$ is the rate constant defined in eq. 6.3. Clearly as the temperature increases, the mean value of the distribution also increases. The distribution is sharply peaked and well-modeled by a Gaussian distribution with mean μ_E/T and variance σ_E/T.

The mean and variance of this effective energy barrier are difficult to calculate analytically. However, the form of the interevent time distribution can be found. The integration in the high temperature case is similar to the low temperature calculation. The integral is

$$\begin{aligned} p(\Delta t) &= \int d(\Delta\tilde{E}) p(\Delta\tilde{E}) \lambda_s(\Delta\tilde{E}) e^{-\lambda_s(\Delta\tilde{E})\Delta t} \\ &= \frac{1}{\sqrt{2\pi\sigma_E^2}} \int d(\Delta\tilde{E}) e^{-(\Delta\tilde{E}-\mu_E)^2/\sigma_E^2 - \Delta\tilde{E}/T - \Delta t e^{-\Delta\tilde{E}/T}}. \end{aligned} \tag{6.14}$$

This integral is again intractable, but the saddle point equation can be solved exactly in this case yielding

$$p(\Delta t) = \frac{e^{-\frac{\mu_E}{T}+\frac{\sigma_E^2}{2T^2}}}{\Delta t_0\sqrt{1+W(z)}} \left(\frac{W(z)}{z}\right)^{T^2/\sigma_E^2} e^{-\frac{T^2}{2\sigma_E^2}W(z)^2}. \tag{6.15}$$

Here $W(z)$ is the Lambert-W function and $z = \Delta t/\Delta t_0 \exp(-\mu_E/T + \sigma_E^2/T^2)\sigma_E^2/T^2$. The calculations are detailed in the supplementary material [191]. This high temperature distribution function is displayed for different temperatures (within the high temperature regime) in Fig. 6.5.

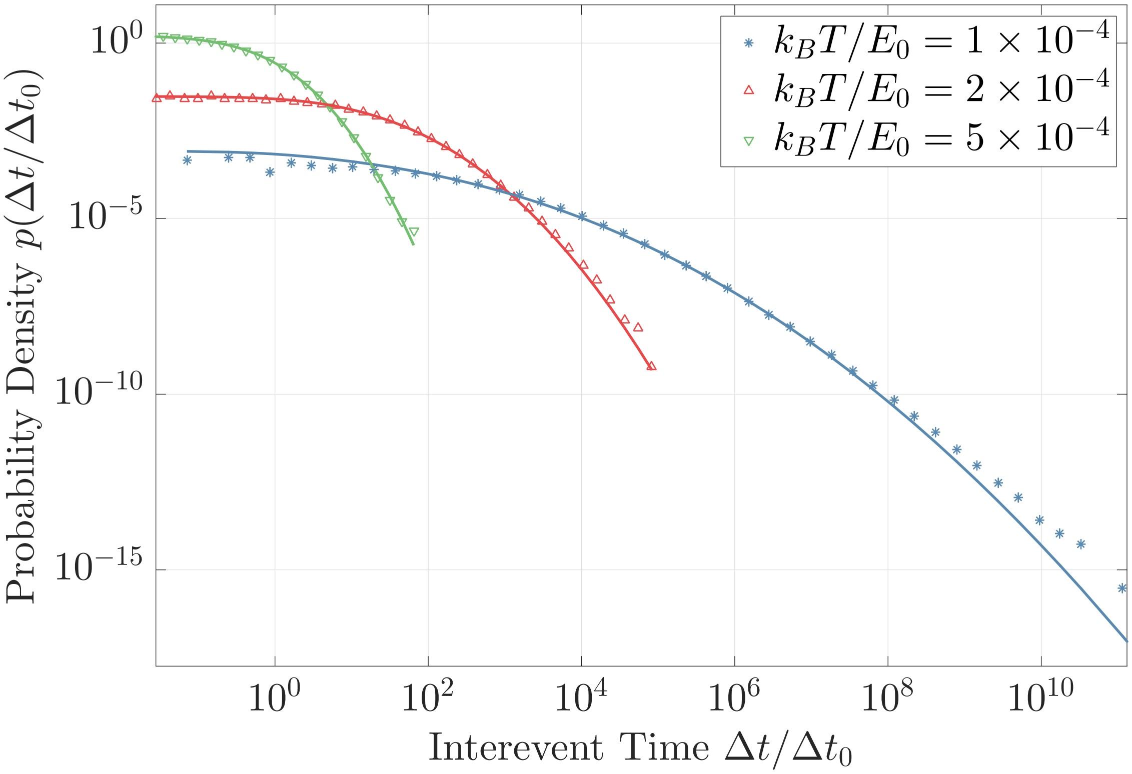

Figure 6.5: Comparing analytics with simulations; the higher temperature approximation to the interevent time distribution. T is the temperature and E_0 is the energy required to excite a weak spot from arrest to failure. The units are the same as in Fig. 6.3, with the same simulation parameters. The solid lines represent the analytic distribution equation 6.15, while markers represent binned values of the probability distribution from simulations. We see here that the interevent times decay much faster, and do not follow a power law.

In Fig. 6.5 we show interevent time distributions (as the symbols) along with the analytic predictions (as the solid lines) in the high temperature regime. The variance and mean were found from the simulation directly, by finding the mean and variance of simulated effective energy barriers $\Delta\tilde{E} = -T\log(\lambda_s)$. The same simulation parameters used in the low temperature regime were used in producing Fig. 6.5, except the temperature was higher.

Most current experiments cannot resolve a single interevent time, as the strain signal from a single slip avalanche is usually below the noise threshold. In [88, 90], the interevent times were instead reported as the times for the strain to increase by a fixed amount (15 nm in these measurements). In Fig. 6.6 we show the interevent times at a fixed low temperature after setting different minimum thresholds for the strain measured. We express this minimum threshold as the average number of avalanches required to traverse the minimum threshold $\langle M\rangle$, which is well defined for fixed Σ, T, and N. We do this by recording the individual strain increases and summing the motion of the shear band until it reaches the next fixed strain amount. The total interevent time is $\Delta t_M = \sum_{i=1}^{M} \Delta t_i$. Independent of $\langle M \rangle$, the distribution $p(\Delta t_{\langle M \rangle})$ is roughly the same, with the only difference being the minimum value of the distribution $p(\Delta t_{\langle M \rangle})$. Heuristically, the reason the distribution is invariant to finite sums is that the eq. 6.10 is roughly scale invariant. Concretely this means that $p(\Delta t_{\langle M \rangle}) \approx 1/\langle M \rangle^{\eta} p(\Delta t)$ for large Δt, where η is an exponent describing the approximate scaling behavior. However, note that because of the exponential term in eq. 6.10 the exponent η need not be the same as γ in eq. 6.11. A more detailed version of this argument is presented in the supplementary material [191].

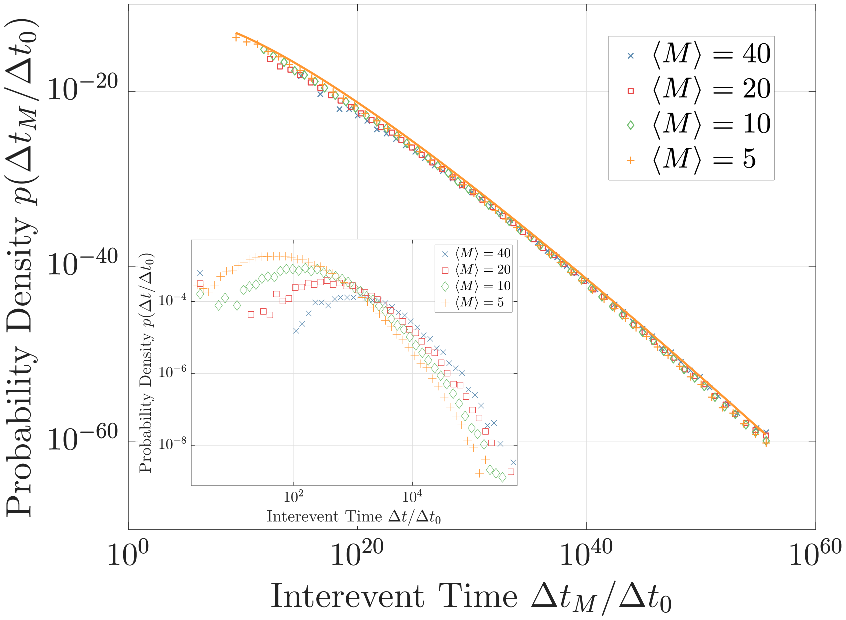

Figure 6.6: Comparing analytics to simulations; the cumulative interevent times are defined as sums of M individual interevent times during which the material has moved by a set distance. The main figure shows the low temperature regime ($k_B T = E_0 \times 10^{-5}$). The solid line shows the analytic prediction at this temperature and force. The inset shows the high temperature regime ($k_B T = E_0 \times 10^{-4}$). We vary the threshold distance proportional to $\langle M \rangle$ to show the invariance of the low temperature distribution to such sums. Conversely, the high temperature regime shows large variance between threshold distances. Therefore, by varying the threshold distance, we can distinguish the two regimes.

The inset of Fig. 6.6 shows the cumulative interevent time in the high temperature regime. We see a qualitatively different type of distribution of interevent times. The distribution is peaked for any appreciable number of mean steps $\langle M \rangle$, and this peak itself depends on the value of $\langle M \rangle$. Therefore, a simple way to distinguish the low and high temperature regimes is to vary the threshold of detection. In the high temperature regime the resulting distribution changes significantly like the inset of Fig. 6.6. In the low temperature regime, only the minimum value of the distribution changes.

Recent bulk-metallic glass experiments using $Pd_{77.5}Cu_6Si_{16.5}$ may satisfy the assumptions [88, 90] in our description of creep. Creep interevent time distributions were found for different stresses and temperatures [90]. These distributions were all close to power laws. In each case, two power laws with exponents of -1.5 and -0.8 were reported, with the crossover interpreted as the formation of a shear band in the metallic glass. We suggest that the -0.8 power law is actually closer to the low temperature distribution eq. 6.10. As shown in Fig. 6.3, the exponential factor in eq. 6.10 tends to decrease the slope on a log-log plot so that it remains close to a -1 slope (the inset of Fig. 6.3 shows what happens with the pure power law). In addition, the experiments have shown that the interevent time distribution does not change appreciably over the small variation of temperature $((0.85 - 0.97) \times T_g)$ [90]. In Fig. 6.3 the temperature needed to be changed by at least a factor of 2 to see an appreciable change in the interevent time distribution.

We propose that interevent times can be measured by both the methods presented in [88, 90] as well as through acoustic emission [193, 24]. In these experiments [193, 24, 88, 90], the material (either ice or bulk metallic glass) is held under a constant stress and it is thought that creep is caused by thermal activation. We expect in the low temperature regime that the distribution can be described by eq. 6.10, with parameters $\gamma \propto k_B T/W$, where W is the spread of disorder in the material, and $\Delta f \propto (\Sigma_c - \Sigma)$. We predict that by varying temperature and stress, it should be possible to observe the predicted variation in interevent time distribution. The value of γ may also be varied by changing the spread of disorder in the material, although this is a very difficult quantity to control in experiments. If it can be extracted from experiments, γ should give information about the amount of disorder present in a material.

Appendix A

Appendix to Chapter 2

A.1 Kepler Data

In this appendix, we show several plots and explain more of the data processing related to the discussion in Chapter 2. The *Kepler* data was provided to us by the Mikulski Archive for Space Telescopes (MAST). The light curve comes as a single processed file known as a single-aperture photometry (SAP) file. The SAP data has many artifacts that are caused by variations extrinsic to the stars monitored by *Kepler*. The data is correct by looking for trends along many different stars and extracting and correcting for these trends. This corrected data is known as the pre-conditioned single aperture photometry (PDC-SAP) data. The PDC-SAP data for all of the stars we used was validated based on the original SAP data as well as pixel-level data, which also shows dimming events of the magnitude seen in the PDC-SAP data [65, 64, 60].

Although the PDC-SAP data was cleaned up significantly compared to the raw data, there were still several steps that needed to be done to clean it up further. First, the data needed to be stitched together. Since *Kepler* orbits the Sun, it occasionally needs to reorient itself to view the patch of space where the stars are located. This process causes minute changes in the point-spread function of the sensors because different sensors are collecting different sets of stars now. The solution is known as stitching, and in order to do it we first used iterative sigma clipping, after which the data was normalized. We normalized to the median value because of the large outliers in KIC 8462852. This lets us string together two discontinuous sets of data.

The second problem was that some of the data was missing. These values needed to be filled in to properly analyze the fourier spectrum. The suggested method to doing this is to interpolate the data, and we chose to linearly interpolate the data since this is what is usually recommended. Linear interpolation was used because it is the simplest of all interpolation kernels. After interpolation, standard filtering was performed on the data. We did not Wiener filter the data [4] because no noise file was available. Using the official *Kepler* photometric noise reported did not improve the processing. No other smoothing was done.

The next, and most involved part, was to filter the rotation signal (the 0.88 day periodicity in KIC

8462852). The rotation signal was filtered in a two step processes. First, all the large avalanches were removed from the light curve. These large avalanches are all drawn in fig. A.1.

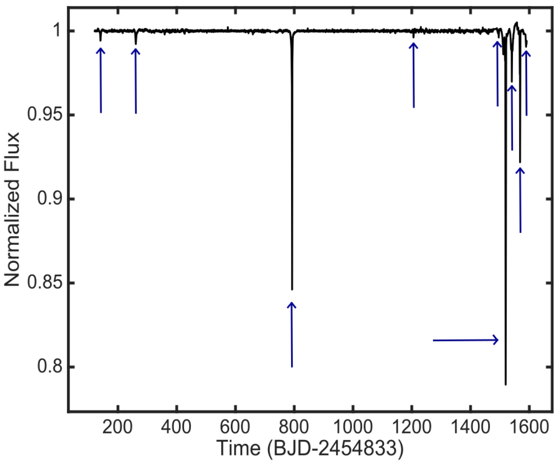

Figure A.1: The light curve of KIC 8462852, with arrows pointing to the dimming events that were removed before filtering. The dimming events were replaced by a constant value that kept the light curve continuous. After filtering, the original large dimming events were once again added in to have a complete, filtered light curve.

In order to remove these avalanches, we sampled the light curve at a very coarse grained scale, and then fit the resulting set of points using cubic splines. Then we subtracted the spline data from the original light curve. The purpose of removing the large avalanches was to prevent spurious ringing, which will occur since many of the large avalanches have frequency components at the filtered frequencies. The resulting data was filtered using a least-squares filter designed by the MATLAB *firls* program. The *firls* program, which stands for finite impulse response least squares, was designed to produce filters which have a frequency profile that fits a desired input profile. In our application, this profile was a band-stop filter [194]. The frequencies we chose were $f_{stop} = 1/\tau_{rot}$, where $\tau_{rot} = 0.88$ days and the two higher harmonics. The stop band had a roll-off frequency of $0.95 f_{stop}$ and a stop band of $0.96 f_{stop}$, as well as a symmetric return to the pass band. The higher harmonics were implemented in the same way. We used the rotation period used for filtering of KIC 8462852 was reported in [60]. Finally, the large avalanches were added in again in order to have a complete, filtered light curve.

For the other stars, we simply used the filter, without removing large events. The rotation periods of KIC 4638884 and KIC 7771282 were reported in [64]. The shortest rotation period of KIC 5955122 [65] was used for the filter of its light curve. The filtering of rotation for these stars was done for consistency in the data processing pipeline.

There were two main advantages to rotation filtering. First, without filtering, rotation dips would be characterized as avalanches, and therefore skew the statistics of the avalanches. Second, before filtering the rotations were visible when analyzing the avalanche shape information. This caused problems for the larger avalanches (on the order of 10^{-3}),), since there were several oscillations during each large avalanche. It also skewed the avalanche durations and sizes in unpredictable ways. However, one draw-back is that by filtering out certain frequencies, we have also biased the data, since legitimate avalanches will also occur at these frequencies. The impact was determined to be negligible since the effects of the filter are localized to a small subset of frequencies.

A.2 Extracting Avalanche Statistics

A.2.1 Exponents

Statistical processing for Tabby's star and the other stars is fairly standard in the field of power law statistical processing [100]. We primarily deviated from the standard method because our distributions are only expected to be power laws over certain ranges, the scaling regime. Therefore, we use the likelihood function described in [195]

$$p(\alpha|x_i) = \prod_{i=1}^{N} \frac{\alpha - 1}{x_{min}} \frac{1}{1 - X^{1-\alpha}} \left(\frac{x_i}{x_{min}} \right)^{-\alpha} . \tag{A.1}$$

Here the x_i are the various points of data, either size or durations of avalanches. Also $X = x_{max}/x_{min}$, the ratio of the range over which the power law is expected to hold. We use this likelihood function to find α, by minimizing the logarithm of this function as a function of α.

In addition to finding the power law exponent, we also used eq. A.1 to find the uncertainties with regard to the exponent. Although the bootstrap method is one way to find uncertainties [100], we found that varying x_{min}, x_{max}, and the threshold was much more reflective of our data. We varied the threshold by 10^{-5} and the values of x_{min} and x_{max} by $\pm 64\%$. These uncertainties were reported in table 2.2. The upper error there is the maximum value of the exponent we extracted, while the lower value is the minimum exponent that we extracted.

A.2.2 Avalanche Shapes and the Scaling Regime

The avalanche shapes were averaged using methods outlined in chapter 2. Avalanches were binned logarithmically, with bin widths of $0.85 - 1.15 \times T_{center}$ or $0.85 - 1.15 \times S_{center}$. The center values were chosen so that no bins overlap, and since it can be presumed that the shapes are roughly independent of each other, the averages in the bins are also independent.

Some amount of filtering was allowed when performing avalanche collapses. For each time point in an average $\langle V(t)|T\rangle$ or $\langle V(t)|S\rangle$, we also had a standard derviation $\sqrt{\mathrm{var}(V(t)|T)}$ and $\sqrt{\mathrm{var}(V(t)|S)}$. The criteria we used for rejecting an averaged shape was that $\max_t \left(\frac{\sqrt{\mathrm{var}(V(t)|T)}}{\langle V(t)|T\rangle}\right) \leq 0.25$. Typically, this meant that we needed approximately 10 or so avalanches before we would use an avalanche average in our scaling collapse. The value of 0.25 was chosen because it allowed us to compromise between selecting bins with many avalanches and choosing enough bins to do good scaling collapses.

Perhaps by accident, we also found a reliable method of estimating the scaling regime in the data. The scaling regime was determined simply by the range over which the avalanches had acceptable size and duration shape collapses, while also maintaining consistency of the exponents. Note that this is really a consistency criteria, since the scaling collapses depend on the exponents, which depend on the scaling regime. We admit that this is a somewhat adhoc criteria, since what acceptable collapse means is not specified, but it is certainly better than simply choosing a scaling regime. A simple improvement over this method would be to select such a criteria systematically, but we did not pursue this any further.

A.3 The Stars KIC 4638884, KIC 7771282, and KIC 5955122

We have now looked through several hundred F class stars, and in the past we focused primarily on magnetically active stars. Several references [64, 65] have already listed out about 22 such stars. We found 3 stars, KIC 4638884, KIC 7771282, and KIC 5955122, conformed to predictions made by the mean field model. In table 2.2, we list the exponents that we extracted for these stars. The scaling regimes for these stars is listed below in table A.1.

Star	Duration Range (days)	Size Range (fraction flux drop * days)
KIC 4638884	$0.11 - 1.71$	$2.1 \times 10^{-6} - 1.6 \times 10^{-4}$
KIC 5955122	$0.13 - 1.06$	$4.8 \times 10^{-6} - 2.6 \times 10^{-4}$
KIC 7771282	$0.16 - 1.44$	$1.7 \times 10^{-6} - 9.1 \times 10^{-5}$
KIC 8462852 (Tabby's star)	$0.18 - 3.33$	$5.1 \times 10^{-6} - 2.4 \times 10^{-3}$

Table A.1: Here we list the scaling regimes found by scaling collapse of either size or duration avalanche shapes. The scaling collapses for KIC 8462852 (denoted with an asterisk) are reported in chapter 2. The scaling collapses for the other three stars are shown below. The scaling regime was found by an iterative process detailed in the supplementary material. Avalanches above or below the scaling regime did not collapse with avalanches in the scaling regime.

Now we list several figures which show the statistics for these stars.

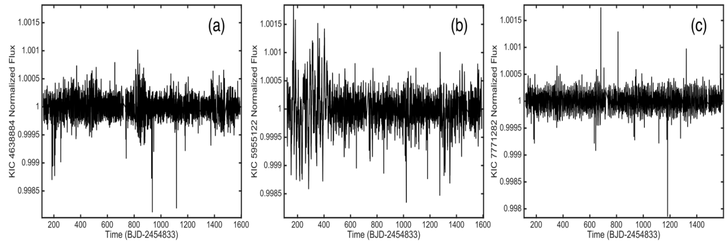

Figure A.2: The light curves of the three stars. (a) The light curve of KIC 4638884. (b) The light curve of KIC 5955122. (c) The light curve of KIC 7771282.

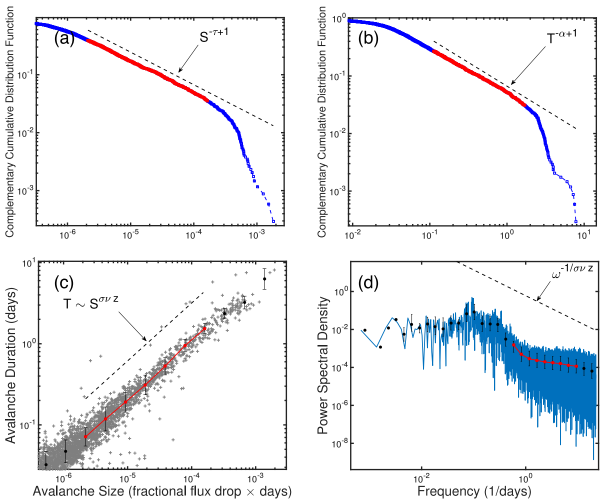

Figure A.3: The statistics of KIC 4638884. The values of the exponents are listed in table 2.2. In figure (a) and (b), the power law statistics of size and duration can be seen in associated CCDFs, with the scaling regimes highlighted in red. The dashed lines in (a) and (b) are the maximum likelihood estimates of the power laws. In figure (c) the related loglog plot of the magnitude vs. duration shows that there is a power law relationship between size and duration, as predicted by theory. The dashed line is the least squares estimate of the slope. For avalanches that are longer than those in the scaling regime defined by the shape collapses, the exponent appears to approach close to the mean field value of 1/2. In (d) we show the power spectral density, and plot the associated power law that the power spectral density is expected to obey. The scaling regime can be found in table A.1.

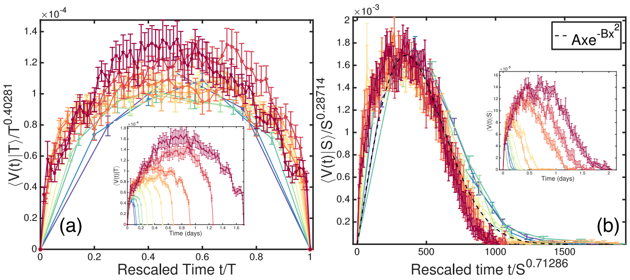

Figure A.4: The avalanche shape collapses for KIC 4638884. The value of $\sigma\nu z$ used for the collapse was the measured value $\sigma\nu z = 0.71$. Values between $0.65 < \sigma\nu z < 0.73$ are also acceptable. (a) The duration collapse. (b) The size collapse.

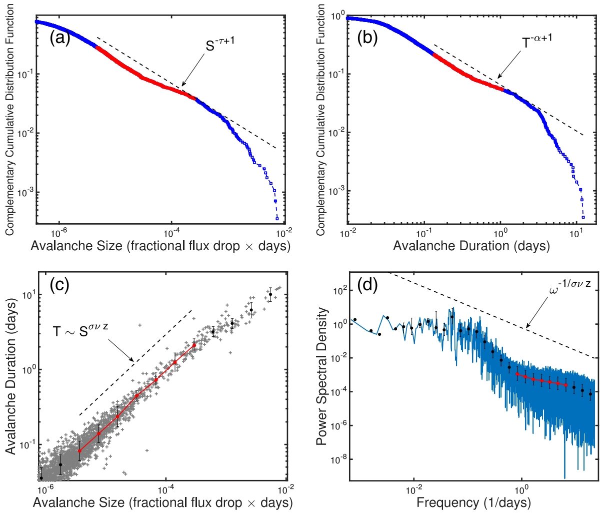

Figure A.5: The statistics of KIC 5955122. The values of the exponents are listed in table 2.2. In figure (a) and (b), the power law statistics of size and duration can be seen in associated CCDFs, with the scaling regimes highlighted in red. The dashed lines in (a) and (b) are the maximum likelihood estimates of the power laws. In figure (c) the related loglog plot of the magnitude vs. duration shows that there is a power law relationship between size and duration, as predicted by theory. The dashed line is the least squares estimate of the slope. For avalanches that are longer than those in the scaling regime defined by the shape collapses, the exponent appears to approach close to the mean field value of 1/2. In (d) we show the power spectral density, and plot the associated power law that the power spectral density is expected to obey. The scaling regime can be found in table A.1.

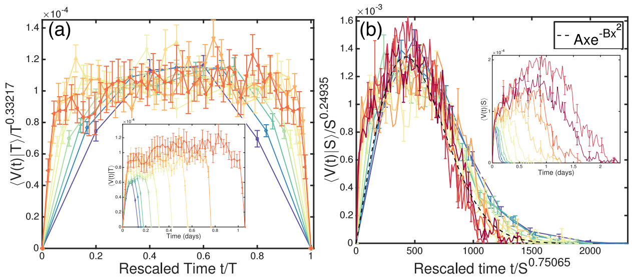

Figure A.6: The avalanche shape collapses for KIC 5955122. The value of $\sigma\nu z$ used for the collapse was the measured value $\sigma\nu z = 0.75$. Values between $0.70 < \sigma\nu z < 0.80$ are also acceptable. (a) The duration collapse. (b) The size collapse.

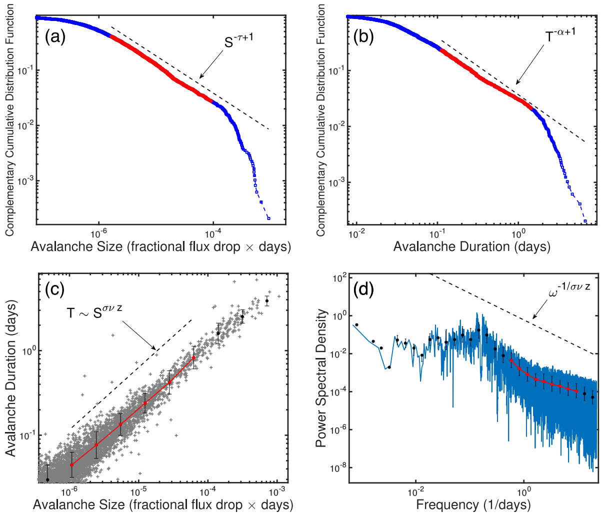

Figure A.7: The statistics of KIC 7771282. The values of the exponents are listed in table 2.2. In figure (a) and (b), the power law statistics of size and duration can be seen in associated CCDFs, with the scaling regimes highlighted in red. The dashed lines in (a) and (b) are the maximum likelihood estimates of the power laws. In figure (c) the related loglog plot of the magnitude vs. duration shows that there is a power law relationship between size and duration, as predicted by theory. The dashed line is the least squares estimate of the slope. For avalanches that are longer than those in the scaling regime defined by the shape collapses, the exponent appears to approach close to the mean field value of 1/2. In (d) we show the power spectral density, and plot the associated power law that the power spectral density is expected to obey. The scaling regime can be found in table A.1.

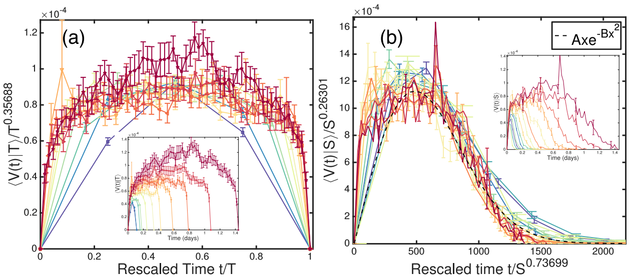

Figure A.8: The avalanche shape collapses for KIC 7771282. The value of $\sigma\nu z$ used for the collapse was the measured value $\sigma\nu z = 0.74$. Values between $0.68 < \sigma\nu z < 0.77$ are also acceptable. (a) The duration collapse. (b) The size collapse.

Appendix B

Appendix to Chapter 3

In this appendix, we show several plots and explain in more detail the data processing related to chapter 3.

B.1 Avalanche Shape Collapses for Regions 2-7

In the following figures, we plot the remaining avalanche shapes and the collapses for both size and duration. The primary purpose of these figures is for completeness. We do not claim that these are acceptable scaling collapses.

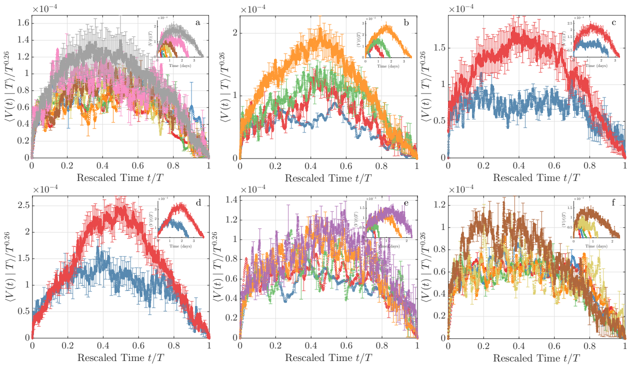

Figure B.1: The avalanche shape collapses for fixed duration for regions 2-7. The shapes are color coded to coincide with the uncollapsed versions in the insets. (a) Region 2. (b) Region 3. (c) Region 4. (d) Region 5. (e) Region 6. (f) Region 7. The shapes were all collapsed using the same exponent $\sigma\nu z = 0.79$. None of the 6 regions shown here produces shape collapses as effectively as the shape collapse shown in fig. 3.3.

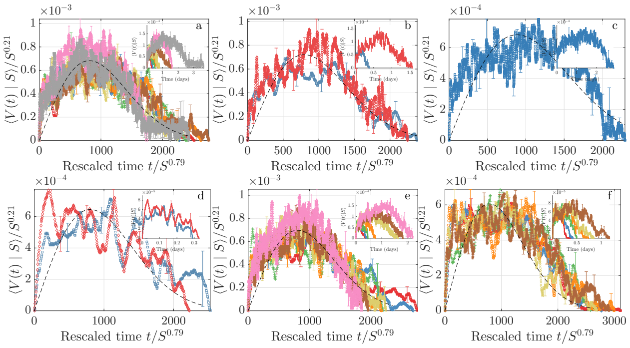

Figure B.2: The avalanche shape collapses for fixed size for regions 2-7. The shapes are color coded to coincide with the uncollapsed versions in the insets. (a) Region 2. (b) Region 3. (c) Region 4. (d) Region 5. (e) Region 6. (f) Region 7. The shapes were all collapsed using the same exponent $\sigma\nu z = 0.79$. None of the 6 regions shown here produces shape collapses as effectively as the shape collapse shown in fig. 3.4.

B.2 Data Preparation Robustness to Threshold Variation

B.2.1 Data Preprocessing and Threshold Variation

One of the major problems with processing the VIRGO data was that we could not use a constant threshold. Therefore we wanted to go into some detail about the data preparation. The data processing pipeline occurred in three steps. We were given access to the raw VIRGO data, not the VIRGO data that has been filtered to remove long term variations. We had to do several filtering steps before we could use the data. We removed bad time points from the light curve $F(t)$, since there were certain times at which the VIRGO instrument did not measure data. We then normalized the VIRGO data $F(t)$ to the mean value (the median or mean produces almost indistinguishable results). This data, $F(t)/F_{mean}$ is then smoothed with a window filter. We chose a time window of 40000 minutes, which is 28 days, because this window will smooth any oscillations that we are interested in. This data can be written as $\bar{F}(t)/F_{mean}$. Then we subtracted the two, resulting in a data set which we call $\bar{V} = (F(t) - \bar{F}(t))/F_{mean}$. Finally, we passed the subtracted data through another filter, to filter out rapid oscillations. This was either a window filter of size 10 minutes, or a Hamming window filter of a roll-off at about 10 minutes. Note that the sampling period is 1 minute. The final result was then used in the data processing.

In order to show that the threshold $\bar{F}/F_{mean}$ does not change the statistics we extracted, we also chose window sizes of 20000 minutes (13 days) in fig. B.3 and 50000 minutes (34 days) in fig. B.4. No huge variations were detected.

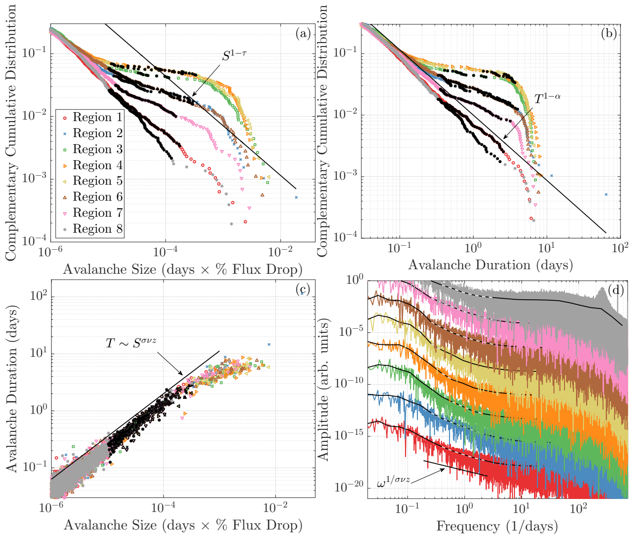

Figure B.3: The dimming event statistics for a threshold found using a smoothing window of 20000 points (13 days). There are no large differences between the overall distribution of sizes and durations versus the original fig. 3.2. (a) The size CCDF. (b) The duration CCDF. (c) The size vs. duration. (d) The PSD.

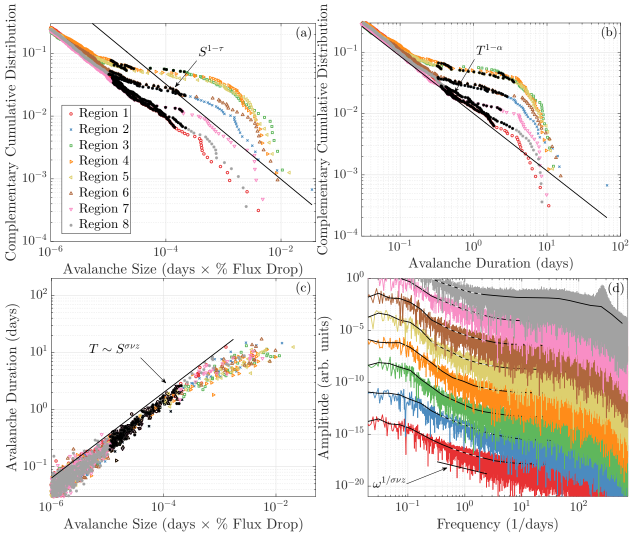

Figure B.4: The dimming event statistics for a threshold found using a smoothing window of 50000 points (34 days). There are no large differences between the overall distribution of sizes and durations versus the original fig. 3.2. (a) The size CCDF. (b) The duration CCDF. (c) The size vs. duration. (d) The PSD.

B.2.2 Extraction of Avalanche Statistics

We used the maximum likelihood method outlined in appendix A.2.1 to find the power law exponents. We also used the exact same methods outlined in appendix A.2.2 to find the shapes.

B.3 Brightening Events

In addition to the dimming events in the VIRGO data, we also took a look at the brightening events, which follow statistics and predictions from the avalanche model [17]. The results are consistent with those of the dimming events. From a purely theoretical point of view, one would expect brightening events that are symmetric with the dimming events. The reason is that the velocity in the mean field model v is analogous to the flux$F$ in the model of stars. In systems where there is a finite velocity ($\Sigma > \Sigma_c$), an avalanche is defined as fluctuations around this velocity. Therefore, if we consider the finite flux as a velocity, we should see brightening variations about this flux that also reflect statistics from the model [17].

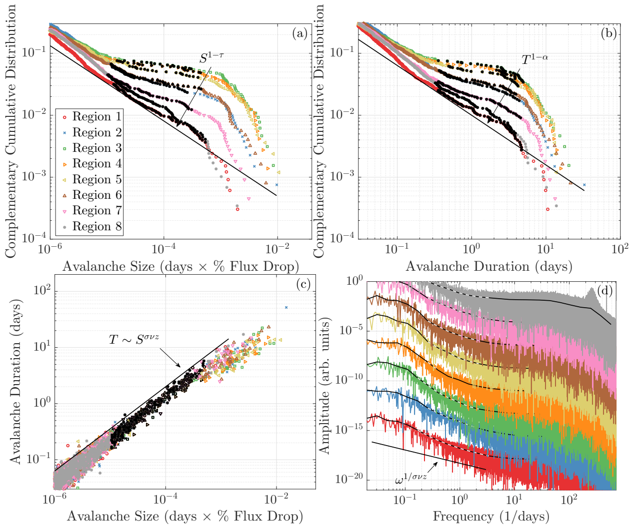

Figure B.5: The brightening statistics that are analogous to the dimming statistics in fig. 3.2. The lines are slopes that have been averaged over the fits from regions 1 and 8. The black markers/highlighting represent the scaling regimes, which are where we obtained avalanches for our collapses. (a) The size CCDF. (b) The duration CCDF. (c) The size vs. duration. (d) The PSD.

Exponent	Region 1	Region 8	Mean Field
τ	$1.83\pm^{0.2}_{0.2}$	$1.66\pm^{0.1}_{0.1}$	3/2
α	$1.95\pm^{0.2}_{0.2}$	$1.90\pm^{0.1}_{0.2}$	2
$\sigma\nu z$	$0.81\pm^{0.03}_{0.03}$	$0.82\pm^{0.03}_{0.03}$	1/2
$\frac{\tau-1}{\alpha-1}$	$0.74\pm^{0.4}_{0.3}$	$0.73\pm^{0.3}_{0.2}$	1/2

Table B.1: Avalanche exponents for regions 1 and 8 for the brightening events, and exponents for the mean field avalanche model [17]. In order to extract the exponents τ and α we used a maximum likelihood approach [100]. The uncertainties obtained from the variation of threshold, the scaling regime, and the two filter windows, which were the highpass filter and filter to determine the threshold (see the appendices). The actual error bars may be larger; the maximum likelihood method we have implemented does not take into account the decaying cutoff function [2].

In fig. B.5, we show the CCDFs, size versus duration, and PSD for the brightening events (the PSD is the same, since it does not depend on a threshold). In table A.1 we show the resulting exponents. Some surprising characteristics that we find are that when the sizes and durations grow larger than a characteristic size/duration (which depends on the region), the distribution transitions from a power-like law to an exponential distribution. This could also be due to the merger of many smaller events.

Next we plot some shape collapses for fixed size and duration.

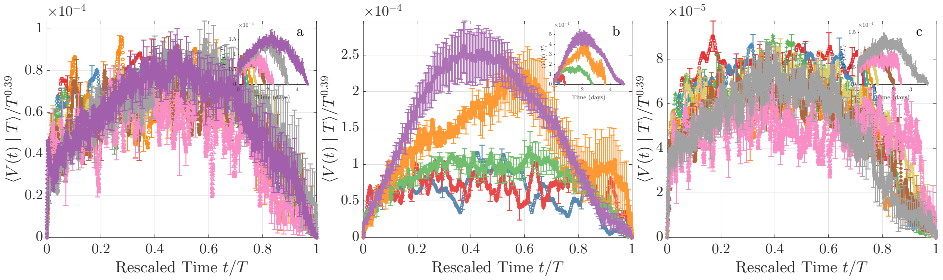

Figure B.6: The brightening shape collapses that are analogous to the dimming shape collapses in fig. 3.3. These are shape collapses at fixed duration. We have included the region 3 collapse in this figure for comparison. (a) The region 1 collapse. (b) The region 3 collapse. (c) The region 8 collapse. The value of $\sigma\nu z$ we used for 0.72.

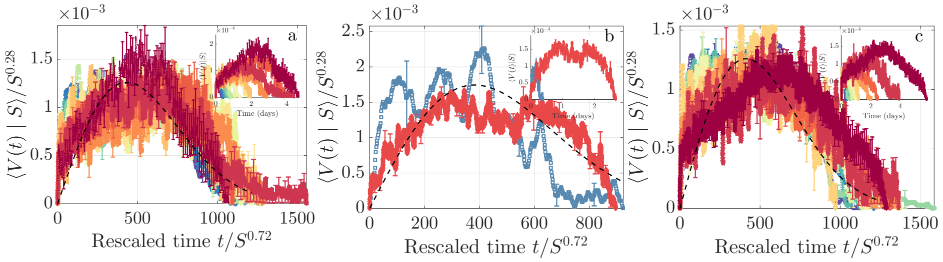

Figure B.7: The brightening shape collapses that are analogous to the dimming shape collapses in fig. 3.4. These are shape collapses at fixed size. We have included the region 3 collapse in this figure for comparison. (a) The region 1 collapse. (b) The region 3 collapse. (c) The region 8 collapse. The value of $\sigma\nu z$ we used for 0.72.

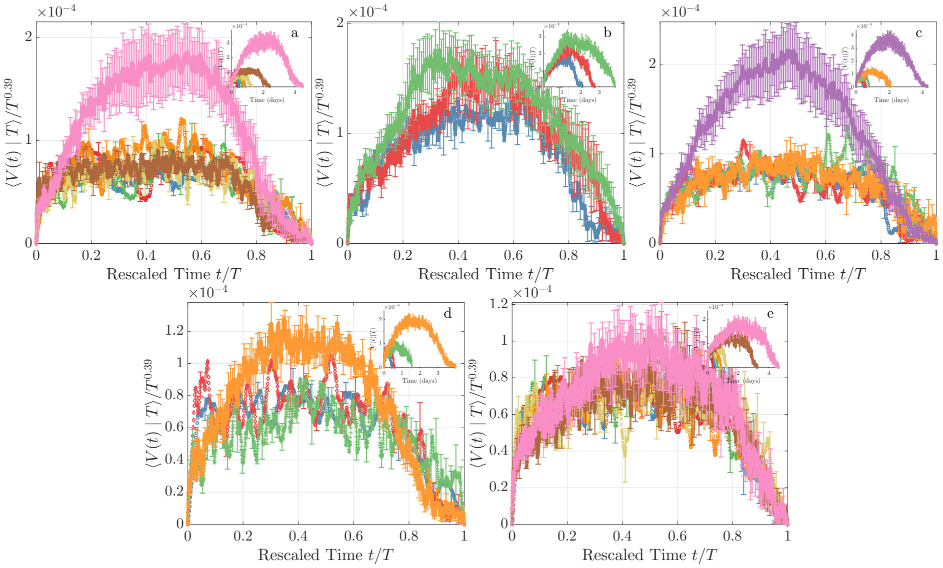

Figure B.8: The brightening shape collapses that are analogous to the dimming shape collapses in fig. B.1. These are shape collapses at fixed duration. We have included the region 3 collapse in this figure for comparison. (a) The region 2 collapse. (b) The region 4 collapse. (c) The region 5 collapse. (d) The region 6 collapse. (e) The region 7 collapse. The value of $\sigma\nu z$ we used for 0.72.

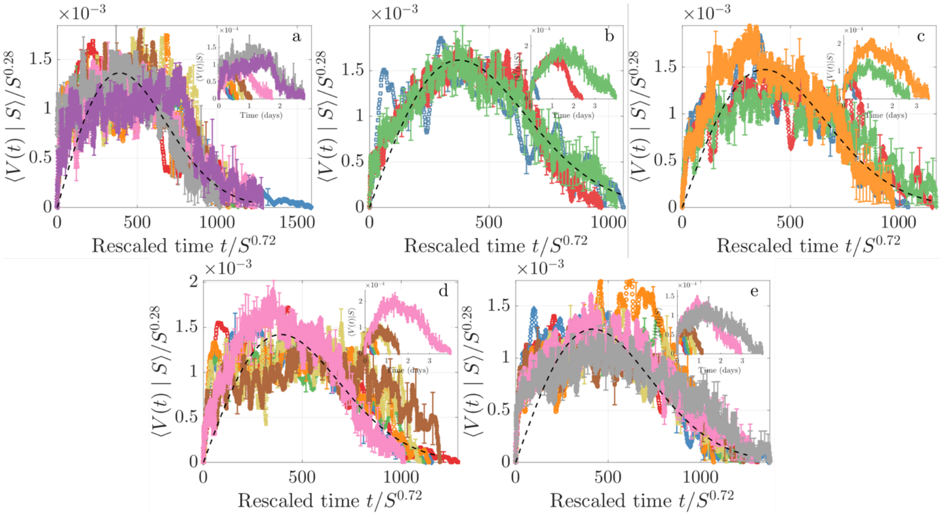

Figure B.9: The brightening shape collapses that are analogous to the dimming shape collapses in fig. B.2. These are shape collapses at fixed size. We have included the region 3 collapse in this figure for comparison. (a) The region 2 collapse. (b) The region 4 collapse. (c) The region 5 collapse. (d) The region 6 collapse. (e) The region 7 collapse. The value of $\sigma\nu z$ we used for 0.72.

We see that in each of these cases, regions 1 and 8 show the best collapses. We hope that this also provides further evidence that near the solar minima, avalanche-like behavior can occur on the Sun's photosphere.

Appendix C

Appendix to Chapter 4

C.1 Response and Correlation Function at Zero Disorder

Much of the analysis in this section is based on [10, 11] and [85]. As a reminder, the action is

$$S = \int d^d x dt i\hat{u}(\mathbf{x},t)\left(\eta \partial_t u(\mathbf{x},t) - \int d^d x' dt' \tilde{J}(\mathbf{x}-\mathbf{x}', t-t')(u(\mathbf{x}',t') - u(\mathbf{x},t)) - \Sigma(\mathbf{x},t)\right) - \frac{1}{2}\int d^d x dt dt' i\hat{u}(\mathbf{x},t) i\hat{u}(\mathbf{x},t')\Delta(u-u') - \eta T \int d^d x dt i\hat{u}(\mathbf{x},t) i\hat{u}(\mathbf{x},t) \quad \text{(C.1)}$$

where we have used general d because we will be renormalizing. Before we continue, let us simplify by assuming that $J(\mathbf{x}'-\mathbf{x}, t'-t) = J(\mathbf{x}'-\mathbf{x})\delta(t-t')$, which eliminates the time integral.

Probably the biggest assumption that we make is that $\tilde{J}(\mathbf{x}-\mathbf{x}', t-t') \sim J/|\mathbf{x}-\mathbf{x}'|^{d+1}$ (where for $d=2$, scales like $|\mathbf{x}|^{-3}$), which means that we will ignore higher order terms (and in particular, ignore short range terms like ∇^2). The reason for this is that higher order terms will turn out to be irrelevant in the sense of RG [19]. The action is

$$S = \int d^d x dt i\hat{u}(\mathbf{x},t)\left(\eta \partial_t u(\mathbf{x},t) - \int d^d x' \frac{J(u(\mathbf{x}',t) - u(\mathbf{x},t))}{|\mathbf{x}'-\mathbf{x}|^{d+1}} - \Sigma(\mathbf{x},t)\right) - \frac{1}{2}\int d^d x dt dt' i\hat{u}(\mathbf{x},t) i\hat{u}(\mathbf{x},t')\Delta(u'-u) - \eta T \int d^d x dt i\hat{u}(\mathbf{x},t) i\hat{u}(\mathbf{x},t) \quad \text{(C.2)}$$

We will simplify this action further, by going into a comoving frame. This means $u \to u + vt$, where $v = \overline{\langle \partial_t 1/L^d \int d^d x u(\mathbf{x},t)\rangle}$ is the average velocity (L^d being the system size). In this case the action remains the same, except that $\partial_t u \to \partial_t u + \eta v$. In order to simplify this, we can absorb the ηv term into Σ, resulting in $\tilde{\Sigma} = \Sigma - \eta v$ defined in eq. 4.30. Also the term $\Delta(u'-u) = \Delta(u(\mathbf{x},t') - u(\mathbf{x},t)) \to \Delta(u(\mathbf{x},t') - u(\mathbf{x},t) + v(t'-t))$.

We can split the action into two parts, the quadratic and nonquadratic actions. The quadratic action is

$$S_q = \int d^d x dt i\hat{u}(\mathbf{x},t)\left(\eta \partial_t u(\mathbf{x},t) - \int d^d x' \frac{J(u(\mathbf{x}',t') - u(\mathbf{x},t))}{|\mathbf{x}'-\mathbf{x}|^{d+1}}\right) - \eta T \int d^d x dt i\hat{u}(\mathbf{x},t) i\hat{u}(\mathbf{x},t) \quad \text{(C.3)}$$

while the nonquadratic action is

$$S_{nq} = -\int d^d x dt i\hat{u}(\mathbf{x},t)\tilde{\Sigma}(\mathbf{x},t) - \frac{1}{2}\int d^d x dt dt' i\hat{u}(\mathbf{x},t) i\hat{u}(\mathbf{x},t')\Delta(u' - u + v(t'-t)). \tag{C.4}$$

Note that we consider the term $\Delta(0)$ to be nonquadratic. What this means is that we consider quantities to order Δ^0, and the vertex $\int i\hat{u}i\hat{u}\Delta(0)$ is first order in Δ. Therefore Δ acts as a perturbation in our picture, although of course, to first order this perturbation is computed exactly. The quadratic part can be simplified further by transforming to the Fourier domain $(\mathbf{q},\omega)$ and considering only the long wavelength behavior $|\mathbf{q}| \to 0$. In this case the interaction kernel

$$\int d^d x' \frac{J(u(\mathbf{x}',t') - u(\mathbf{x},t))}{|\mathbf{x}' - \mathbf{x}|^{d+1}} = J|\mathbf{q}|u(\mathbf{q},t) \tag{C.5}$$

which is necessarily the behavior for long wavelengths based on dimensional analysis and isotropy. More rigorously, we know that $\int d^d x' \frac{J(u(\mathbf{x}',t')}{|\mathbf{x}'-\mathbf{x}|^{d+1}}$ is a convolution, so it results in multiplication in the Fourier domain. The Fourier transform of $\tilde{J}(\mathbf{x}) = \tilde{J}(\mathbf{q})$ must scale as $|\mathbf{q}|$, but also at $\mathbf{q} = 0$, the Fourier transform must equal $\int d^d x \tilde{J}(\mathbf{x}) = \int d^d x/|\mathbf{x}|^{d+1}$. This means there must be an constant $\tilde{J}(\mathbf{q}) = JC|\mathbf{q}| + \tilde{J}(0)\delta(\mathbf{q})$, since the integral of $\int d^d x/|\mathbf{x}|^{d+1} \neq 0$. This constant term cancels the second term in the integral in eq. C.5. We absorb the constant C into the definition of J since it does not change the results.

In this case the quadratic action can be written

$$S_q = \int d^d q d\omega i\hat{u}(-\mathbf{q},-\omega)\left(i\omega\eta u(\mathbf{q},\omega) - J|\mathbf{q}|u(\mathbf{q},\omega) - \eta T i\hat{u}(\mathbf{q},\omega)\right). \tag{C.6}$$

Then we can write this quadratic action as a an integral over a quadratic form, evaluated for the pair of fields $i\hat{u}, u$. In this case

$$[i\hat{u}(-\mathbf{q},-\omega)\ u(-\mathbf{q},-\omega)]\begin{bmatrix} \eta T & i\eta\omega - J|\mathbf{q}| \\ -i\eta\omega - J|\mathbf{q}| & 0 \end{bmatrix}\begin{bmatrix} i\hat{u}(\mathbf{q},\omega) \\ u(\mathbf{q},\omega) \end{bmatrix} \tag{C.7}$$

where the minus sign in the quadratic form matrix comes from the fact that the arguments ω is swapped with $-\omega$ in the conjugate. Then the inverse of the quadratic form matrix will be the various (unrenormalized, or "bare") correlation functions. The inverse is

$$\begin{bmatrix} 0 & \frac{1}{J|\mathbf{q}|-i\eta\omega} \\ \frac{1}{J|\mathbf{q}|+i\eta\omega} & \frac{\eta T}{(J|\mathbf{q}|)^2+(\eta\omega)^2} \end{bmatrix}. \tag{C.8}$$

From this it is easy to read off the response function

$$R(\mathbf{q},\omega) = \langle\overline{i\hat{u}(-\mathbf{q},-\omega)u(\mathbf{q},\omega)}\rangle = \frac{1}{J|\mathbf{q}| - i\eta\omega} \tag{C.9}$$

and the correlation function

$$C(\mathbf{q},\omega) = \langle\overline{u(-\mathbf{q},-\omega)u(\mathbf{q},\omega)}\rangle = \frac{\eta T}{(J|\mathbf{q}|)^2 + (\eta\omega)^2} \tag{C.10}$$

while $\langle\overline{\hat{u}(-\mathbf{q},-\omega)\hat{u}(\mathbf{q},\omega)}\rangle = 0$. We will need the $\mathbf{q}, t$ response and correlation functions, as we need to impose the constraint that

$$R(\mathbf{q},t,t) = 0. \tag{C.11}$$

These are

$$R(\mathbf{q},t-t') = \frac{\Theta(t-t')}{\eta}e^{-J|\mathbf{q}||t-t'|/\eta} \tag{C.12}$$

$$C(\mathbf{q},t-t') = T\frac{e^{-J|\mathbf{q}||t-t'|/\eta}}{J|\mathbf{q}|} \tag{C.13}$$

where $\Theta(t)$ is the step function.

C.2 Rescaling the Action

The general strategy now is to find a rescaling of the action that keeps the quadratic part of the action eq. C.6 invariant to a scale transform. Before we attempt this, we need one more result, known as statistical tilt symmetry [11, 85]. Take the action eq. C.6 and eq. C.4, and do a shift of $u(\mathbf{q},\omega) \to u(\mathbf{q},\omega) + |J\mathbf{q}|^{-1}w(\mathbf{q})$. Note that $w(\mathbf{q})$ is time independent. Then $S \to S - \int d^dq d\omega i\hat{u}(-\mathbf{q},-\omega)w(\mathbf{q})$ (the $i\omega w(\mathbf{q})$ term turns to $\partial_t w(\mathbf{x}) = 0$ because of the time independence). Assume that $w(\mathbf{x}) \to 0$ as $|\mathbf{x}| \to \infty$, so that we can safely change variables of integration without worrying about boundary value terms. Then changing variables is simply a shift in integration, so

$$\int \mathcal{D}u\mathcal{D}\hat{u}ue^S = \int \mathcal{D}u\mathcal{D}\hat{u}\left(u(\mathbf{q},\omega) + |J\mathbf{q}|^{-1}w(\mathbf{q})\right)e^{S-\int d^dq d\omega i\hat{u}(-\mathbf{q},-\omega)w(\mathbf{q})}. \tag{C.14}$$

Taking the functional derivative evaluated at the null function $\delta/\delta w(\mathbf{q})|_{w(\mathbf{q})=0}$, we get

$$0 = \int \mathcal{D}u\mathcal{D}\hat{u}|J\mathbf{q}|^{-1}e^{S} - u(\mathbf{q},0)i\hat{u}(-\mathbf{q},0)e^{S} \tag{C.15}$$

$$\int_0^\infty dtR_r(\mathbf{q},t) = \langle\overline{u(\mathbf{q},0)i\hat{u}(-\mathbf{q},0)}\rangle = |J\mathbf{q}|^{-1}\int \mathcal{D}u\mathcal{D}e^{S} = |J\mathbf{q}|^{-1} \tag{C.16}$$

where we know from the fact that the Jacobian is 1 that $\int \mathcal{D}u\mathcal{D}e^S = 1$, and $R_r(\mathbf{q},t)$ is the full renormalized action. What this means is that the constant J does not get renormalized, and remains invariant under any RG transformation.

Now we perform a simple scale transform $\mathbf{q}' = b\mathbf{q}$, so that

$$S_q = \int d^dq'b^{-d}d\omega'b^{-z}i\hat{u}(-\mathbf{q}',-\omega')\left(i\omega'\eta'b^{-z}u(\mathbf{q}',\omega') - J|\mathbf{q}'|b^{-1}u(\mathbf{q}',\omega') - \eta'T'i\hat{u}(\mathbf{q}',\omega')\right). \tag{C.17}$$

where z is the dynamical exponent defined so that $\omega' = b^z\omega$ and J is invariant. In order for this action to remain invariant $\hat{u}(-\mathbf{q}',-\omega')u(\mathbf{q}',\omega') = b^{-d-2z}\hat{u}'(-\mathbf{q}',-\omega')u'(\mathbf{q}',\omega') = b^{-d-z-1}\hat{u}'(-\mathbf{q}',-\omega')u'(\mathbf{q}',\omega')$ which gives us that $z = 1$. Here u' and $\hat{u}'$ denote the rescaled fields.

The nonquadratic action S_{nq} also has a quadratic piece. This piece comes from the Taylor expansion of $\Delta(u(\mathbf{x},t) - u(\mathbf{x},t') + v(t-t')) = \sum_n \Delta^{(n)}(v(t-t'))/n!(u(\mathbf{x},t) - u(\mathbf{x},t'))^n$ evaluated at $n = 0$, where $\Delta^{(n)}$ is the nth derivative of Δ. This results in

$$\int d^dxdtdt'i\hat{u}(\mathbf{x},t)i\hat{u}(\mathbf{x},t')\Delta(v(t-t')) = \int d^dqd\omega i\hat{u}(-\mathbf{q},-v\omega)i\hat{u}(\mathbf{q},v\omega)\Delta(\omega) \tag{C.18}$$

which must remain constant since $\Delta(0)$ does not depend on rescaling. Then

$$\int d^dq'b^{-d}d\omega'b^{-z}i\hat{u}(-\mathbf{q}',-\omega')i\hat{u}(\mathbf{q}',\omega')\Delta(0). \tag{C.19}$$

This implies that $\hat{u}(-\mathbf{q}',-\omega')\hat{u}(\mathbf{q}',\omega') = b^{d+z}\hat{u}'(-\mathbf{q}',-\omega')\hat{u}'(\mathbf{q}',\omega') = b^{d+1}\hat{u}'(-\mathbf{q}',-\omega')\hat{u}'(\mathbf{q}',\omega')$ or $b^{\frac{d+1}{2}}\hat{u}(\mathbf{q}',\omega') = \hat{u}'(\mathbf{q}',\omega')$ where $\hat{u}'(\mathbf{q}',\omega')$ is the rescaled field. Then $b^{d/2-1}u(\mathbf{q}',\omega') = u'(\mathbf{q}',\omega')$.

Now if we are performing an iterative RG, the we will rescale $b < 1$ since we want $\mathbf{q}'/\mathbf{q} < 1$, as $\mathbf{q} \to 0$ is the long wavelength limit. Therefore *relevant* variables will have an exponent that is negative as they will grow larger, while *irrelevant* variables will have an exponent which is positive, as they will grow smaller. The field u is marginal when $d = d_c = 2$ and relevant when $d < d_c = 2$, since $d/2 - 1 < 0$ for $d < d_c$ so u' grows with shrinking b. What is key is the terms which we call nonquadratic. This includes the linear term

$\tilde{\Sigma}\int d^dqdti\hat{u}$, which can easily be handled, and the truly nonlinear term

$$\int d^dxdtdt'\Delta(u(\mathbf{x},t')-u(\mathbf{x},t)+v(t'-t))i\hat{u}(\mathbf{x},t)i\hat{u}(\mathbf{x},t'). \tag{C.20}$$

Since $\Delta(x)$ is a function, we can hope that it has a Taylor expansion near 0. Such terms would be of the form

$$\int d^dxdtdt'\frac{\Delta^{(n)}(v(t'-t))}{n!}(u(\mathbf{x},t')-u(\mathbf{x},t))^n i\hat{u}(\mathbf{x},t)i\hat{u}(\mathbf{x},t') \tag{C.21}$$

Here $\Delta^{(n)}$ represents a derivative of $\Delta(x)$. Expanding this in terms of $\mathbf{q},\omega$ would be messy. Instead, we just observe that $\mathbf{q}'=b\mathbf{q}\to\mathbf{x}'=b^{-1}\mathbf{x}$, and $\omega'=b^z\omega\to t'=b^{-z}t$, but otherwise nothing changes. Therefore $u(\mathbf{x}',t')=b^{d/2-1}u'(\mathbf{x}',t')$ and $\hat{u}(\mathbf{x}',t')=b^{1+d/2}\hat{u}'(\mathbf{x}',t')$. The vertex $\Delta^{(n)}$ then rescales like $b^{-n(d/2-1)}$, and the whole vertex is *marginal* when $d=d_c=2$. In other words, all derivatives are marginal and hence the entire function is marginal. As promised, we have to renormalize infinitely many variables here. Note that this isn't a problem for us, since we have a finite cutoff Λ.

Before we consider perturbations from the disorder Δ, we want to comment on the general structure of the RG. In RG we will be transforming the various constants infinitesimally, so the rescaling factor $\delta b=be^{-\delta\ell}=b(1-\delta\ell)$. We will do this in generic $d<d_c$, taking $\epsilon=d_c-d$ to be a "small" parameter, with the hopes that ϵ can be continued to large values, since the only physical value we can have is $d=1$ or 2, so $\epsilon=1$ or 0. As we transform equations, we will find that certain quantities grow or shrink depending on ϵ and ℓ.

C.3 Scaling Relations

Let us write some exponents in terms of ϵ to simplify things. We let ζ be the scaling dimension of the field $u(\mathbf{x},t)$ and $d-\theta$ be the scaling dimension of $\hat{u}(\mathbf{x},t)$. The stress $\tilde{\Sigma}$ scales as $d-\theta-z-d=-\theta-z$. The exponents θ and ζ are therefore of $\mathcal{O}(\epsilon)$, although they are not equal to the naive scaling dimensions. We need several exponent relations now [11, 163]. Since we are tuning the stress Σ, we can define the correlation length $\xi\sim(\Sigma-\Sigma_c)^{-\nu}$. This also implies that

$$\nu=\frac{1}{\theta+z}. \tag{C.22}$$

Any deformation $\delta u\sim\xi^\zeta$ then, by the above definition.

From eq. C.16, we can use the definition of the response function

$$\frac{\delta u(\mathbf{q},\omega=0)}{\delta\Sigma(\mathbf{q},\omega=0)}=\int dt R_r(\mathbf{q},t)\sim\frac{1}{|\mathbf{q}|} \tag{C.23}$$

to relate $\delta u\sim\xi^{\zeta}$, $\delta\Sigma\sim\xi^{-1/\nu}$, and $|\mathbf{q}|\sim\xi^{-1}$ to get $\zeta+1/\nu=1$ or

$$\nu=\frac{1}{1+\zeta}. \tag{C.24}$$

We will use the identity $\theta+z=1+\zeta$ by combining eqs. C.22 and C.24 several times.

C.4 Coarse Graining and the Renormalization Equations

The second step in RG is to define a coarse graining procedure. To be general, let $\mathbf{u}=[i\hat{u}\ u]^T$, the vector of fields we are renormalizing. The path integral defining the theory can be written

$$Z=\int_{\mathbf{u}(0)}^{\mathbf{u}(\Lambda)}\mathcal{D}\mathbf{u}e^{S}. \tag{C.25}$$

Here the $\mathbf{u}(0)$ and $\mathbf{u}(\Lambda)$ are schematic representations for fields $\mathbf{u}$ with zero momentum to fields $\mathbf{u}$ with momentum Λ, which is the highest momentum in the theory. This can be coarse grained by considering

$$Z=\int_0^{\mathbf{u}(b\Lambda)}\mathcal{D}\mathbf{u}\int_{\mathbf{u}(b\Lambda)}^{\mathbf{u}(\Lambda)}\mathcal{D}\mathbf{u}e^{S}=\int_0^{b\Lambda}\mathcal{D}\mathbf{u}e^{\tilde{S}} \tag{C.26}$$

where $\tilde{S}$ is a new effective action. The primary idea behind renormalization is that the terms in $\tilde{S}$ should be of the same form as the terms in S, from which we can have a well defined flow of each term. We now transform coordinates so that $\mathbf{q}'=b\mathbf{q}$ (i.e. $\Lambda'=b\Lambda$). As we can do this iteratively, it is good to think of $b=(1-\delta\ell)$. Now of course, in doing this, we will have scaling for each of the terms in the action so that we do not have any dangling powers of b. All of these terms can be handled, except the nonquadratic term $\Delta(u-u')$. If $\epsilon>0$, this term grows exponentially. So we actually have to do a double expansion, known as the ϵ expansion [20] with ϵ close to 0, since we can only handle the nonlinear term $\Delta(u-u')$ perturbatively (i.e. for small values). In our case, this perturbative expansion is good as long as the starting point $\Delta_0(u-u')$ of the expansion is small, since we are most interested in the $\epsilon=0$ case.

Going into more detail now, we split the fields $u^{<},\hat{u}^{<}$ and $u^{>},\hat{u}^{>}$. Here $u^{>}$ and $\hat{u}^{>}$ define fields that have large momenta $|\mathbf{q}| \in [b\Lambda, \Lambda]$. The generating functional

$$Z = \int \mathcal{D}u\mathcal{D}\hat{u}e^{S_q+S_{nq}} = \int \mathcal{D}u^{<}\mathcal{D}\hat{u}^{<}\mathcal{D}u^{>}\mathcal{D}\hat{u}^{>}e^{S_q(u^{<}+u^{>},\hat{u}^{<}+\hat{u}^{>})+S_{nq}(u^{<}+u^{>},\hat{u}^{<}+\hat{u}^{>})} \tag{C.27}$$

$$Z = \int \mathcal{D}u^{<}\mathcal{D}\hat{u}^{<}\mathcal{D}u^{>}\mathcal{D}\hat{u}^{>}e^{S_q(u^{<},\hat{u}^{<})+S_q(u^{>},\hat{u}^{>})}e^{S_{nq}} = \int \mathcal{D}u^{<}\mathcal{D}\hat{u}^{<}e^{S_q(u^{<},\hat{u}^{<})}\langle e^{S_{nq}}\rangle_q \tag{C.28}$$

$$Z = \int \mathcal{D}u^{<}\mathcal{D}\hat{u}^{<}e^{S_q(u^{<},\hat{u}^{<})+\ln\langle e^{S_{nq}}\rangle_q} \tag{C.29}$$

$$Z = \int \mathcal{D}u^{<}\mathcal{D}\hat{u}^{<}e^{S_q(u^{<},\hat{u}^{<})+\langle S_{nq}\rangle_q+\frac{1}{2}(\langle S_{nq}^2\rangle_q-\langle S_{nq}\rangle_q^2)+\ldots} \tag{C.30}$$

where $\langle\cdot\rangle_q$ is the mean with respect to the quadratic action over the variables $u^{>}$ and $\hat{u}^{>}$.

It is somewhat easier to do part of the action in the position basis $\mathbf{x}, t$ because the $\Delta(u - u')$ term is difficult to handle in the momentum basis.

$$\begin{gathered}S_{nq} = -\int d^dxdti(\hat{u}^{<}(\mathbf{x},t) + \hat{u}^{>}(\mathbf{x},t))\tilde{\Sigma} \\ -\frac{1}{2}\int d^dxdtdt'i(\hat{u}^{<}(\mathbf{x},t)+\hat{u}^{>}(\mathbf{x},t))i(\hat{u}^{<}(\mathbf{x},t')+\hat{u}^{>}(\mathbf{x},t'))\Delta(u^{<}(\mathbf{x},t')+u^{>}(\mathbf{x},t')-u^{<}(\mathbf{x},t)-u^{>}(\mathbf{x},t)+v(t'-t)).\end{gathered} \tag{C.31}$$

To calculate $\langle S_{nq}\rangle$, we first average over the term with $\tilde{\Sigma}$ which is zero. The second term is a somewhat unwieldy problem which can be significantly simplified by transforming

$$\Delta(x) = \int \frac{dp}{2\pi}e^{ipx}\Delta(p) \tag{C.32}$$

with $x = u^{<}(\mathbf{x},t') + u^{>}(\mathbf{x},t') - u^{<}(\mathbf{x},t) - u^{>}(\mathbf{x},t) + v(t' - t)$. The average $\langle S_{nq}\rangle_q$ includes the terms $\langle\overline{\hat{u}^{<}\hat{u}^{<}\Delta}\rangle_q = \hat{u}^{<}\hat{u}^{<}\langle\overline{\Delta}\rangle_q$, $\langle\overline{2\hat{u}^{>}\hat{u}^{<}\Delta}\rangle_q = 2\hat{u}^{<}\langle\overline{\hat{u}^{>}\Delta}\rangle_q$ and $\langle\overline{\hat{u}^{>}\hat{u}^{>}\Delta}\rangle_q$. If we represent everything in terms of the Fourier transform eq. C.32, we can simplify these expressions. Recalling our correlation functions eq. C.12 and eq. C.13, we find

$$\left\langle\overline{e^{ip(u^{>}(\mathbf{x},t)-u^{>}(\mathbf{x},t'))}}\right\rangle_q = e^{(ip)^2\left(C^{>}(0,0)-C^{>}(0,(t-t'))\right)} \tag{C.33}$$

$$\left\langle\overline{\hat{u}^{>}(\mathbf{x},t)e^{ip(u^{>}(\mathbf{x},t)-u^{>}(\mathbf{x},t'))}}\right\rangle_q = ipe^{(ip)^2(C^{>}(0,0)-C^{>}(0,t-t'))}R^{>}(0,(t-t')) \tag{C.34}$$

$$\left\langle\overline{\hat{u}^{>}(\mathbf{x},t)\hat{u}^{>}(\mathbf{x},t')e^{ip(u^{>}(\mathbf{x},t)-u^{>}(\mathbf{x},t'))}}\right\rangle_q = 0 \tag{C.35}$$

which can be found by Taylor expanding the exponentials. Here $R^{>}(0, t - t')$ and $C^{>}(0, t - t')$ are in the $\mathbf{x}, t$ basis for $b\Lambda < |\mathbf{q}| < \Lambda$.

We can simplify things by considering that both $C^{>}$ an $R^{>}$ must be of order $d\ell$, and in particular using eqs. C.12 and C.13 we have

$$C^{>}(0,\tau) = T\Lambda^d S_d \frac{e^{-c\Lambda\tau/\eta}}{c\Lambda} d\ell \tag{C.36}$$

$$R^{>}(0,\tau) = \frac{\Theta(\tau)}{\eta}\Lambda^d S_d e^{-c\Lambda\tau/\eta} d\ell \tag{C.37}$$

where S_d is the surface area of the d sphere. Therefore we only need to analyze terms that are up to first order in $C^{>}$ and $R^{>}$.

Now we look at the various terms. First from eq. C.34,

$$-\int d^d x dt dt' i\hat{u}^{<}(\mathbf{x},t) R^{>}(0,(t-t')) \int_p ipe^{ik(u^{<}(\mathbf{x},t)-u^{<}(\mathbf{x},t')+v(t-t'))}\Delta(p) e^{(ip)^2\left(C^{>}(0,0)-C^{>}(0,(t-t'))\right)} \tag{C.38}$$

has one power of $\hat{u}^{<}(\mathbf{x},t)$. Therefore it can act as a correction to either $\tilde{\Sigma}$ or $\eta\partial_t u(\mathbf{x},t)$. The $\tilde{\Sigma}$ correction term is the $0th$ order correction on expanding $\exp(ip(u^{<}(\mathbf{x},t)-u^{<}(\mathbf{x},t'))) = 1 + ip(u^{<}(\mathbf{x},t)-u^{<}(\mathbf{x},t')) + \dots$ and the correlation functions in the exponent. This term reads

$$-\int d^d x dt dt' i\hat{u}^{<}(\mathbf{x},t) R^{>}(0,(t-t')) \int_p ipe^{ipv(t-t')}\Delta(p) \tag{C.39}$$

where the operators $C^{>}$ disappear because of the $R^{>}$ which is already of order $d\ell$. If we substitute in $\tau = t - t'$ then we have

$$\delta\tilde{\Sigma} = \int d^d x dt i\hat{u}^{<}(\mathbf{x},t) \int d\tau \frac{dp}{2\pi} R^{>}(0,\tau) ipe^{ipv\tau}\Delta(p). \tag{C.40}$$

where the negative sign disappers because the $\tilde{\Sigma}$ also has a negative sign in front. The first order correction $ip(u^{<}(\mathbf{x},t)-u^{<}(\mathbf{x},t')) \approx ip\partial_t u^{<}(\mathbf{x},t)(t-t')$ which results in

$$\delta\eta = -\int d^d x dt i\hat{u}^{<}(\mathbf{x},t)\partial_t u^{<}(\mathbf{x},t) \int d\tau \frac{dp}{2\pi} R^{>}(0,\tau)\tau(ip)^2 e^{ipv\tau}\Delta(p) \tag{C.41}$$

which is clearly a correction to η. We want to put this in terms of $C^{>}(0,\tau)$, so since $\Theta(\tau)\partial_t C^{>}(0,\tau) =$

$TR^{>}(0,\tau)$ from eq. C.36 and eq. C.37, so

$$dv = TR^{>}(0,\tau) \tag{C.42}$$

$$u = \tau e^{ipv\tau} \tag{C.43}$$

$$v = C^{>}(0,\tau) \tag{C.44}$$

$$du = (1+ipv\tau)e^{ipv\tau} \tag{C.45}$$

Then

$$T\delta\eta = -\int d\tau \frac{dp}{2\pi}(1+ipv\tau)e^{ipv\tau}(ip)^2 C^{>}(0,\tau) \tag{C.46}$$

What about other terms, such as $\partial_t^2 u$ and $(\partial_t u)^2$ and so forth? These terms turn out to be *irrelevant*, as the extra powers of z ensure that they shrink upon renormalization [10]. Therefore they can be ignored safely.

The second term to look at is from eq. C.33,

$$-\int d^d x dt dt' i\hat{u}^{<}(\mathbf{x},t) i\hat{u}^{<}(\mathbf{x},t') \int_p e^{ip(u^{<}(\mathbf{x},t)-u^{<}(\mathbf{x},t')+v(t-t'))}\Delta(p) e^{(ip)^2(C^{>}(0,0)-C^{>}(0,t-t'))}. \tag{C.47}$$

This term must generate the disorder potential, as well as corrections to the ηT term and the disorder potential. Let us expand

$$-\int d^d x dt dt' i\hat{u}^{<}(\mathbf{x},t) i\hat{u}^{<}(\mathbf{x},t') \int_p e^{ip(u^{<}(\mathbf{x},t)-u^{<}(\mathbf{x},t')+v(t-t'))}\Delta(p)(1+(ip)^2(C^{>}(0,0)-C^{>}(0,t-t'))) \tag{C.48}$$

Then

$$-\int d^d x dt dt' i\hat{u}^{<}(\mathbf{x},t) i\hat{u}^{<}(\mathbf{x},t') \int_p e^{ip(u^{<}(\mathbf{x},t)-u^{<}(\mathbf{x},t')+v(t-t'))}\Delta(p) = \tag{C.49}$$

$$-\int d^d x dt dt' i\hat{u}^{<}(\mathbf{x},t) i\hat{u}^{<}(\mathbf{x},t') \Delta(u^{<}(\mathbf{x},t)-u^{<}(\mathbf{x},t')+v(t-t'))) \tag{C.50}$$

will generate the vertex itself, the left over

$$-\int d^d x dt dt' i\hat{u}^{<}(\mathbf{x},t) i\hat{u}^{<}(\mathbf{x},t') \int_p e^{ip(u^{<}(\mathbf{x},t)-u^{<}(\mathbf{x},t')+v(t-t'))}\Delta(p)(ip)^2(C^{>}(0,0)-C^{>}(0,t-t')). \tag{C.51}$$

will correct the vertex and the product ηT. The $C^{>}(0,0)$ term corrects the vertex, since it doesn't alter the integral $\int dtdt' u^<(\mathbf{x},t)u^<(\mathbf{x},t')$, so

$$\delta\Delta = \int \frac{dp}{2\pi} e^{ip(u^<(\mathbf{x},t)-u^<(\mathbf{x},t')+v(t-t'))}\Delta(p)(ip)^2 C^>(0,0) \tag{C.52}$$

The left over, when projected to $u(\mathbf{x},t) = u(\mathbf{x},t')$ in the outside integral

$$\delta(\eta T) = -\int \frac{dp}{2\pi} d\tau e^{ipv\tau}\Delta(p)(ip)^2 C^>(0,\tau). \tag{C.53}$$

will correct ηT.

To calculate the correction to temperature, we must use the product rule, so that $\delta(\eta T) - T\delta\eta = \eta\delta T$. This gives a corrections

$$\eta\delta T = \int \frac{dp}{2\pi} d\tau v\tau\Delta(p)e^{ipv\tau}(ip)^3 C^>(0,\tau) \tag{C.54}$$

$$\delta\eta = -\int \frac{dp}{2\pi} d\tau R^>(0,\tau)(ip)^2 e^{ipv\tau}\Delta(p) \tag{C.55}$$

$$\delta\tilde{\Sigma} = \int \frac{dp}{2\pi} d\tau R^>(0,\tau) ipe^{ipv\tau}\Delta(p) \tag{C.56}$$

$$\delta\Delta(u) = \int \frac{dp}{2\pi} e^{ipu}\Delta(p)(ip)^2 C^>(0,0) \tag{C.57}$$

We have an almost closed set of equations C.54-C.57. The only missing piece is that v will be coupled with η once we plug in eqs C.36 and C.37. Since v is not corrected by the interaction (as $\langle\overline{\partial_t u}\rangle$ no powers of $\hat{u}$) $v\delta\eta = \delta(v\eta)$, so

$$\eta T' = (1 + (\epsilon - 1 - 2\zeta)d\ell)\eta T + \frac{T\Lambda^d S_d}{c\Lambda}\int \frac{dp}{2\pi} d\tau e^{-c\Lambda\tau/\eta} ipv\tau\Delta(p)e^{ikp\tau}(ip)^2 d\ell \tag{C.58}$$

$$f' = (1 + (1-\zeta)d\ell)f + \frac{\Lambda^d S_d}{\eta}\int \frac{dp}{2\pi} d\tau\Theta(\tau)e^{-c\Lambda\tau/\eta} ipe^{ipv\tau}\Delta(p)d\ell \tag{C.59}$$

$$(\eta v)' = (1 + (1-\zeta)d\ell)\eta v - \frac{\Lambda^d S_d}{\eta}\int \frac{dp}{2\pi} d\tau v\Theta(\tau)e^{-c\Lambda\tau/\eta}(ip)^3 e^{ipv\tau}\Delta_k d\ell \tag{C.60}$$

$$\Delta'(u') = (1 + (\epsilon - 2\zeta)d\ell)\Delta(u) + \zeta h\partial_u\Delta(u)d\ell + \frac{T\Lambda^d S_d}{c\Lambda}\Delta''(u)d\ell. \tag{C.61}$$

which hopefully shows why we chose the rescalings in eq. 4.28-eq. 4.31. The full set of equations is almost complete, the last step being to calculate the second order or one loop correction to the vertex Δ.

C.4.1 Second Order Vertex Correction

Before we conclude, we need to calculate *second* order expansions for Δ, because the vertex must be corrected to second order to correctly calculate first order in ϵ. We managed to calculate first order quantities without diagrams, because these were simple enough to do with an expansion. Second order quantities will be done using diagrams which were first developed for application to charge density waves [10]. The rules are somewhat complex because the vertex is nonlocal in time.

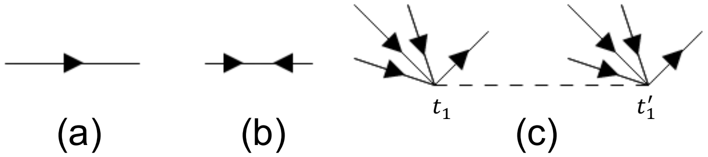

Figure C.1: The diagrams we will need. (a) The half propagator, which represents either $u(\mathbf{x},t)$ or $\hat{u}(\mathbf{x},t)$ depending on whether it enters or leaves a vertex. Arrows pointing towards a vertex are $u(\mathbf{x},t)$, arrows pointing away are $\hat{u}(\mathbf{x},t)$. (b) The diagram representing the correlation function eq. C.13, which shows two arrows pointing towards each other, meaning a term like $u(\mathbf{x},t)u(\mathbf{x}',t')$. (c) The vertex $\Delta(u-u'+v(t_1-t_1'))\hat{u}\hat{u}'$ (where primes denote time differences). We expand $\Delta(u-u'+v(t_1-t_1'))$ into a Taylor series, which results in powers of u. Here we draw an example of a diagram with three u and u' entering into the vertex, but in general it is best to think of this diagram as a sum of diagrams with m, n arrows entering into each vertex, with the derivative of the vertex being the $m+n$th derivative. The dotted line means that the arguments are considered at different times. This diagram would represent a term $(-1)^3 \frac{\binom{6}{3}}{3!} \frac{d^6}{du^6}\Delta(u)|_{v(t-t')} u^3 u'^3 \hat{u}'\hat{u}$. For the m, nth vertex, the term would be $(-1)^n \frac{\binom{m+n}{n}}{(m+n)!} \frac{d^{m+n}}{du^{m+n}} \Delta(u)|_{v(t-t')} u^m u'^n \hat{u}'\hat{u}$. When an arrow leaves one vertex ($\hat{u}$) and enters another (u), one has a contraction $\hat{u}u$, which results in a propagator $R(\mathbf{q}, t_1^+ - t_1)$. Remembering that $R(\mathbf{q}, 0) = 0$ by definition, it implies that $t_1^+ > t_1$.

The description of how the diagrams work is given above, and is also the exact prescription given in [10]. The biggest challenge is to sum up infinitely many diagrams consistently and carefully. The diagram we are interested in corrects the vertex, which means it has a $\hat{u}\hat{u}'$ behavior. According to fig. C.1, this diagram would have *two* vertexes like fig. C.1(c), which would then have to be connected because only two arrows can leave the diagram to get the $\hat{u}\hat{u}'$ behavior.

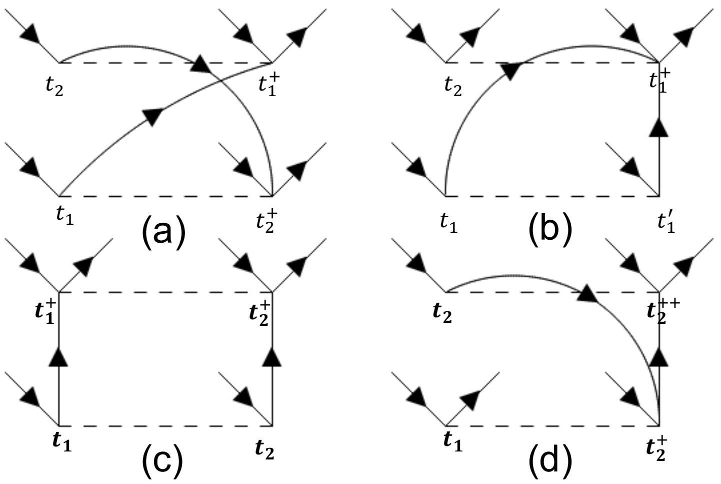

Figure C.2: The diagrams relevant for renormalizing the vertex. For brevity we have only drawn single incoming lines to each vertex, but in reality one is summing over all powers of $(uu')^n$. The intuition behind interpreting these diagrams is that for each outgoing line from a vertex that connects to another vertex, an incoming line from that vertex must be taken. The taken vertex results in a power one power smaller in the expansion series, so one is summing $(uu')^{n-1}/n!$. Since there are n ways to take a vertex, there is also a factor of n that multiplies each diagram. Therefore what it does is effectively take the derivative, as $x^n/n! \to x^{n-1}/(n-1)!$. As the arrows can only connect past times to future times, we have denoted future times with a + superscript, based on previous notation [10]. (a) Each vertex gets hit by a single propagator. Therefore one has a correction of the form $\Delta'(u)^2$. (b) Both propagators hit the upper vertex, therefore one has $\Delta''(u)\Delta(u)$ correction. (c) Again a correction of type $\Delta''(u)\Delta(u)$. (d) A correction of type $\Delta'(u)^2$.

To one loop we will add terms to the disorder. We consider the diagrams from above. Let us call $\tau_1 = t_1^+ - t_1$ and $\tau_2 = t_2^+ - t_2$. Then (a) results in

$$\begin{aligned}
D_a = &\int_{\Lambda(1-d\ell)}^{\Lambda} dt_1 dt_2 \frac{d^d q}{(2\pi)^d} \overline{\langle \hat{u}(-\mathbf{q}, t_1) u(\mathbf{q}, t_1^+)\rangle}\,\overline{\langle \hat{u}(-\mathbf{q}, t_2) u(\mathbf{q}, t_2^+)\rangle} \\
&\times \sum_{m,n} \frac{T_{m,n}}{(n-1)!m!} u^{n-1}(\mathbf{x}, t_1^+) u^m(\mathbf{x}, t_2) \sum_{k,l} \frac{T_{k,l}}{(k-1)!l!} u^{k-1}(\mathbf{x}, t_2^+) u^l(\mathbf{x}, t_1) \\
= &-\int d\tau_1 d\tau_2 \frac{S_d \Lambda^d e^{-J\Lambda(\tau_1+\tau_2)/\eta}}{\eta^2} d\ell \Delta'(u(\mathbf{x}, t_1^+) - u(\mathbf{x}, t_2^+ - \tau_2) - v(t_1^+ - t_2^+ + \tau_2)) \times \\
&\Delta'(u(\mathbf{x}, t_2^+) - u(\mathbf{x}, t_1^+ - \tau_1) + v(t_2^+ - t_1^+ + \tau_1)) \qquad \text{(C.62)}
\end{aligned}$$

where $T_{m,n} = \binom{m}{n}(-1)^n \Delta^{(m+n)}(v(t-t'))$, which results in a correction

$$-\int_{t>0,t'>0} e^{-t-t'}\Delta'(u+t\lambda)\Delta'(u-t'\lambda) \tag{C.63}$$

after substituting $t = J\tau_1\Lambda/\eta$ and $t' = J\tau_2\Lambda/\eta$. The second diagram results in

$$\begin{aligned} D_b = \int_{\Lambda(1-d\ell)}^{\Lambda} & dt_1 dt_2 \frac{d^d q}{(2\pi)^d} \overline{\langle \hat{u}(-\mathbf{q},t_1)u(\mathbf{q},t_1^+)\rangle}\,\overline{\langle \hat{u}(-\mathbf{q},t_1')u(\mathbf{q},t_1^+)\rangle} \\ & \times \sum_{m,n} \frac{T_{m,n}}{(n-2)!m!} u^{n-2}(\mathbf{x},t_1^+)u^m(\mathbf{x},t_2) \sum_{k,l} \frac{T_{k,l}}{k!l!} u^k(\mathbf{x},t_1')u^l(\mathbf{x},t_1) \\ = & -\int d\tau_1 d\tau_2 \frac{S_d \Lambda^d e^{-J\Lambda(\tau_1+\tau_2)/\eta}}{\eta^2} d\ell \Delta''(u(\mathbf{x},t_1^+) - u(\mathbf{x},t_2) - v(t_1^+ - t_2))\times \\ & \Delta(u(\mathbf{x},t_1^+ - \tau_1) - u(\mathbf{x},t_1^+ - \tau_2) + v(\tau_2 - \tau_1)). \end{aligned} \tag{C.64}$$

The third in

$$\begin{aligned} D_c = \int_{\Lambda(1-d\ell)}^{\Lambda} & dt_1 dt_2 \frac{d^d q}{(2\pi)^d} \overline{\langle \hat{u}(-\mathbf{q},t_1)u(\mathbf{q},t_1^+)\rangle}\,\overline{\langle \hat{u}(-\mathbf{q},t_2)u(\mathbf{q},t_2^+)\rangle} \\ & \times \sum_{m,n} \frac{T_{m,n}}{(n-1)!(m-1)!} u^{n-1}(\mathbf{x},t_1^+)u^{m-1}(\mathbf{x},t_2^+) \sum_{k,l} \frac{T_{k,l}}{k!l!} u^k(\mathbf{x},t_1^+ - \tau_1)u^l(\mathbf{x},t_2^+ - \tau_2) \\ = & -\int d\tau_1 d\tau_2 \frac{S_d \Lambda^d e^{-J\Lambda(\tau_1+\tau_2)/\eta}}{\eta^2} d\ell \Delta''(u(\mathbf{x},t_1^+) - u(\mathbf{x},t_2^+) - v(t_1^+ - t_2^+))\times \\ & \Delta(u(\mathbf{x},t_1^+ - \tau_1) - u(\mathbf{x},t_2^+ - \tau_2) + v(t_1^+ - t_2^+ + \tau_2 - \tau_1)), \end{aligned} \tag{C.65}$$

which results in a correction

$$-\int_{t>0,t'>0} e^{-t-t'}\Delta''(u)\Delta(u+(t'-t)\lambda). \tag{C.66}$$

And finally

$$\begin{aligned} D_d = \int_{\Lambda(1-d\ell)}^{\Lambda} & dt_1 dt_2 \frac{d^d q}{(2\pi)^d} \overline{\langle \hat{u}(-\mathbf{q},t_1)u(\mathbf{q},t_1^+)\rangle}\,\overline{\langle \hat{u}(-\mathbf{q},t_1')u(\mathbf{q},t_1^+)\rangle} \\ & \times \sum_{m,n} \frac{T_{m,n}}{(n-2)!m!} u^{n-2}(\mathbf{x},t_1^+)u^m(\mathbf{x},t_2) \sum_{k,l} \frac{T_{k,l}}{k!l!} u^k(\mathbf{x},t_1')u^l(\mathbf{x},t_1) \\ = & -\int d\tau_1 d\tau_2 \frac{S_d \Lambda^d e^{-J\Lambda(\tau_1+\tau_2)/\eta}}{\eta^2} d\ell \Delta''(u(\mathbf{x},t_1^+) - u(\mathbf{x},t_2) - v(t_1^+ - t_2))\times \\ & \Delta(u(\mathbf{x},t_1^+ - \tau_1) - u(\mathbf{x},t_1^+ - \tau_2) + v(\tau_2 - \tau_1)), \end{aligned} \tag{C.67}$$

These together will result in the second order correction in eq. 4.35.

C.5 Solution of the Disorder Correlator Renormalization at the Upper Critical Dimension

The analysis here is close to [165]. We will solve eq. 4.35 with the assumptions that $\kappa \to 0$, fixed $\tilde{T}$, and $\epsilon = 0$ (the upper critical dimension). The RG equation with these assumptions is

$$\partial_\ell \tilde{\Delta}(u) = \tilde{T}\tilde{\Delta}''(u) + \tilde{\Delta}''(u)(\tilde{\Delta}(0) - \tilde{\Delta}(u)) - \tilde{\Delta}'^2 \tag{C.68}$$

We make the assumption that $\tilde{\Delta}(u) = \phi(\ell)\rho(z\psi(\ell))$, which is known as the automodel form [165]. We plug in this form to obtain

$$\phi'\rho(z\psi) + z\psi'\phi\rho'(z\psi) = \hat{T}\phi^2\psi^2\rho''(z\psi) + \phi^2\psi^2\rho''(z\psi)(\rho(0) - \rho(z\psi)) - \phi^2\psi^2\rho'(z\psi)^2 \tag{C.69}$$

where $\psi' = \partial_\ell\psi$, $\phi' = \partial_\ell\phi$ and $\hat{T} = \tilde{T}\phi$. The form of the equation now suggests that one can set

$$\phi' = -\phi^2\psi^2 \tag{C.70}$$

$$\psi' = -\phi\psi^3 \tag{C.71}$$

where the minus signs maintain consistency with [165]. Letting $\psi z = u$ means that

$$(u\rho)' = \rho'^2 - \hat{T}\rho'' - \rho''(\rho(0) - \rho). \tag{C.72}$$

We need one more constraint, in particular dividing $\psi'/\phi' = \psi/\phi$, so that $\psi/\phi = a$ is a constant yet to be determined. Solving for ψ and ϕ through separation of variables and using $\psi/\phi = a$ we get

$$\phi(\ell) = (3a^2\ell)^{-1/3} \tag{C.73}$$

$$\psi(\ell) = (3\ell/a)^{-1/3}. \tag{C.74}$$

One can write the right hand side of eq. C.72 as $(\rho^2/2 - \rho(\rho(0) - \hat{T}))''$, which immediately yields

$$u\rho = (\rho^2/2 - \rho(\rho(0) - \hat{T}))' + k = \rho\rho' - \rho'(\rho(0) - \hat{T}) + k. \tag{C.75}$$

Plugging in at $u = 0$ gives $0 = \rho(0)\rho'(0) - \rho'(0)\rho(0) - \rho'(0)\hat{T} + k$. We now use that if $\hat{T} > 0$, then no cusp forms, which *a priori* is an assumption that is true as we have seen (see fig. 4.4). Then $\rho'(0) = 0$ so that

$k = 0$. On the other hand, if $\hat{T} = 0$ then $k = 0$ since the terms cancel. Then

$$u = \rho' - \rho'/\rho(\rho(0) - \hat{T}) \tag{C.76}$$

$$\frac{u^2}{2} = \rho - \ln(\rho)(\rho(0) - \hat{T}) + d. \tag{C.77}$$

Plugging in again at $u = 0$ gives $0 = \rho(0) - \ln(\rho(0))(\rho(0) - \hat{T}) + d$. We simply let $\rho(0) = 1$ since any scale can be absorbed into $\phi(\ell)$, so that $d = 1$ [165]. Then finally

$$\frac{u^2}{2} = \rho - \ln(\rho)(\rho(0) - \hat{T}) + 1. \tag{C.78}$$

To find the constant $a = \psi/\phi$, we note that the original equation C.68 implies that

$$\partial_\ell \int_{-\infty}^{\infty} \tilde{\Delta}(u)du = (\hat{T} + \tilde{\Delta}(0))\tilde{\Delta}'\big|_{-\infty}^{\infty} - \tilde{\Delta}'\tilde{\Delta}\big|_{-\infty}^{\infty} = 0 \tag{C.79}$$

where we assume that $\tilde{\Delta}' \to 0$ and $\tilde{\Delta} \to 0$ as $|u| \to \infty$. Therefore $\int \tilde{\Delta} = c$ is a conserved quantity in the first order RG [165]. Since

$$\int_{-\infty}^{\infty} \tilde{\Delta}du = c = \phi/\psi \int_{-\infty}^{\infty} \rho dz, \tag{C.80}$$

we must have that

$$a = \int_{-\infty}^{\infty} \rho dz/c \approx \frac{1.55J^2}{2\pi \int \Delta du} \tag{C.81}$$

where we have input the original physical constants. Note that the numerical integration $\int_{-\infty}^{\infty} \rho \approx 1.55$ has been obtained for $\hat{T} = 0$ [165], and is not exactly true for $\hat{T} > 0$. We only make the approximation here because we are usually dealing with small $\hat{T}$ near 0, so the numerical result still holds.

Appendix D

Appendix to Chapter 5

D.1 Derivation of Energy Barriers for a Cusped Potential

We will derive the energy barriers for generic coupling J_{ij} with $\varphi = 2$ anf stress Σ. We derive it for generic coupling because we need this result to derive the algorithm for coupled sites. We make the assumption that the pinning potential for each site is independent and (fig. 4.5) the same as presented in [11] based on renormalization arguments. Therefore $U_{p,i}(u_i) = U_{p,i}(a_i) - s_{f,i}(a_i - u_i) + \omega_i/2(a_i - u_i)^2$, where $s_{f,i}$ is the failure force, $2a_i$ is the length of the well, and ω_i controls the depth of the well. All three of these numbers $s_{f,i}, a_i, \omega_i$ can be random in the most generic version mean field theory [6]. It is customary to set $s_{f,i}$ to be fixed, although it is easy to change this in the algorithm. The full energy is

$$E = \sum_i U_{p,i}(u_i) + \frac{1}{2}\sum_{i<j} J_{ij}(u_i - u_j)^2 - \Sigma \sum_i u_i. \tag{D.1}$$

Differentiating eq. D.1, we can find the minimum value, which gives the metastable point $u_{m,i}$ for each index i in terms of $\delta s_i(u_i) = s_{f,i} - s_i(u_i)$. Let us first recall the stress equation eq. 4.53 for general J_{ij}

$$s_i(u_i) = \sum_j J_{ij}(u_i - u_j) - \Sigma \tag{D.2}$$

$$s_{f,i} + \omega_i(u_{i,m} - a_i) + \sum_j J_{ij}(u_{i,m} - u_j) - \Sigma = 0 \tag{D.3}$$

$$s_{f,i} + \omega_i(u_{i,m} - a_i) - s_i(u_{i,m}) = 0 \tag{D.4}$$

$$u_{m,i} = a_i - \delta s_i/\omega_i \tag{D.5}$$

where we denote $\delta s_i = \delta s_i(u_{m,i})$. This is the difference between the metastable stress and the failure stress. For cell i, at the top of the barrier, the energy is

$$E_i = \sum_{j\neq i} U(u_j) + U_{p,i}(a_i) + \frac{1}{2}\sum_{j<k,j,k\neq i} J_{jk}(u_j - u_k)^2 + \frac{1}{2}\sum_j J_{ij}(u_j - a_i)^2 - \Sigma\sum_{j\neq i} u_j - \Sigma a_i. \tag{D.6}$$

This gives

$$\Delta E_i = E_i - E = s_f \frac{\delta s_i}{\omega_i} - \frac{(\delta s_i)^2}{2\omega_i} - \frac{\Sigma \delta s_i}{\omega_i} + \frac{1}{2} \sum_{i>j} J_{ij} \left[(u_j - a_i)^2 - (u_j - u_{m,i})^2 \right] \tag{D.7}$$

We have

$$\begin{aligned} (u_j - a_i)^2 - (u_j - u_{m,i})^2 &= -2a_i u_j + a_i^2 + 2u_j u_{m,i} - u_{m,i}^2 \qquad \text{(D.8)} \\ = (2u_j - u_{m,i} - a_i)(u_{m,i} - a_i) &= -(2u_j - u_{m,i} - a_i)\delta s_i / \omega_i \end{aligned}$$

We can then use this result to simplify eq. D.7

$$\sum_j J_{ij} \left[(u_j - a_i)^2 - (u_j - u_{m,i})^2 \right] = \frac{\delta s_i}{\omega_i} \sum_j J_{ij} [(a_i - u_j) + (u_{m,i} - x_j)] \tag{D.9}$$

Using eq. D.5 after adding and subtracting $u_{m,i}$ we have

$$\sum_j J_{ij} \left[(u_j - a_i)^2 - (u_j - u_{m,i})^2 \right] = \frac{\delta s_i}{\omega_i} \sum_j J_{ij} [(u_{m,i} - u_j) + (u_{m,i} - u_j) + \delta s_i / \omega_i] \tag{D.10}$$

$$\sum_j J_{ij} \left[(u_j - a_i)^2 - (u_j - u_{m,i})^2 \right] = \frac{\delta s_i}{\omega_i} 2(\Sigma - s_i) + \frac{\delta s_i^2}{\omega_i^2} \tilde{J} \tag{D.11}$$

where $\tilde{J} = \sum_{j \neq i} J_{ij}$. This gives us

$$\Delta E_i = (s_f - s_i) \frac{\delta s_i}{\omega_i} - \frac{\delta s_i^2}{2\omega_i} + \frac{\tilde{J} \delta s_i^2}{2\omega_i^2} \tag{D.12}$$

$$\Delta E_i = \frac{(\omega + \tilde{J}) \delta s_i^2}{2\omega_i^2} = \Omega_i \delta s_i^2 \tag{D.13}$$

Now if two cells are independent of each other (i.e. $J_{ij} = 0$) fail, then clearly the energy barriers add

$$\Delta E = \Omega_i (\delta s_i)^2 + \Omega_j (\delta s_j)^2. \tag{D.14}$$

Let us analyze what happens in general, when $J_{ij} \neq 0$: Let $S \subseteq \{1, \ldots, N\}$ denote the set of indicies of the n failing cells, so that

$$E = \sum_i U_p(u_i) + \frac{1}{2}\sum_{i>j} J_{ij}(u_i - u_j)^2 - \Sigma \sum_i u_i \tag{D.15}$$

$$\begin{aligned} E_S = \sum_{j\notin S} U(u_j) + \sum_{j\in S} U_p(a_j) + \frac{1}{2}\sum_{j>k,j,k\notin S} J_{jk}(u_j - u_k)^2 + \frac{1}{2}\sum_{j\in S,k\notin S} J_{jk}(a_j - u_k)^2 \\ + \frac{1}{2}\sum_{j>k,j,k\in S} J_{jk}(a_j - a_k)^2 - \Sigma\sum_{i\in S} a_i - \Sigma\sum_{i\notin S} u_i \end{aligned} \tag{D.16}$$

Then subtracting the two terms, we get

$$\begin{aligned} \Delta E_S = \sum_{i\in S}\left(s_f\frac{\delta s_i}{\omega_i} - \frac{(\delta s_i)^2}{2\omega_i} - \frac{\Sigma\delta s_i}{\omega_i}\right) + \frac{1}{2}\sum_{i\in S,j\notin S} J_{ij}[(u_j - a_i)^2 - (u_j - u_i)^2] \\ + \frac{1}{4}\sum_{i,j\in S} J_{ij}[(a_j - a_i)^2 - (u_j - u_i)^2] \end{aligned} \tag{D.17}$$

Note that we have changed from summing over $i > j$ to summing over i, j in the second sum to simplify later expressions. The first sum is invariant to this change since i and j are guaranteed to be unique (since $i \in S, j \notin S$). Then

$$\frac{1}{2}\sum_{i\in S,j\notin S} J_{ij}[(u_j - a_i)^2 - (u_j - u_i)^2] = \frac{1}{2}\sum_{i\in S}\frac{\delta s_i}{\omega_i}\sum_{j\notin S} J_{ij}[(a_i - u_j) + (u_i - u_j)] \tag{D.18}$$

$$\frac{1}{4}\sum_{i,j\in S} J_{ij}[(a_j - a_i)^2 - (u_j - u_i)^2] = \frac{1}{4}\sum_{i,j\in S} J_{ij}[a_j^2 - 2a_j a_i + a_i^2 - u_j^2 + 2u_j u_i - u_i^2]. \tag{D.19}$$

The first sum eq. D.18 is familiar, and is similar to eq. D.11, except that we are summing over $j \notin S$ for each i that is failing. These terms will result in terms similar to eq. D.11. Thus we can write

$$\begin{aligned} \frac{1}{2}\sum_{i\in S,j\notin S} J_{ij}[(u_j - a_i)^2 - (u_j - u_i)^2] + \frac{1}{4}\sum_{i,j\in S} J_{ij}[(a_j - a_i)^2 - (u_j - u_i)^2] = \\ \frac{1}{2}\sum_{i\in S}\frac{\delta s_i}{\omega_i}\sum_{j\notin S} J_{ij}[(a_i - u_j) + (u_i - u_j)] + \frac{1}{4}\sum_{i\in S}\frac{\delta s_i}{\omega_i}\sum_{j\in S} J_{ij}[(a_i - u_j)^2 + (u_i - u_j)^2] \\ + \frac{1}{4}\sum_{i,j\in S} J_{ij}[2a_j u_i + 2a_i u_j - 2u_i u_j - 2a_i a_j] \end{aligned} \tag{D.20}$$

In the second sum on the right hand side of the equal sign, $i, j \in S$, so we can change it so that the sum is not repeating, and combine the two sums so that:

$$\frac{1}{2}\sum_{i\in S}\frac{\delta s_i}{\omega_i}\sum_{j\notin S}J_{ij}[(a_i-u_j)+(u_i-u_j)]+\frac{1}{4}\sum_{i\in S}\frac{\delta s_i}{\omega_i}\sum_{j\in S}J_{ij}[(a_i-u_j)^2+(u_i-u_j)^2]=$$

$$\frac{1}{2}\sum_{i\in S}\frac{\delta s_i}{\omega_i}\sum_{j\neq i}J_{ij}[(a_i-u_j)+(u_i-u_j)] \quad \text{(D.21)}$$

The third sum is

$$\frac{1}{4}\sum_{i,j\in S}J_{ij}[2a_ju_i+2a_iu_j-2u_iu_j-2a_ia_j]=-\frac{1}{2}\sum_{i,j\in S}(a_j-u_j)(a_i-u_i)=-\frac{1}{2}\sum_{i,j\in S}\frac{\delta s_j}{\omega_j}\frac{\delta s_i}{\omega_i}. \quad \text{(D.22)}$$

Combining everything together, we have

$$\Delta E_S=\sum_{i\in S}\Delta E_i-\frac{1}{2}\sum_{i,j\in S}J_{ij}\frac{\delta s_i\delta s_j}{\omega_i\omega_j} \quad \text{(D.23)}$$

$$\Delta E_S=\sum_{i\in S}\frac{\omega_i+\tilde{J}}{2\omega_i^2}\delta s_i^2-\frac{1}{2}\sum_{i,j\in S}J_{ij}\frac{\delta s_i\delta s_j}{\omega_i\omega_j}. \quad \text{(D.24)}$$

Typically, for mean field theory, $\tilde{J}=\mathcal{O}(J_{ij}N)$. Notice that the first term essentially quantifies how large the barrier is if all sites failed individually, while the second sum is essentially a discount because the elastic stiffness pulls the interface together. The second term is of order $\mathcal{O}(1/N)$ in mean field theory. As $N\to\infty$, the second term becomes negligible. This is the expected behavior.

D.2 Algorithm in the Interacting Case

Here we describe how to extend the algorithm to the case of interactions. We take the very simple mean field case with finite size effects. We fix N to be the number of sites, the set of failing sites to be S, with $|S|$ being the number of failing sites. In mean field theory, $J_{ij}=\tilde{J}/N$. To simplify notation, we have set $\lambda_0=1$. The energy barrier

$$\Delta E_S=\Omega\sum_{i=1}^{N}(s_{f,i}-s_i)^2-\tilde{J}/N\sum_{i,j\in\Pi}(s_{f,i}-s_i)(s_{f,j}-s_j). \quad \text{(D.25)}$$

The constant Ω is the same as in eq. 5.23, while $\tilde{J}/N=J$ is of order $\mathcal{O}(1/N)$. Then our previous approach to summing the rate constants will not work, as

$$r_{ij\ldots}\neq\lambda_i\lambda_j\ldots. \quad \text{(D.26)}$$

Also, there is no simple way to factor the interaction

$$\exp\left(\tilde{J}/Nk_BT\sum_{i,j\in S}(s_{f,i}-s_i)(s_{f,j}-s_j)\right) \tag{D.27}$$

so that a product of rate constants remains.

Therefore, we opt for an approximate treatment of this problem. Luckily, since J is of order $1/N$, we can expand

$$\lambda_S = \exp(-\Delta E_S/k_BT) \tag{D.28}$$

$$= \exp\left(-\frac{\Omega}{k_BT}\sum_{i=1}^{N}\delta s_i^2\right)\left(1+\frac{\tilde{J}}{Nk_BT}\sum_{i,j\in S}\delta s_i\delta s_j\right) \tag{D.29}$$

For small T, the exponential term supresses the inaccuracy of this expansion since $\Omega \gg \tilde{J}/N$. For large T, the expansion becomes more accurate, and again since $\Omega \gg \tilde{J}/N$, the approximation term only matters when the expansion is very nearly correct.

As above, we define

$$\sigma_{l,n} = \sum_{i=n}^{N-l+1}\lambda_i\sigma_{l,i+1}. \tag{D.30}$$

In addition, we also define

$$\beta_i = \delta s_i\lambda_i. \tag{D.31}$$

Then the sum of all 1 combinations is again (eq. 5.38)

$$R_1 = \sum_{i=1}^{N-1+1}\lambda_i \tag{D.32}$$

For all single site failures, there is no interaction term, as only one site has failed. However, for $l > 1$ sites, given the set of failed sites S, we must take into account the interaction term. This term includes all pairs of sites in S. The sum of all two combinations is now

$$R_2 = \sum_{i=1}^{N-1}\left(\lambda_i\sigma_{1,i+1} + J\beta_i\gamma_{l,i+1}^{1,2}\right) \tag{D.33}$$

where we have absorbed $\tilde{J}/Nk_BT$ into the definition of J to simplify later expressions and defined

$$\gamma_{1,n}^{1,2} = \sum_{i=n}^{N}\beta_i\sigma_{0,i+1} \tag{D.34}$$

with $\sigma_{0,i+1} = 1$. This takes into account the sum of the interaction terms. The superscript denotes the index of the site we choose. For example, for $\gamma^{1,2}_{l-1,n}$ means we choose the first and second index of the product of rate constants $\lambda_{i_1}\lambda_{i_2}\ldots\lambda_{i_l}$. Then

$$R_l = \sum_{i=0}^{N-l+1}\left(\lambda_i\sigma_{l-1,i+1} + J\beta_i \sum_{m=1,n>m}\gamma^{m,n}_{l-1,i+1} + J\lambda_i \sum_{m>1,n>m}\gamma^{m,n}_{l-1,i+1}\right). \tag{D.35}$$

Naively it would take $\mathcal{O}(Nl^2)$ time to compute each layer, and with N layers, it would take $\mathcal{O}(N^4)$ time. We can simplify things by defining

$$\chi_{l,n} = \sum_{i=n}^{N-l+1}\sum_q \gamma^{1,q}_{l-1,i+1} \tag{D.36}$$

$$\xi_{l,n} = \sum_{i=n}^{N-l+1}\sum_{p,q>1}\gamma^{p,q}_{l-1,i+1} \tag{D.37}$$

$$R_l = \sum_{i=0}^{N-l+1}(\lambda_i\sigma_{l-1,i+1} + J\beta_i\chi_{l-1,i+1} + J\lambda_i\xi_{l-1,i+1}). \tag{D.38}$$

Then along with $\sigma_{l,n}$, $\chi_{l,n}$ and $\xi_{l,n}$ also obey recursion relations of the form

$$\chi_{l,n} = \sum_{i=n}^{N-l+1}\lambda_i\chi_{l-1,i+1} + \sum_{i=n}^{N}\beta_i\sigma_{l-1,i+1} \tag{D.39}$$

$$\xi_{l,n} = \sum_{i=n}^{N-l+1}\beta_i\chi_{l-1,i+1} + \sum_{i=n}^{N}\lambda_i\xi_{l-1,i+1} \tag{D.40}$$

Therefore one can compute the sum again in $\mathcal{O}(N^2)$ time, keeping track of 2 extra variables. In fact, to expand the sum when finding the failing sites, it is convenient to also keep track of

$$\tilde{\sigma}_{l,n} = \sum_{i=n}^{N-l+1}\beta_i\sigma_{l-1,i+1} \tag{D.41}$$

$$\tilde{\chi}_{l,n} = \sum_{i=n}^{N-l+1}\beta_i\chi_{l-1,i+1} \tag{D.42}$$

raising the total to five variables.

To implement the recursive subalgorithm in step 3 of the KMC algorithm, we follow almost exactly the same steps described above. First, we search through $\sum_l R_l$ and find the total number of failed sites ν. The algorithm is modified because we define a matrix of partial sums $\mathbf{S}$. The indices are $S_{k,1} = \sum_{i=1}^k \lambda_i\sigma_{l,i+1}$, $S_{k,2} = \sum_{i=1}^k \lambda_i\chi_{l,i+1}$, $S_{k,3} = \sum_{i=1}^k \lambda_i\xi_{l,i+1}$, $S_{k,4} = \sum_{i=1}^k \beta_i\sigma_{l,i+1}$, and $S_{k,5} = \sum_{i=1}^k \beta_i\chi_{l,i+1}$. Then at each step, we multiply together $\mathbf{S}\vec{\gamma}$ to search for the next index. After the first step $\vec{\gamma}$ is defined as

$[\lambda_{k_1}, J\beta_{k_1}, J\lambda_{k_1}, J\beta_{k_1}, J\lambda_{k_1}]^T$. Subsequently,

$$\vec{\gamma} \leftarrow \begin{bmatrix} \lambda_{k_i}\gamma_0 + \beta_{k_i}\gamma_4 \\ \lambda_{k_i}\gamma_1 + \beta_{k_i}\gamma_4 \\ \lambda_{k_i}\gamma_2 \\ \lambda_{k_i}\gamma_1 + \beta_{k_i}\gamma_4 \\ \lambda_{k_i}\lambda_2^T \end{bmatrix} \tag{D.43}$$

Graphically, fig. D.1 shows the assignment. These assignments follow from the definition of **S**, and any permutation of the columns will also work as long as the assigments are correctly mapped.

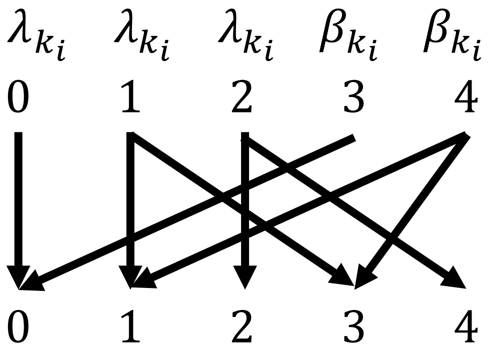

Figure D.1: A graphical representation of the index swapping. This is necessary because of the way the auxiliary variables $\chi_{l,n}$ and $\xi_{l,n}$ were defined. The entire process is a vectorized generalization of the simpler algorithm presented in the main work. The upper indices $\{0, 1, 2, 3, 4\}$ represent the initial values of $\vec{\gamma}$. The upper values λ_{k_i} and β_{k_i} represent multipliers of these values. The lower indices represent the updated values of $\vec{\gamma}$.

Appendix E

Appendix to Chapter 6

E.1 The distribution of stresses

From [7], the distribution of stress for a given site is

$$p(s|s_a) = \frac{1}{s_m - s_a} \quad \text{for} \quad s_a \le s \le s_m \tag{E.1}$$

where s_m is the maximum stress and s_a is the arrest stress of that cell. We denote the distribution of arrest stresses as $\rho(s_a)$ and assume that it has zero mean and variance $\langle s_a^2 \rangle \ll s_m^2$. We also assume that the arrest stress has a finite width W, so $\langle s_a^2 \rangle \sim W^2$ which implies $W \ll s_a$. The distribution of stresses over the entire system is therefore

$$p(s) = \int_{-W/2}^{s} ds_a p(s|s_a)\rho(s_a) \tag{E.2}$$

$$p(s) = \begin{cases} f(s) = \int_{-W/2}^{s} ds_a \frac{\rho(s_a)}{s_m - s_a}, & \text{for } -W/2 \le s < W/2 \\ \bar{p} = \langle (s_m - s_a)^{-1} \rangle, & \text{for } W/2 \le s \le s_m \end{cases}$$

where the angular brackets denote averaging with respect to the arrest stress. The constant $\bar{p}$ can be evaluated by expansion as

$$\bar{p} = \int_{-W/2}^{W/2} \frac{ds_a \rho(s_a)}{s_m - s_a} \tag{E.3}$$

$$= \frac{1}{s_m} \int_{-W/2}^{W/2} \frac{ds_a \rho(s_a)}{1 - s_a/s_m} \approx \frac{1}{s_m} \int_{-W/2}^{W/2} ds_a \rho(s_a) \left[1 + \frac{s_a}{s_m} + \frac{s_a^2}{s_m^2} \right] \tag{E.4}$$

$$= \frac{1}{s_m} \left[1 + \frac{\langle s_a \rangle}{s_m} + \frac{\langle s_a^2 \rangle}{s_m^2} \right] = \frac{1}{s_m} + \frac{\langle s_a^2 \rangle}{s_m^3} \tag{E.5}$$

which is approximately $\bar{p} \approx s_m^{-1}$ since $\langle s_a^2 \rangle \ll s_m^2$.

E.1.1 Variance of stresses

The stress on a specific site after a number of iterations is the sum of its arrest stress and the stress redistributed to it by other failing sites. Therefore, to calculate the variance, we define a new variable $\Delta s_i = s_f - s_{a,i}$. Δs_i is used to determine the amount of stress site i redistributes onto all other sites. Note that we no longer assume that $s_0 > s_1 > \ldots > s_{N-1}$, as we will need to keep track of each stress to calculuate the variance. Let $s_{max,i}$ be stress of site i when it is the maximum stress in the system. Then $s_{max,i}$ is determined by the initial arrest stress together with the contribution of all other Δs_j that have failed:

$$s_{max,i}(t) = s_{a,i}(t) + \sum_{j \neq i}^{R_{i,t}} \frac{\Delta s_j}{N}. \tag{E.6}$$

Here $R_{i,t}$ is a random variable which determines the number of iterations a site waits in order to become the site with the maximum stress starting from the arrest stress. It is reasonable that $R_{i,t} = R_i$ relaxes to a stationary process after many iterations for each stress. Then the variance is

$$\mathrm{var}(s_{max,i}(t)) = \mathrm{var}(s_{a,i}) + \mathrm{var}\left(\sum_{j \neq i}^{R_i} \frac{\Delta s_j}{N}\right) + 2\mathrm{cov}\left(\sum_{j \neq i}^{R_i} \frac{\Delta s_j}{N}, s_{a,i}\right) \tag{E.7}$$

To evaluate the variance of a random sum of random variables, we rely on the conditional expectation

$$\mathrm{var}\left(\sum_{j \neq i}^{R_i} \frac{\Delta s_j}{N} \middle| R_i = r\right) = r\mathrm{var}\left(\frac{\Delta s_j}{N}\right) + (r^2 - \langle R_i \rangle^2)\left\langle \frac{\Delta s_j}{N} \right\rangle^2 \tag{E.8}$$

$$\mathrm{var}\left(\sum_{j \neq i}^{R_i} \frac{\Delta s_j}{N}\right) = \langle R_i \rangle \mathrm{var}\left(\frac{\Delta s_j}{N}\right) + \mathrm{var}(R_i)\left\langle \frac{\Delta s_j}{N} \right\rangle^2. \tag{E.9}$$

Similarly, the covariance can be handled by conditional expectation on both R_i and $s_{a,i}$, so that

$$\mathrm{cov}\left(\sum_{j \neq i}^{R_i} \frac{\Delta s_j}{N}, s_{a,i} \middle| R = r, s_{a,i} = s\right) = rs\left\langle \frac{\Delta s_j}{N} \right\rangle - \langle R_i \rangle \langle s_{a,i} \rangle \left\langle \frac{\Delta s_j}{N} \right\rangle \tag{E.10}$$

$$\mathrm{cov}\left(\sum_{j \neq i}^{R_i} \frac{\Delta s_j}{N}, s_{a,i}\right) = \mathrm{cov}(R_i, s_{a,i})\left\langle \frac{\Delta s_j}{N} \right\rangle \tag{E.11}$$

where we have used that Δs_i is an independent identically distributed variable for each i, and $s_{a,i}$ is an independent identitically distributed variable for each i. Finally, we have also used that R_i is independent of each Δs_i. Then the problem is essentially to compute each of these variances and covariances separately.

First

$$\mathrm{var}\left(\frac{\Delta s_j}{N}\right) = \frac{\mathrm{var}(s_a)}{N^2}, \tag{E.12}$$

where we have removed the index j since the variables are identically distributed. Second, we know that a site that starts with a large arrest stress has fewer steps to the maximum stress. Therefore

$$R_i = N\frac{s_m}{s_f} - N\frac{s_{a,i}}{s_f} + \xi. \tag{E.13}$$

Here the term ξ is a random variable. In the mean field model, the only time that a given site can skip its position when ordered sequentially (so $s_0 > s_1 > \ldots > s_{N-1}$) is if the stress is in the arrest stress portion of the distribution, so $s \in [-W/2, W/2]$. In this case another site can fail with arrest stress higher than the current site. Therefore, the random variable ξ represents how many places the given site has been skipped or has skipped other sites. For any given distribution, the probability that $P(s_{a,i} > s_{a,j}) = 1/2$. Each skip is a Bernoulli random variable, so it has variance $1/4$, and on average each site has to travel $NW/2s_f$ steps. Therefore,

$$\mathrm{var}(\xi) \approx \frac{NW}{8s_f} \tag{E.14}$$

This gives us

$$\mathrm{var}(R_i) = \frac{N^2}{s_f^2}\mathrm{var}(s_a) + \frac{NW}{8s_f} \tag{E.15}$$

$$\mathrm{cov}(R_i, s_{a,i}) = -\frac{N}{s_f}\mathrm{var}(s_a). \tag{E.16}$$

Combining these equations together and plugging into eq. E.7, we get

$$\sigma^2 = \mathrm{var}(s_{max,i}(t)) = 2\mathrm{var}(s_a) + \frac{s_f^2}{N^2}\frac{NW}{8s_f} - 2\mathrm{var}(s_a) \tag{E.17}$$

$$\sigma^2 = \frac{Ws_f}{8N} \tag{E.18}$$

E.1.2 Mean energy difference

We define $\Delta E_0 < \Delta E_1 < \ldots < \Delta E_{N-1}$. Each $\Delta E_i = (s_f - s_i)^2$, so when we expand

$$\Delta E_i = s_f^2 - 2s_f s_i + s_i^2. \tag{E.19}$$

Each s_i is normally distributed with mean μ_i and variance σ^2. We have found empirically that σ^2 is constant for $i \ll N$. If we let ξ be a standard normal distribution with zero mean and variance σ^2, then $s_i = \mu_i + \sigma\xi$. Then expanding

$$\Delta E_i/\Omega = s_f^2 - 2s_f\mu_i - 2(s_f - \mu_i)\sigma\xi + \mu_i^2 + \sigma^2\xi^2 \tag{E.20}$$

From eq. **??** in the supplementary, we can find expressions for μ_i so

$$\langle \Delta E_i - \Delta E_{i+1}\rangle = \Omega(2s_f(\mu_{i+1} - \mu_i) + \mu_i^2 - \mu_{i+1}^2) \tag{E.21}$$

$$= \Omega(4s_f\Sigma/N - 8\Sigma^2 i/N) + \mathcal{O}(1/N^2) \tag{E.22}$$

$$\approx 8\Omega F(\Sigma_c - \Sigma)/N = 8\Omega F^2\frac{\Delta\Sigma}{N\Sigma} = 2E_0\frac{\Sigma\Delta\Sigma}{N\Sigma_c^2}. \tag{E.23}$$

E.2 Saddle point approximations

Here we give details about the saddle point analysis of equations 8 and 11 in the main text.

E.2.1 Low Temperature

Set $\Omega = \lambda_0 = 1$ for simplicity. Let $f(s)$ be be the argument of the exponential

$$f(s) = \frac{(s_m - \mu)^2}{2\sigma^2} + \frac{(s_f - s_m)^2}{T} + \Delta t \exp(-(s_f - s_m)^2/T) \tag{E.24}$$

Shift variables so that $u = (s_f - s_m)/\sqrt{T}$ and define $\Delta f = 2\Delta\Sigma/\sqrt{T}$, where we have used that $\mu = 2F$ and $s_f = 2F_c$. The saddle point equation is $f'(u) = 0$ or

$$\alpha(u - \Delta f) + u = \Delta t u e^{-u^2}. \tag{E.25}$$

We have set $\alpha = T/2\sigma^2$. Note the limits of integration now go between 0 and $s_f/\sqrt{T}$. We can expand in powers of $\alpha\Delta f$, which we denote $u_0, u_1, \ldots$, so to zeroth order we have:

$$u_0 = \log\left(\frac{\Delta t}{\alpha + 1}\right). \tag{E.26}$$

The first order term is

$$u_1 = \frac{\alpha\Delta f}{2(1+\alpha)u_0}, \tag{E.27}$$

and the second order term is

$$u_2 = \frac{\alpha^2 \Delta f^2(-3 + 2u_0)}{8(1+\alpha)^2 u_0^2}. \tag{E.28}$$

Expanding the argument of the exponential to second order we have

$$f(u) \approx (1+\alpha)\left(1+u_0^2\right) - 2\alpha\Delta f u_0 + \frac{\Delta f^2 \alpha(2 + 2\alpha - \alpha/u_0)}{2(1+\alpha)}. \tag{E.29}$$

Then we exponentiate this so

$$p(\Delta t) \sim \left(\frac{1+\alpha}{\Delta t}\right)^{1+\alpha} \exp\left(-1 - \alpha + \alpha\Delta f\left(2\sqrt{\log\left(\frac{\Delta t}{\alpha+1}\right)} - \Delta f\right) + \mathcal{O}(\Delta f^2\alpha^2/\log(\Delta t))\right) \tag{E.30}$$

Plugging in this form into the original equation, we can see that equation 6.10 in the main text emerges. We take into account the Gaussian integral as well:

$$f''(u) = \alpha + 1 - \Delta t e^{-u^2/T} + \frac{2\Delta t}{T} u^2 e^{-u^2/T} \tag{E.31}$$

$$f''(u) = -\frac{\alpha\Delta f}{u} + 2(\alpha+1)u^2 - 2\alpha\Delta f u \approx \mathcal{O}(\Delta f^2 \alpha^2 u_0^{-2}) \tag{E.32}$$

$$\sqrt{\frac{2\pi}{f''(u)}} = \mathcal{O}(u_0/\Delta f\alpha) = \mathcal{O}(\log(\Delta t)) \tag{E.33}$$

which is a logarithmic correction.

E.2.2 High Temperature

In the high temperature regime we have from equation 11 in the main text, the integral

$$p(\Delta t) = \frac{1}{\sqrt{2\pi\sigma_E^2}} \int \exp\left(-E/T - (E-\mu_E)^2/(2\sigma_E^2) - \Delta t e^{-E/T}\right) \tag{E.34}$$

which yields the saddle point equation

$$\Delta t e^{-E/T} = 1 + \frac{T}{\sigma_E^2}(E - \mu_E) \tag{E.35}$$

which upon substitution of $y = E/T - \mu/T + \sigma^2/T^2$ yields the solution

$$y = W\left(\Delta t e^{-\mu_E/T + \sigma_E^2/T} \frac{\sigma_E^2}{T^2}\right) = W(z) \tag{E.36}$$

where $W(z)$ is the Lambert-W function and $z = \Delta t e^{-\mu_E/T+\sigma_E^2/T^2}\sigma_E^2/T^2$. The Gaussian correction is

$$1/\sqrt{\Delta t_0^2(1+W(z))} \tag{E.37}$$

Plugging all of this into the integral we have

$$p(\Delta t) = \frac{1}{\Delta t_0\sqrt{1+W(z)}}\left(\frac{W(z)}{z}\right)^{T^2/\sigma_E^2} e^{-\frac{T^2}{2\sigma_E^2}W(z)^2-\frac{\mu_E}{T}+\frac{\sigma_E^2}{2T^2}} \tag{E.38}$$

where we used the identity $e^{-aW(z)} = (W(z)/z)^a$.

E.3 Plausibility argument that $p(\Delta t_M)$ scales like $p(\Delta t)$

It is plausible that $p(\Delta t_M)$ scales similarly to $p(\Delta t)$. First take the complementary cumulative distribution $P(\Delta t_i > \Delta t) \sim \Delta t^{-\alpha}$ of each interevent time. We have $\Delta t_i < \Delta t_M$, and hence $P(\Delta t_i > \Delta t) < P(\Delta t_M > \Delta t)$. Similarly, if all of $\Delta t_i < \Delta t/M$, then $\Delta t_M < \Delta t$, so $\sum_i P(\Delta t_i < \Delta t/M) \sim \Delta t^{-\alpha} < P(\Delta t_M < \Delta t)$ (by independence of each Δt_i). We can convert this so that $\sum_i(1 - P(\Delta t_i > \Delta t/M)) < 1 - P(\Delta t_M > \Delta t)$ so that $P(\Delta t_M > \Delta t) < \sum_i P(\Delta t_i > \Delta t/M) \sim \Delta t^{-\alpha}$. Hence $C_1\Delta t^{-\alpha} < P(\Delta t_M > \Delta t) < C_2\Delta t^{-\alpha}$ for large Δt, so $p(\Delta t_M) \sim \Delta t_M^{-1-\alpha}$. In Fig. 4, the angular brackets denote the mean number of steps taken for each of the thresholds set. We see that the interevent time distribution does not change near the tail of the distribution regardless of the threshold set. In particular, the exponential term in eq. 6.10 does not seem to cause huge deviation as more interevent times are summed together.

References

[1] James P. Sethna, Karin A. Dahmen, and Christopher R. Myers. Crackling noise. *Nature*, 410(6825):242–250, March 2001.

[2] Olga Perkovi, Karin Dahmen, and James P. Sethna. Avalanches, Barkhausen Noise, and Plain Old Criticality. *Physical Review Letters*, 75(24):4528–4531, December 1995.

[3] Stefano Zapperi, Pierre Cizeau, Gianfranco Durin, and H. Eugene Stanley. Dynamics of a ferromagnetic domain wall: Avalanches, depinning transition, and the Barkhausen effect. *Physical Review B*, 58(10):6353–6366, September 1998.

[4] Stefanos Papanikolaou, Felipe Bohn, Rubem Luis Sommer, Gianfranco Durin, Stefano Zapperi, and James P. Sethna. Universality beyond power laws and the average avalanche shape. *Nature Physics*, 7(4):316–320, April 2011.

[5] Edward T. Lu and Russell J. Hamilton. Avalanches and the distribution of solar flares. *The Astrophysical Journal Letters*, 380:L89–L92, October 1991.

[6] Daniel S. Fisher, Karin Dahmen, Sharad Ramanathan, and Yehuda Ben-Zion. Statistics of Earthquakes in Simple Models of Heterogeneous Faults. *Physical Review Letters*, 78(25):4885–4888, June 1997.

[7] Karin Dahmen, Deniz Ertas, and Yehuda Ben-Zion. Gutenberg-Richter and characteristic earthquake behavior in simple mean-field models of heterogeneous faults. *Physical Review E*, 58(2):1494–1501, August 1998.

[8] Deniz Erta and Mehran Kardar. Anisotropic Scaling in Depinning of a Flux Line. *Physical Review Letters*, 73(12):1703–1706, September 1994.

[9] Stuart Field, Jeff Witt, Franco Nori, and Xinsheng Ling. Superconducting Vortex Avalanches. *Physical Review Letters*, 74(7):1206–1209, February 1995.

[10] Onuttom Narayan and Daniel S. Fisher. Critical behavior of sliding charge-density waves in 4-ϵ dimensions. *Physical Review B*, 46(18):11520–11549, November 1992.

[11] Onuttom Narayan and Daniel S. Fisher. Threshold critical dynamics of driven interfaces in random media. *Physical Review B*, 48(10):7030–7042, September 1993.

[12] Semjon Stepanow, Thomas Nattermann, Lei-Han Tang, and Heiko Leschhorn. Dynamics of Interface Depinning in a Disordered Medium. In Y. Rabin and R. Bruinsma, editors, *Soft Order in Physical Systems*, NATO ASI Series, pages 155–158. Springer US, Boston, MA, 1994.

[13] Karin A. Dahmen, Yehuda Ben-Zion, and Jonathan T. Uhl. Micromechanical Model for Deformation in Solids with Universal Predictions for Stress-Strain Curves and Slip Avalanches. *Physical Review Letters*, 102(17):175501, April 2009.

[14] Nir Friedman, Andrew T. Jennings, Georgios Tsekenis, Ju-Young Kim, Molei Tao, Jonathan T. Uhl, Julia R. Greer, and Karin A. Dahmen. Statistics of Dislocation Slip Avalanches in Nanosized Single Crystals Show Tuned Critical Behavior Predicted by a Simple Mean Field Model. *Physical Review Letters*, 109(9):095507, August 2012.

[15] James Antonaglia, Wendelin J. Wright, Xiaojun Gu, Rachel R. Byer, Todd C. Hufnagel, Michael LeBlanc, Jonathan T. Uhl, and Karin A. Dahmen. Bulk Metallic Glasses Deform via Slip Avalanches. *Physical Review Letters*, 112(15):155501, April 2014.

[16] James P. Sethna, Karin Dahmen, Sivan Kartha, James A. Krumhansl, Bruce W. Roberts, and Joel D. Shore. Hysteresis and hierarchies: Dynamics of disorder-driven first-order phase transformations. *Physical Review Letters*, 70(21):3347–3350, May 1993.

[17] Daniel S. Fisher. Collective transport in random media: from superconductors to earthquakes. *Physics Reports*, 301(13):113–150, July 1998.

[18] Matthew C. Kuntz and James P. Sethna. Noise in disordered systems: The power spectrum and dynamic exponents in avalanche models. *Physical Review B*, 62(17):11699–11708, November 2000.

[19] Leo P. Kadanoff. Scaling Laws for Ising Models Near T_c. *Physics Physique Fizika*, 2(6):263–272, June 1966.

[20] Kenneth G. Wilson. The renormalization group: Critical phenomena and the Kondo problem. *Reviews of Modern Physics*, 47(4):773–840, October 1975.

[21] Karin Dahmen and James P. Sethna. Hysteresis loop critical exponents in $6 - \epsilon$ dimensions. *Physical Review Letters*, 71(19):3222–3225, November 1993.

[22] Karin Dahmen and James P. Sethna. Hysteresis, avalanches, and disorder-induced critical scaling: A renormalization-group approach. *Physical Review B*, 53(22):14872–14905, June 1996.

[23] Jrme Weiss and Jean-Robert Grasso. Acoustic Emission in Single Crystals of Ice. *The Journal of Physical Chemistry B*, 101(32):6113–6117, August 1997.

[24] M.-Carmen Miguel, Alessandro Vespignani, Stefano Zapperi, Jrme Weiss, and Jean-Robert Grasso. Intermittent dislocation flow in viscoplastic deformation. *Nature*, 410(6829):667–671, April 2001.

[25] Karin A. Dahmen, Yehuda Ben-Zion, and Jonathan T. Uhl. A simple analytic theory for the statistics of avalanches in sheared granular materials. *Nature Physics*, 7(7):554–557, July 2011.

[26] James Antonaglia, Xie Xie, Gregory Schwarz, Matthew Wraith, Junwei Qiao, Yong Zhang, Peter K. Liaw, Jonathan T. Uhl, and Karin A. Dahmen. Tuned Critical Avalanche Scaling in Bulk Metallic Glasses. *Scientific Reports*, 4:4382, March 2014.

[27] L. B. Ioffe and V. M. Vinokur. Dynamics of interfaces and dislocations in disordered media. *Journal of Physics C: Solid State Physics*, 20(36):6149, 1987.

[28] G. Tsekenis, J. T. Uhl, N. Goldenfeld, and K. A. Dahmen. Determination of the universality class of crystal plasticity. *EPL (Europhysics Letters)*, 101(3):36003, 2013.

[29] Frans Spaepen. A microscopic mechanism for steady state inhomogeneous flow in metallic glasses. *Acta Metallurgica*, 25(4):407–415, April 1977.

[30] A. S Argon. Plastic deformation in metallic glasses. *Acta Metallurgica*, 27(1):47–58, January 1979.

[31] A. S. Argon. Strain avalanches in plasticity. *Philosophical Magazine*, 93(28-30):3795–3808, September 2013.

[32] B. Widom. Surface Tension and Molecular Correlations near the Critical Point. *The Journal of Chemical Physics*, 43(11):3892–3897, December 1965.

[33] F. R. N. Nabarro. Dislocations in a simple cubic lattice. *Proceedings of the Physical Society*, 59(2):256, 1947.

[34] D. G Morris, C. T Liu, and E. P George. Pinning of dislocations and the origin of the stress anomaly in FeAl alloys. *Intermetallics*, 7(9):1059–1068, September 1999.

[35] Pak Yuen Chan, Georgios Tsekenis, Jonathan Dantzig, Karin A. Dahmen, and Nigel Goldenfeld. Plasticity and Dislocation Dynamics in a Phase Field Crystal Model. *Physical Review Letters*, 105(1):015502, June 2010.

[36] Georgios Tsekenis, Nigel Goldenfeld, and Karin A. Dahmen. Dislocations Jam at Any Density. *Physical Review Letters*, 106(10):105501, March 2011.

[37] K. Morii, H. Mecking, and Y. Nakayama. Development of shear bands in f.c.c. single crystals. *Acta Metallurgica*, 33(3):379–386, March 1985.

[38] James P. Sethna, Matthew K. Bierbaum, Karin A. Dahmen, Carl P. Goodrich, Julia R. Greer, Lorien X. Hayden, Jaron P. Kent-Dobias, Edward D. Lee, Danilo B. Liarte, Xiaoyue Ni, and et. al. Deformation of Crystals: Connections with Statistical Physics. *Annual Review of Materials Research*, 47(1):217–246, 2017.

[39] Stefano Zapperi and Michael Zaiser. Depinning of a dislocation: the influence of long-range interactions. *Materials Science and Engineering: A*, 309-310:348–351, July 2001.

[40] Georgios Tsekenis. *Plasticity as a Depinning Phase Transition.* PhD thesis, University of Illinois at Urbana-Champaign, 2012.

[41] Michael Zaiser. Scale invariance in plastic flow of crystalline solids. *Advances in Physics*, 55(1-2):185–245, January 2006.

[42] Christopher A. Schuh, Todd C. Hufnagel, and Upadrasta Ramamurty. Mechanical behavior of amorphous alloys. *Acta Materialia*, 55(12):4067–4109, July 2007.

[43] M. L. Falk and J. S. Langer. Dynamics of viscoplastic deformation in amorphous solids. *Physical Review E*, 57(6):7192–7205, June 1998.

[44] B.S.S. Daniel, A. Reger-Leonhard, M. Heilmaier, J. Eckert, and L. Schultz. Thermal Relaxation and High Temperature Creep of Zr55cu30al10ni5 Bulk Metallic Glass. *Mechanics of Time-Dependent Materials*, 6(2):193–206, June 2002.

[45] Marc Heggen, Frans Spaepen, and Michael Feuerbacher. Creation and annihilation of free volume during homogeneous flow of a metallic glass. *Journal of Applied Physics*, 97(3):033506, December 2004.

[46] X. L. Fu, Y. Li, and C. A. Schuh. Contributions to the homogeneous plastic flow of in situ metallic glass matrix composites. *Applied Physics Letters*, 87(24):241904, December 2005.

[47] W. L. Johnson and K. Samwer. A Universal Criterion for Plastic Yielding of Metallic Glasses with a $(T/T_g)^{2/3}$ Temperature Dependence. *Physical Review Letters*, 95(19):195501, November 2005.

[48] D. Pan, A. Inoue, T. Sakurai, and M. W. Chen. Experimental characterization of shear transformation zones for plastic flow of bulk metallic glasses. *Proceedings of the National Academy of Sciences*, 105(39):14769–14772, September 2008.

[49] Mareike Zink, K. Samwer, W. L. Johnson, and S. G. Mayr. Plastic deformation of metallic glasses: Size of shear transformation zones from molecular dynamics simulations. *Physical Review B*, 73(17):172203, May 2006.

[50] Peter Schall, David A. Weitz, and Frans Spaepen. Structural Rearrangements That Govern Flow in Colloidal Glasses. *Science*, 318(5858):1895–1899, December 2007.

[51] Eric R. Homer and Christopher A. Schuh. Mesoscale modeling of amorphous metals by shear transformation zone dynamics. *Acta Materialia*, 57(9):2823–2833, May 2009.

[52] John Douglas Eshelby. The elastic field outside an ellipsoidal inclusion. *Proc. R. Soc. Lond. A*, 252(1271):561–569, October 1959.

[53] S. F. Edwards and P. W. Anderson. Theory of spin glasses. *Journal of Physics F: Metal Physics*, 5(5):965, 1975.

[54] Jonathan T. Uhl, Shivesh Pathak, Danijel Schorlemmer, Xin Liu, Ryan Swindeman, Braden A. W. Brinkman, Michael LeBlanc, Georgios Tsekenis, Nir Friedman, Robert Behringer, Dmitry Denisov, Peter Schall, Xiaojun Gu, Wendelin J. Wright, Todd Hufnagel, Andrew Jennings, Julia R. Greer, P. K. Liaw, Thorsten Becker, Georg Dresen, and Karin A. Dahmen. Universal Quake Statistics: From Compressed Nanocrystals to Earthquakes. *Scientific Reports*, 5:16493, November 2015.

[55] Yehuda BenZion and James R. Rice. Earthquake failure sequences along a cellular fault zone in a three-dimensional elastic solid containing asperity and nonasperity regions. *Journal of Geophysical Research: Solid Earth*, 98(B8):14109–14131, August 1993.

[56] D. Schorlemmer, S. Wiemer, and M. Wyss. Earthquake statistics at Parkfield: 1. Stationarity of b values. *Journal of Geophysical Research: Solid Earth*, 109(B12), December 2004.

[57] Danijel Schorlemmer, Stefan Wiemer, and Max Wyss. Variations in earthquake-size distribution across different stress regimes. *Nature*, 437(7058):539–542, September 2005.

[58] Hiroyuki Maehara, Takuya Shibayama, Shota Notsu, Yuta Notsu, Takashi Nagao, Satoshi Kusaba, Satoshi Honda, Daisaku Nogami, and Kazunari Shibata. Superflares on solar-type stars. *Nature*, 485(7399):478–481, May 2012.

[59] Mohammed A. Sheikh, Richard L. Weaver, and Karin A. Dahmen. Avalanche Statistics Identify Intrinsic Stellar Processes near Criticality in KIC 8462852. *Phys. Rev. Lett.*, 117(26):261101, December 2016.

[60] T. S. Boyajian, D. M. LaCourse, S. A. Rappaport, D. Fabrycky, D. A. Fischer, D. Gandolfi, G. M. Kennedy, H. Korhonen, M. C. Liu, A. Moor, and et. al. Planet Hunters IX. KIC 8462852 where's the flux? *Monthly Notices of the Royal Astronomical Society*, 457(4):3988–4004, April 2016.

[61] Subrahmanyan Chandrasekhar. *An introduction to the study of stellar structure*. The University of Chicago Press, 1939.

[62] Henry Norris Russell. Relations Between the Spectra and Other Characteristics of the Stars. *Popular Astronomy*, 22:275–294, May 1914.

[63] Richard Powell. HertzsprungRussell diagram.

[64] S. Mathur, R. A. Garca, J. Ballot, T. Ceillier, D. Salabert, T. S. Metcalfe, C. Rgulo, A. Jimnez, and S. Bloemen. Magnetic activity of F stars observed by *Kepler*. *Astronomy & Astrophysics*, 562:A124, February 2014.

[65] A. Bonanno, H.-E. Frhlich, C. Karoff, M. N. Lund, E. Corsaro, and A. Frasca. Magnetic activity, differential rotation, and dynamo action in the pulsating F9iv star KIC 5955122. *Astronomy & Astrophysics*, 569:A113, September 2014.

[66] Michele Johnson. Liftoff of the Kepler spacecraft, April 2015.

[67] Suzanne L. Hawley, James R. A. Davenport, Adam F. Kowalski, John P. Wisniewski, Leslie Hebb, Russell Deitrick, and Eric J. Hilton. Kepler Flares. I. Active and Inactive M Dwarfs. *The Astrophysical Journal*, 797(2):121, 2014.

[68] James R. A. Davenport, Suzanne L. Hawley, Leslie Hebb, John P. Wisniewski, Adam F. Kowalski, Emily C. Johnson, Michael Malatesta, Jesus Peraza, Marcus Keil, Steven M. Silverberg, and et. al. Kepler Flares. II. The Temporal Morphology of White-light Flares on GJ 1243. *The Astrophysical Journal*, 797(2):122, 2014.

[69] Jim Fuller, Matteo Cantiello, Dennis Stello, Rafael A. Garcia, and Lars Bildsten. Asteroseismology can reveal strong internal magnetic fields in red giant stars. *Science*, 350(6259):423–426, October 2015.

[70] A. Alan Middleton and Daniel S. Fisher. Critical behavior of charge-density waves below threshold: Numerical and scaling analysis. *Physical Review B*, 47(7):3530–3552, February 1993.

[71] Theodore E. Harris. *The Theory of Branching Processes*. Springer, 1963. pg. 32.

[72] Pascal Chauve and Pierre Le Doussal. Exact multilocal renormalization group and applications to disordered problems. *Physical Review E*, 64(5):051102, October 2001.

[73] Amit P. Mehta, Andrea C. Mills, Karin A. Dahmen, and James P. Sethna. Universal pulse shape scaling function and exponents: Critical test for avalanche models applied to Barkhausen noise. *Physical Review E*, 65(4):046139, April 2002.

[74] Pierre Le Doussal. Exact results and open questions in first principle functional RG. *Annals of Physics*, 325(1):49–150, January 2010.

[75] Pierre Le Doussal and Kay Jrg Wiese. Avalanche dynamics of elastic interfaces. *Physical Review E*, 88(2):022106, August 2013.

[76] Alexander Dobrinevski, Pierre Le Doussal, and Kay Jrg Wiese. Avalanche shape and exponents beyond mean-field theory. *EPL (Europhysics Letters)*, 108(6):66002, 2014.

[77] Nigel Goldenfeld. *Lectures On Phase Transitions And The Renormalization Group*. CRC Press, March 2018.

[78] Bertrand Delamotte. An Introduction to the Nonperturbative Renormalization Group. In Achim Schwenk and Janos Polonyi, editors, *Renormalization Group and Effective Field Theory Approaches to Many-Body Systems*, Lecture Notes in Physics, pages 49–132. Springer Berlin Heidelberg, Berlin, Heidelberg, 2012.

[79] A. I. Larkin. Effect of Inhomogeneities on the Structure of the Mixed State of Superconductors. *Zh. Eksp. Theor. Fiz. 58: 1466-70(Apr 1970).*, January 1970.

[80] Yoseph Imry and Shang-keng Ma. Random-Field Instability of the Ordered State of Continuous Symmetry. *Physical Review Letters*, 35(21):1399–1401, November 1975.

[81] Claus Fröhlich, Bo N. Andersen, Thierry Appourchaux, Gabrielle Berthomieu, Dominique A. Crommelynck, Vicente Domingo, Alain Fichot, Wolfgang Finsterle, Maria F. Gomez, Douglas Gough, and et. al. First Results from VIRGO, the Experiment for Helioseismology and Solar Irradiance Monitoring on SOHO. *Solar Physics*, 170:1–25, 1997.

[82] M. V. Feigelman, V. B. Geshkenbein, A. I. Larkin, and V. M. Vinokur. Theory of collective flux creep. *Physical Review Letters*, 63(20):2303–2306, November 1989.

[83] G. Blatter, M. V. Feigel'man, V. B. Geshkenbein, A. I. Larkin, and V. M. Vinokur. Vortices in high-temperature superconductors. *Reviews of Modern Physics*, 66(4):1125–1388, October 1994.

[84] Valerii M. Vinokur, M. Cristina Marchetti, and Lee-Wen Chen. Glassy Motion of Elastic Manifolds. *Physical Review Letters*, 77(9):1845–1848, August 1996.

[85] Pascal Chauve, Thierry Giamarchi, and Pierre Le Doussal. Creep and depinning in disordered media. *Physical Review B*, 62(10):6241–6267, September 2000.

[86] A. H Clauer, B. A Wilcox, and J. P Hirth. Creep behavior of molybdenum single crystals. *Acta Metallurgica*, 18(3):367–379, March 1970.

[87] D. Ftay, J. Gubicza, and J. Lendvai. Indentation creep behavior of a Zr-based bulk metallic glass. *Journal of Alloys and Compounds*, 434-435:75–78, May 2007.

[88] Jon-Olaf Krisponeit, Sebastian Pitikaris, Karina E. Avila, Stefan Kchemann, Antje Krger, and Konrad Samwer. Crossover from random three-dimensional avalanches to correlated nano shear bands in metallic glasses. *Nature Communications*, 5:ncomms4616, April 2014.

[89] Michael E. Kassner, Kamia Smith, and Veronica Eliasson. Creep in amorphous metals. *Journal of Materials Research and Technology*, 4(1):100–107, January 2015.

[90] Carlos Herrero-Gmez and Konrad Samwer. Stress and temperature dependence of the avalanche dynamics during creep deformation of metallic glasses. *Scientific Reports*, 6:33503, September 2016.

[91] William J. Borucki, David Koch, Gibor Basri, Natalie Batalha, Timothy Brown, Douglas Caldwell, John Caldwell, Jrgen Christensen-Dalsgaard, William D. Cochran, Edna DeVore, and et. al. Kepler Planet-Detection Mission: Introduction and First Results. *Science*, 327(5968):977–980, February 2010.

[92] A. S. Baran, S. Zola, A. Blokesz, R. H. stensen, and R. Silvotti. Detection of a planet in the sdB + M dwarf binary system 2m 1938+4603. *Astronomy & Astrophysics*, 577:A146, May 2015.

[93] Gibor Basri, Lucianne M. Walkowicz, Natalie Batalha, Ronald L. Gilliland, Jon Jenkins, William J. Borucki, David Koch, Doug Caldwell, Andrea K. Dupree, David W. Latham, Sren Meibom, Steve Howell, and Tim Brown. Photometric Variability in Kepler Target Stars: The Sun Among Starsa First Look. *The Astrophysical Journal Letters*, 713(2):L155, 2010.

[94] W. J. Chaplin, H. Kjeldsen, J. Christensen-Dalsgaard, S. Basu, A. Miglio, T. Appourchaux, T. R. Bedding, Y. Elsworth, R. A. Garca, and R. L. et. al. Gilliland. Ensemble Asteroseismology of Solar-Type Stars with the NASA Kepler Mission. *Science*, 332(6026):213–216, April 2011.

[95] Ersin G, Peter M. Woods, Chryssa Kouveliotou, Jan van Paradijs, Michael S. Briggs, Robert C. Duncan, and Christopher Thompson. Statistical Properties of SGR 180620 Bursts. *The Astrophysical Journal Letters*, 532(2):L121, 2000.

[96] Markus J. Aschwanden, Norma B. Crosby, Michaila Dimitropoulou, Manolis K. Georgoulis, Stefan Hergarten, James McAteer, Alexander V. Milovanov, Shin Mineshige, Laura Morales, Naoto Nishizuka, and et. al. 25 Years of Self-Organized Criticality: Solar and Astrophysics. *Space Science Reviews*, 198(1-4):47–166, July 2014.

[97] M. B. Nielsen, L. Gizon, H. Schunker, and C. Karoff. Rotation periods of 12 000 main-sequence Kepler stars: Dependence on stellar spectral type and comparison with v sin i observations. *Astronomy & Astrophysics*, 557:L10, September 2013. arXiv: 1305.5721.

[98] A. McQuillan, T. Mazeh, and S. Aigrain. Rotation Periods of 34,030 Kepler Main-sequence Stars: The Full Autocorrelation Sample. *The Astrophysical Journal Supplement Series*, 211(2):24, 2014.

[99] T. R. Marsh and Keith Horne. Images of accretion discs II. Doppler tomography. *Monthly Notices of the Royal Astronomical Society*, 235(1):269–286, November 1988.

[100] A. Clauset, C. Shalizi, and M. Newman. Power-Law Distributions in Empirical Data. *SIAM Review*, 51(4):661–703, November 2009.

[101] Bradley E. Schaefer. KIC 8462852 Faded at an Average Rate of 0.164 0.013 Magnitudes per Century from 1890 to 1989. *The Astrophysical Journal Letters*, 822(2):L34, 2016.

[102] Benjamin T. Montet and Joshua D. Simon. KIC 8462852 Faded throughout the Kepler Mission. *The Astrophysical Journal Letters*, 830(2):L39, 2016.

[103] Michael Hippke, Daniel Angerhausen, Michael B. Lund, Joshua Pepper, and Keivan G. Stassun. A Statistical Analysis of the Accuracy of the Digitized Magnitudes of Photometric Plates on the Timescale of Decades with an Application to the Century-long Light Curve of KIC 8462852. *The Astrophysical Journal*, 825(1):73, 2016.

[104] M. A. Thompson, P. Scicluna, F. Kemper, J. E. Geach, M. M. Dunham, O. Morata, S. Ertel, P. T. P. Ho, J. Dempsey, I. Coulson, G. Petitpas, and L. E. Kristensen. Constraints on the circumstellar dust around KIC 8462852. *Monthly Notices of the Royal Astronomical Society: Letters*, 458(1):L39–L43, May 2016.

[105] Bradley E. Schaefer, Rory O. Bentley, Tabetha S. Boyajian, Phillip H. Coker, Shawn Dvorak, Franky Dubois, Emery Erdelyi, Tyler Ellis, Keith Graham, Barbara G. Harris, and et. al. The KIC 8462852 light curve from 2015.75 to 2018.18 shows a variable secular decline. *Monthly Notices of the Royal Astronomical Society*, 481(2):2235–2248, December 2018.

[106] M. C. Wyatt, R. van Lieshout, G. M. Kennedy, and T. S. Boyajian. Modelling the KIC8462852 light curves: compatibility of the dips and secular dimming with an exocomet interpretation. *Monthly Notices of the Royal Astronomical Society*, 473(4):5286–5307, February 2018.

[107] Tabetha S. Boyajian, Roi Alonso, Alex Ammerman, David Armstrong, A. Asensio Ramos, K. Barkaoui, Thomas G. Beatty, Z. Benkhaldoun, Paul Benni, Rory O. Bentley, Andrei Berdyugin, and et. al. The First Post- Kepler Brightness Dips of KIC 8462852. *The Astrophysical Journal Letters*, 853(1):L8, 2018.

[108] Peter Foukal. Reddened Dimming of Boyajians Star Supports Internal Storage of Its Missing Flux. *Research Notes of the AAS*, 1(1):52, 2017.

[109] P. Foukal, C. Fröhlich, H. Spruit, and T. M. L. Wigley. Variations in solar luminosity and their effect on the Earth's climate. *Nature*, 443(7108):161–166, September 2006.

[110] Bradley E. Schaefer, Jeremy R. King, and Constantine P. Deliyannis. Superflares on Ordinary Solar-Type Stars. *The Astrophysical Journal*, 529(2):1026, 2000.

[111] Han He, Huaning Wang, and Duo Yun. Activity Analyses for Solar-type Stars Observed with Kepler. I. Proxies of Magnetic Activity. *The Astrophysical Journal Supplement Series*, 221(1):18, 2015.

[112] Takuya Shibayama, Hiroyuki Maehara, Shota Notsu, Yuta Notsu, Takashi Nagao, Satoshi Honda, Takako T. Ishii, Daisaku Nogami, and Kazunari Shibata. Superflares on Solar-type Stars Observed with Kepler. I. Statistical Properties of Superflares. *The Astrophysical Journal Supplement Series*, 209(1):5, 2013.

[113] H. W. Babcock. The Topology of the Sun's Magnetic Field and the 22-YEAR Cycle. *The Astrophysical Journal*, 133:572, March 1961.

[114] Paul Charbonneau, Scott W. McIntosh, Han-Li Liu, and Thomas J. Bogdan. Avalanche models for solar flares (Invited Review). *Solar Physics*, 203(2):321–353, November 2001.

[115] E. N. Parker. Nanoflares and the solar X-ray corona. *The Astrophysical Journal*, 330:474–479, July 1988.

[116] G. A. Chapman, A. M. Cookson, and J. J. Dobias. Variations in total solar irradiance during solar cycle 22. *Journal of Geophysical Research: Space Physics*, 101(A6):13541–13548, June 1996.

[117] P. Foukal and J. Lean. Magnetic modulation of solar luminosity by photospheric activity. *The Astrophysical Journal*, 328:347–357, May 1988.

[118] Richard C. Willson. ACRIM3 and the Total Solar Irradiance database. *Astrophysics and Space Science*, 352(2):341–352, August 2014.

[119] Paul Charbonneau. Dynamo Models of the Solar Cycle. *Living Reviews in Solar Physics*, 7, 2010.

[120] Nir Friedman, Shinya Ito, Braden A. W. Brinkman, Masanori Shimono, R. E. Lee DeVille, Karin A. Dahmen, John M. Beggs, and Thomas C. Butler. Universal Critical Dynamics in High Resolution Neuronal Avalanche Data. *Physical Review Letters*, 108(20):208102, May 2012.

[121] I.-H. Cho, K.-S. Cho, S.-C. Bong, E.-K. Lim, R.-S. Kim, S. Choi, Y.-H. Kim, and V. Yurchyshyn. Statistical Comparison Between Pores and Sunspots by Using SDO/HMI. *The Astrophysical Journal*, 811(1):49, 2015.

[122] Matthias Rempel and Rolf Schlichenmaier. Sunspot Modeling: From Simplified Models to Radiative MHD Simulations. *Living Reviews in Solar Physics*, 8(1):3, December 2011.

[123] E. N. Parker. Sunspots and the physics of magnetic flux tubes. I - The general nature of the sunspot. II - Aerodynamic drag. *The Astrophysical Journal*, 230:905–923, June 1979.

[124] L. M. Zelenyi and A. V. Milovanov. Fractal Properties of Sunspots. *Soviet Astronomy Letters*, 17:425, November 1991.

[125] S. Criscuoli, M. P. Rast, I. Ermolli, and M. Centrone. On the reliability of the fractal dimension measure of solar magnetic features and on its variation with solar activity. *Astronomy & Astrophysics*, 461(1):331–338, January 2007.

[126] B. Rajkumar, S. Haque, and W. Hrudey. Fractal Dimensions of Umbral and Penumbral Regions of Sunspots. *Solar Physics*, 292(11):170, November 2017.

[127] Carolus J. Schrijver, Alan M. Title, Adriaan A. van Ballegooijen, Hermance J. Hagenaar, and Richard A. Shine. Sustaining the Quiet Photospheric Network: The Balance of Flux Emergence, Fragmentation, Merging, and Cancellation. *The Astrophysical Journal*, 487(1):424, 1997.

[128] Samuel D. T. Grant, David B. Jess, Teimuraz V. Zaqarashvili, Christian Beck, Hector Socas-Navarro, Markus J. Aschwanden, Peter H. Keys, Damian J. Christian, Scott J. Houston, and Rebecca L. Hewitt. Alfvn wave dissipation in the solar chromosphere. *Nature Physics*, 14(5):480, May 2018.

[129] Tritschler A., Rimmele T. R., Berukoff S., Casini R., Kuhn J. R., Lin H., Rast M. P., McMullin J. P., Schmidt W., Wger F., and DKIST Team null. Daniel K. Inouye Solar Telescope: Highresolution observing of the dynamic Sun. *Astronomische Nachrichten*, 337(10):1064–1069, November 2016.

[130] Collados M., Bettonvil F., Cavaller L., Ermolli I., Gelly B., Prez A., SocasNavarro H., Soltau D., Volkmer R., and the EST team null. European Solar Telescope: Progress status. *Astronomische Nachrichten*, 331(6):615–619, June 2010.

[131] Peter V. Foukal. The Photosphere. In *Solar Astrophysics*, pages 133–166. Wiley-VCH Verlag GmbH, 2004.

[132] Robert A. White and Karin A. Dahmen. Driving Rate Effects on Crackling Noise. *Physical Review Letters*, 91(8):085702, August 2003.

[133] A. Quesnel, B. R. Dennis, B. Fleck, C. Froelich, and H. S. Hudson. The Signature of Flares in VIRGO Total Solar Irradiance Measurements. volume 428 of *Astronomical Society of the Pacific Conference Series*, Northeast Harbor, Maine, March 2010.

[134] Jean-Paul Poirier. *Creep of Crystals: High-Temperature Deformation Processes in Metals, Ceramics and Minerals.* Cambridge University Press, February 1985.

[135] A. H. Cottrell and B. A. Bilby. Dislocation Theory of Yielding and Strain Ageing of Iron. *Proceedings of the Physical Society. Section A*, 62(1):49, 1949.

[136] D. Hull and D. J. Bacon. Chapter 7 - Jogs and the Intersection of Dislocations. In D. Hull and D. J. Bacon, editors, *Introduction to Dislocations (Fifth Edition)*, pages 137–155. Butterworth-Heinemann, Oxford, January 2011.

[137] William D. Callister and David G. Rethwisch. *Materials Science and Engineering: An Introduction.* John Wiley & Sons, December 2013.

[138] Conyers Herring. Diffusional Viscosity of a Polycrystalline Solid. *Journal of Applied Physics*, 21(5):437–445, May 1950.

[139] R. L. Coble. A Model for Boundary Diffusion Controlled Creep in Polycrystalline Materials. *Journal of Applied Physics*, 34(6):1679–1682, June 1963.

[140] F. R. N. Nabarro. Steady-state diffusional creep. *Philosophical Magazine*, 16(140):231–237, August 1967.

[141] F. R. N. Nabarro. Do we have an acceptable model of power-law creep? *Materials Science and Engineering: A*, 387-389:659–664, December 2004.

[142] Edward Neville Da Costa Andrade. On the viscous flow in metals, and allied phenomena. *Proc. R. Soc. Lond. A*, 84(567):1–12, June 1910.

[143] W. H. Wang, C. Dong, and C. H. Shek. Bulk metallic glasses. *Materials Science and Engineering: R: Reports*, 44(2):45–89, June 2004.

[144] J. S. Langer. Shear-transformation-zone theory of plastic deformation near the glass transition. *Physical Review E*, 77(2):021502, February 2008.

[145] S. G. Mayr. Activation Energy of Shear Transformation Zones: A Key for Understanding Rheology of Glasses and Liquids. *Physical Review Letters*, 97(19):195501, November 2006.

[146] H. J. Frost and M. F. Ashby. *Deformation-mechanism maps: the plasticity and creep of metals and ceramics*. Pergamon Press, 1982.

[147] Thiebaud Richeton, Jrme Weiss, and Franois Louchet. Dislocation avalanches: Role of temperature, grain size and strain hardening. *Acta Materialia*, 53(16):4463–4471, September 2005.

[148] W. H. Jiang, G. J. Fan, F. X. Liu, G. Y. Wang, H. Choo, and P. K. Liaw. Rate dependence of shear banding and serrated flows in a bulk metallic glass. *Journal of Materials Research*, 21(9):2164–2167, September 2006.

[149] R. Maa, D. Klaumnzer, and J. F. Lffler. Propagation dynamics of individual shear bands during inhomogeneous flow in a Zr-based bulk metallic glass. *Acta Materialia*, 59(8):3205–3213, May 2011.

[150] Robert Zwanzig. *Nonequilibrium Statistical Mechanics*. Oxford University Press, April 2001. Google-Books-ID: 4cI5136OdoMC.

[151] A. Alan Middleton. Asymptotic uniqueness of the sliding state for charge-density waves. *Physical Review Letters*, 68(5):670–673, February 1992.

[152] P. C. Martin, E. D. Siggia, and H. A. Rose. Statistical Dynamics of Classical Systems. *Physical Review A*, 8(1):423–437, July 1973.

[153] Hans-Karl Janssen. On a Lagrangean for classical field dynamics and renormalization group calculations of dynamical critical properties. *Zeitschrift fr Physik B Condensed Matter*, 23(4):377–380, December 1976.

[154] Michael P Leblanc. *Avalanches in plastic deformation: maximum velocity statistics, finite temperature effects, and analysis of low time resolution data*. PhD thesis, University of Illinois at Urbana-Champaign, 8 2016.

[155] A. Alan Middleton. Thermal rounding of the charge-density-wave depinning transition. *Physical Review B*, 45(16):9465–9468, April 1992.

[156] P. W. Anderson. Theory of Flux Creep in Hard Superconductors. *Physical Review Letters*, 9(7):309–311, October 1962.

[157] P. W. Anderson and Y. B. Kim. Hard Superconductivity: Theory of the Motion of Abrikosov Flux Lines. *Reviews of Modern Physics*, 36(1):39–43, January 1964.

[158] M. Mller, D. A. Gorokhov, and G. Blatter. Velocity-force characteristics of a driven interface in a disordered medium. *Physical Review B*, 63(18):184305, April 2001.

[159] C. De Dominicis. Techniques de Renormalisation de la Théorie des Champs et Dynamique des Phénomènes Critiques. *Le Journal de Physique Colloques*, 37(C1):C1–247–C1–253, January 1976.

[160] K. B. Efetov. Supersymmetry and theory of disordered metals. *Advances in Physics*, 32(1):53–127, January 1983.

[161] John A. Hertz, Yasser Roudi, and Peter Sollich. Path integral methods for the dynamics of stochastic and disordered systems. *Journal of Physics A: Mathematical and Theoretical*, 50(3):033001, 2017.

[162] Thomas Nattermann, Semjon Stepanow, Lei-Han Tang, and Heiko Leschhorn. Dynamics of interface depinning in a disordered medium. *Journal de Physique II*, 2(8):1483–1488, 1992.

[163] Deniz Erta and Mehran Kardar. Critical dynamics of contact line depinning. *Physical Review E*, 49(4):R2532–R2535, April 1994.

[164] Christof Wetterich. Exact evolution equation for the effective potential. *Physics Letters B*, 301(1):90–94, February 1993.

[165] Andrei A. Fedorenko and Semjon Stepanow. Depinning transition at the upper critical dimension. *Physical Review E*, 67(5):057104, May 2003.

[166] Leon Balents, Jean-Philippe Bouchaud, and Marc Mzard. The Large Scale Energy Landscape of Randomly Pinned Objects. *Journal de Physique I*, 6(8):1007–1020, August 1996.

[167] Daniel S. Fisher. Sliding charge-density waves as a dynamic critical phenomenon. *Physical Review B*, 31(3):1396–1427, February 1985.

[168] Alejandro B. Kolton, Alberto Rosso, and Thierry Giamarchi. Creep Motion of an Elastic String in a Random Potential. *Physical Review Letters*, 94(4):047002, February 2005.

[169] Vesselin Yamakov, Dieter Wolf, Simon R. Phillpot, Amiya K. Mukherjee, and Herbert Gleiter. Dislocation processes in the deformation of nanocrystalline aluminium by molecular-dynamics simulation. *Nature Materials*, 1(1):45–49, September 2002.

[170] Arthur F. Voter. Introduction to the Kinetic Monte Carlo Method. In *Radiation Effects in Solids*, pages 1–23. Springer, Dordrecht, 2007.

[171] Mukul Kabir, Timothy T. Lau, David Rodney, Sidney Yip, and Krystyn J. Van Vliet. Predicting Dislocation Climb and Creep from Explicit Atomistic Details. *Physical Review Letters*, 105(9):095501, August 2010.

[172] Pengyang Zhao, Ju Li, and Yunzhi Wang. Heterogeneously randomized STZ model of metallic glasses: Softening and extreme value statistics during deformation. *International Journal of Plasticity*, 40:1–22, January 2013.

[173] Naoki Yoshioka, Ferenc Kun, and Nobuyasu Ito. Kinetic Monte Carlo algorithm for thermally induced breakdown of fiber bundles. *Physical Review E*, 91(3):033305, March 2015.

[174] M. Rajaguru and S. M. Keralavarma. A Discrete Dislocation Model of Creep in Single Crystals. In *TMS 2016 145th Annual Meeting & Exhibition*, pages 351–358. Springer, Cham, 2016.

[175] A. B. Bortz, M. H. Kalos, and J. L. Lebowitz. A new algorithm for Monte Carlo simulation of Ising spin systems. *Journal of Computational Physics*, 17(1):10–18, January 1975.

[176] Santiago A. Serebrinsky. Physical time scale in kinetic Monte Carlo simulations of continuous-time Markov chains. *Physical Review E*, 83(3):037701, March 2011.

[177] Daniel T Gillespie. A general method for numerically simulating the stochastic time evolution of coupled chemical reactions. *Journal of Computational Physics*, 22(4):403–434, December 1976.

[178] James L. Blue, Isabel Beichl, and Francis Sullivan. Faster Monte Carlo simulations. *Physical Review E*, 51(2):R867–R868, February 1995.

[179] Alejandro B. Kolton, Alberto Rosso, Thierry Giamarchi, and Werner Krauth. Creep dynamics of elastic manifolds via exact transition pathways. *Physical Review B*, 79(18):184207, May 2009.

[180] V. H. Purrello, J. L. Iguain, A. B. Kolton, and E. A. Jagla. Creep and thermal rounding close to the elastic depinning threshold. *Physical Review E*, 96(2):022112, August 2017.

[181] Alberto Rosso and Werner Krauth. Monte Carlo dynamics of driven elastic strings in disordered media. *Physical Review B*, 65(1):012202, November 2001.

[182] Ezequiel E. Ferrero, Laura Foini, Thierry Giamarchi, Alejandro B. Kolton, and Alberto Rosso. Spatiotemporal Patterns in Ultraslow Domain Wall Creep Dynamics. *Physical Review Letters*, 118(14):147208, April 2017.

[183] D.F. Castellanos and M. Zaiser. Avalanche Behavior in Creep Failure of Disordered Materials. *Physical Review Letters*, 121(12):125501, September 2018.

[184] H. A. Kramers. Brownian motion in a field of force and the diffusion model of chemical reactions. *Physica*, 7(4):284–304, April 1940.

[185] Donald L. Kreher and Douglas R. Stinson. Combinatorial Algorithms: Generation, Enumeration, and Search. *SIGACT News*, 30(1):33–35, March 1999.

[186] J. Lu, G. Ravichandran, and W. L. Johnson. Deformation behavior of the Zr41.2ti13.8cu12.5ni10be22.5 bulk metallic glass over a wide range of strain-rates and temperatures. *Acta Materialia*, 51(12):3429–3443, July 2003.

[187] S. X. Song, Y. H. Lai, J. C. Huang, and T. G. Nieh. Homogeneous deformation of Au-based metallic glass micropillars in compression at elevated temperatures. *Applied Physics Letters*, 94(6):061911, February 2009.

[188] L. I. Salminen, A. I. Tolvanen, and M. J. Alava. Acoustic Emission from Paper Fracture. *Physical Review Letters*, 89(18):185503, October 2002.

[189] Ekhard K. H. Salje, Hanlong Liu, Linsen Jin, Deyi Jiang, Yang Xiao, and Xiang Jiang. Intermittent flow under constant forcing: Acoustic emission from creep avalanches. *Applied Physics Letters*, 112(5):054101, January 2018.

[190] Jan Beirlant, Yuri Goegebeur, Jozef Teugels, and Johan Segers. The Probabilistic Side of Extreme Value Theory. In *Statistics of Extremes*, pages 45–82. John Wiley & Sons, Ltd, 2004.

[191] M. A. Sheikh and K. A. Dahmen. Supplementary Material. *Supplementary Material*, 2018.

[192] Daniel Dufresne. The log-normal approximation in financial and other computations. *Advances in Applied Probability*, 36(3):747–773, September 2004.

[193] Jrme Weiss, Franz Lahaie, and Jean Robert Grasso. Statistical analysis of dislocation dynamics during viscoplastic deformation from acoustic emission. *Journal of Geophysical Research: Solid Earth*, 105(B1):433–442, January 2000.

[194] Rusty Allred. *Digital Filters for Everyone: Third Edition.* Creative Arts & Sciences House, 3 edition edition, March 2015.

[195] Nir Friedman. *Avalanches in Disordered Systems.* PhD thesis, University of Illinois at Urbana-Champaign, 8 2013.